5-2023

A Study on Asymmetric Perfect Vortex: Fractional Orbital Angular Momentum and Nonlinear Interaction

Kunjian Dai
kunjiad@clemson.edu

A STUDY ON ASYMMETRIC PERFECT VORTEX: FRACTIONAL ORBITAL ANGULAR MOMENTUM AND NONLINEAR INTERACTION

A Dissertation
Presented to
the Graduate School of
Clemson University

In Partial Fulfillment
of the Requirements for the Degree
Doctor of Philosophy
Electrical Engineering

---

by
Kunjian Dai
May 2023

Accepted by:
Dr. Eric G. Johnson, Committee Chair
Dr. Joe Watkins
Dr. Lin Zhu
Dr. Judson Ryckman

ABSTRACT

In this work, the manipulation including generation and detection of the asymmetric perfect vortex (APV) carrying fractional orbital angular momentum (OAM) was demonstrated and discussed. All the manipulation of the modes is in real-time which provides a perfect tool for sensing the dynamic properties of complex media. The OAM-involved nonlinear conversion, specifically the second-harmonic generation (SHG) using the APV and asymmetric Bessel-Gaussian (BG) beams was studied in detail.

The generation and detection of the APV are based on the HOBBIT concept which includes acoustic optical deflector (AOD) and log-polar coordinate transformation optics. The RF signal driving the AOD allows the real-time controlling of the OAM modes. Because of the asymmetric property of the modes, the APV beams can carry fractional OAM with a linear one-to-one correspondence of the fractional charges. The feature of the Doppler frequency shift caused by the AOD was introduced and demonstrated which was used to build a Poincaré sphere to encode and decode information. The spatial APV basis was also demonstrated by developing a pulsed 2D HOBBIT system which includes two AODs controlling both the OAM and radial dimensions. Examples using all these HOBBIT systems to sense complex media were given to show the real-time OAM spectrum measurement.

The SHG process of the APV and the asymmetric BG beams was discussed. The theoretical and experimental results show how beams with OAM-independent and OAM-dependent sizes behave in the nonlinear process. Both the two beam models gave a very good one-to-one correspondence of fractional charges which shows the potential to use the

beam models for information encoding and decoding. Different parameters impacting the OAM-related nonlinear conversion were discussed. These parameters include power density, phase-matching condition, and mode overlapping. Multiple OAM modes nonlinear interaction was also studied. The reverse HOBBIT system was used to verify the multi-mode interaction theory of the APV modes. Using the nonlinear interaction theory of the APV, the 2D HOBBIT was used as the source to excite the SHG process and generate deep UV APV carrying OAM. The effects of how OAM and radial beam size affect the nonlinear interaction were illustrated.

DEDICATION

To my family, friends, and colleagues for their help and encouragement.

ACKNOWLEDGMENTS

I would like to thank my advisor, Dr. Eric Johnson, for his support, help, and guidance throughout my fantastic PhD study. Without his advice and support, I would not have such a memorable journey. He also taught me how to think and do good research and showed me how to be a better researcher.

I would like to thank my committee members Dr. Joe Watkins, Dr. Lin Zhu, and Dr. Judson Ryckman, for their valuable time, help, and advice.

I would like to thank all the former and present members of the Micro-Photonics lab, for their selfless help and advice. I would also like to thank Dr. Keith Miller for his patient support and assistance.

I would like to thank my family for their understanding, support and always being there for me.

I would like to thank all the nice people in my life and my best friends who supported and helped me.

Lastly, I would like to thank my wife for her love and support.

Funding for this research was provided by: ONR N00014-16-1-3090, N00014-17-1-2779, N00014-20-1-2037, N00014-18-1-2225, N00014-18-1-2377, N00014-20-1-2558.

TABLE OF CONTENTS

Page

LIST OF FIGURES

List of Figures (Continued)

Figure Page

List of Figures (Continued)

List of Figures (Continued)

Figure Page

CHAPTER ONE

INTRODUCTION

1.1 Background

Structured light has drawn lots of attention in recent years due to its potential applications in fields like optical communications, particle manipulation, remote sensing, and quantum information technology. Among all kinds of structured light such as manipulations on intensity, phase, and polarization, beams carrying orbital angular momentum (OAM) are specific because of their interesting properties [1]. Carrying a spiral phase pattern $\exp(i\ell\theta)$, where ℓ represents the so-called OAM charge and θ denotes the azimuthal coordinate, OAM beams have a Poynting vector that spirals along the propagation direction and a donut-shape intensity distribution [2]. The entire set of integer OAM can be considered as an infinite Hilbert space which indicates the ability of OAM beams to encode and decode information.

Laguerre Gaussian (LG) beams, Bessel beams, and perfect vortex beams are regular OAM beam models. The intensity and phase profiles of the three types of beams are shown in Fig. 1.1.1. LG beams not only have the azimuthal dimension (OAM) but also carry a radial degree of freedom, which shows potential in applications such as optical communications [3] and remote sensing [4]. Bessel beams have very special properties like non-diffracting and self-healing, which are potential tools for particle manipulation and sensing. The beam sizes of both LG and Bessel beams are OAM related which means under the same conditions beams carrying larger OAM will have a larger beam size. In some

cases, it is important to explore the effects only caused by OAM. Then perfect vortices are an ideal choice since beams carrying any OAM have the same intensity distribution. The beam models introduced here are considered to carry an integer OAM charge, and in the next section, OAM beams carrying fractional charges will be discussed.

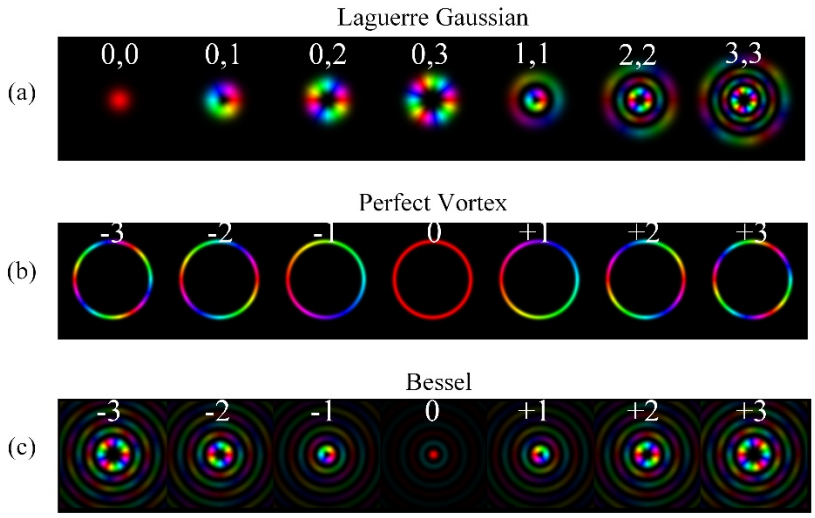

Fig. 1.1.1. Regular OAM-carrying beam models.

1.2 Fractional OAM

The set of all integer OAM constructs an infinite Hilbert space which is the key point to exploiting OAM as carriers for information encoding and decoding. Then a very interesting question here is does fractional OAM exist? If so, the channel capacity and light spectrum efficiency can be largely enhanced which will be beneficial to OAM-related applications.

One key feature of OAM beams is the spiral phase and the spiral phase pattern can be used to generate and detect OAM. For an integer OAM charge ℓ, the transverse spiral phase pattern changes from 0 to 2π by ℓ times. If a spiral phase pattern that does not

change phase by integer times is used to generate OAM, there will be a phase discontinuity in this phase pattern and the generated field will have constructed and destructed interference along propagation. This generated beam can be seen as a fraction OAM beam since the global/mean OAM is not an integer. In 2004, M V Berry derived what would happen when a plane wave illuminates fractional phase step and he found that no fractional-strength can propagate which is due to the phase discontinuity in the beam [5]. Berry also found that the global OAM of the generated beam is always the nearest integer to the fractional value. So the OAM mapping curve for plane wave illuminating a fractional phase pattern is like stairs. In 2007, J. B. Götte et al. decomposed a fractional OAM state by using an integer OAM states basis and when the fractional OAM phase pattern is illuminated by a Gaussian beam, the results show a winding mapping curve whose global OAM is equal to the fractional phase pattern order only at integer and half-integer OAM charges [6]. The global/mean OAM value can be calculated as $\overline{M} = M - \frac{\sin(2M\pi)}{2\pi}$, where M denotes the order of the fractional phase pattern. This equation can be found in many papers involving fractional OAM analysis, however, it fits the situation best when the incident beam has a Gaussian description.

The generated fractional OAM by the above methods usually has a very complicated intensity and phase distribution due to the evolvement of phase discontinuity along propagation. The complexity of the OAM mapping curve is also a problem since it is better to have a linear OAM mapping curve considering the difficulty to discern two adjacent OAM charges which is essential in information decoding. However, like many

different beam models that can be used as OAM carrying beams, illuminating the fractional spiral phase pattern with a plane wave or Gaussian beam is not the only way to generate fractional OAM states. To address the issues of fractional OAM, researchers have developed other methods to demonstrate fractional OAM.

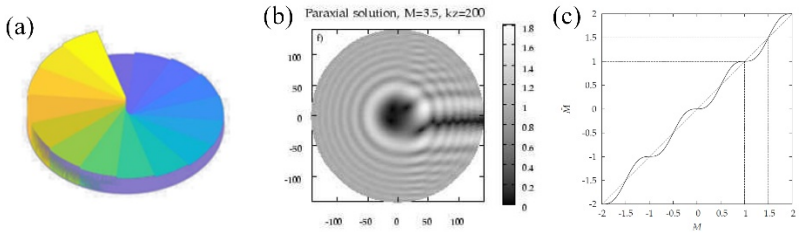

Fig. 1.2.1. (a) The illustration of a fractional SPP. (b) The intensity distribution of a fractional OAM beam with charge 3.5 [6]. (c) The plot of the global OAM for fractional OAM beams [6].

According to M. J. Padgett [7], OAM may have a different global/mean value depending on the choice of the calculation axis. This calculation will decide whether the OAM carried by a beam is intrinsic or extrinsic. Discussing the basic intrinsic nature of OAM is not the purpose of this dissertation since the information encoding/decoding system will have a fixed axis most time. But the lateral shift of the axis provides a way to tailor OAM. In 2019, Kotlyar et al. used a Gaussian beam to illuminate an off-axis spiral phase plate (SPP) and measured the dependence of global OAM on the SPP's shift [8]. In Ref. [6] mentioned above, the fractional OAM states are decomposed into an integer OAM basis. Actually, this can be done in a reverse way to generate fractional OAM. In 2014, Kotlyar et al. proposed a beam model called asymmetric Bessel-Gauss beams which can carry both integer and fractional OAM [9], and this beam model is based on a Bessel-Gauss

basis. By controlling the summation coefficients of the basis, the global OAM can be manipulated. In 2008, J. B. Götte et al. put forward to a fractional OAM beam generated by a synthesis of LG basis [10] and this method overcomes the structure non-stable problem of fractional OAM.

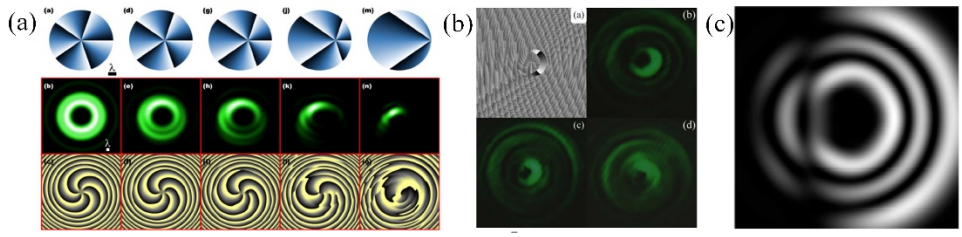

Fig. 1.2.2. Three methods to generate fractional OAM beams. (a) Off-axis SPP [8]. (b) The asymmetric Bessel-Gauss beams [9]. (c) Superposition method using LG basis [10].

All the fractional OAM generation methods introduced above can be realized by creating relative phase patterns. These phase patterns can be generated on a glass substrate using photolithography or simply by displaying a phase device like a spatial light modulator (SLM) or a deformable mirror device (DMD). However, the mode switch rate based on glass-substate optics, SLM or DMD is very low and limited by tens of Hz to a few kHz. The mode switching rate is rather an essential concern when OAM is used to sense some disturbance of flowing media. In 2019, Wenzhe Li et al. demonstrated a rapidly tunable OAM generation system for higher-order Bessel beams integrated in time (HOBBIT) [11]. The HOBBIT system shows an OAM mode switching rate of 400 kHz and works for both integer and fractional OAM which are continuously tunable. The fractional OAM generated by HOBBIT shows a linear mapping curve and is used to probe atmosphere turbulence in real-time [12].

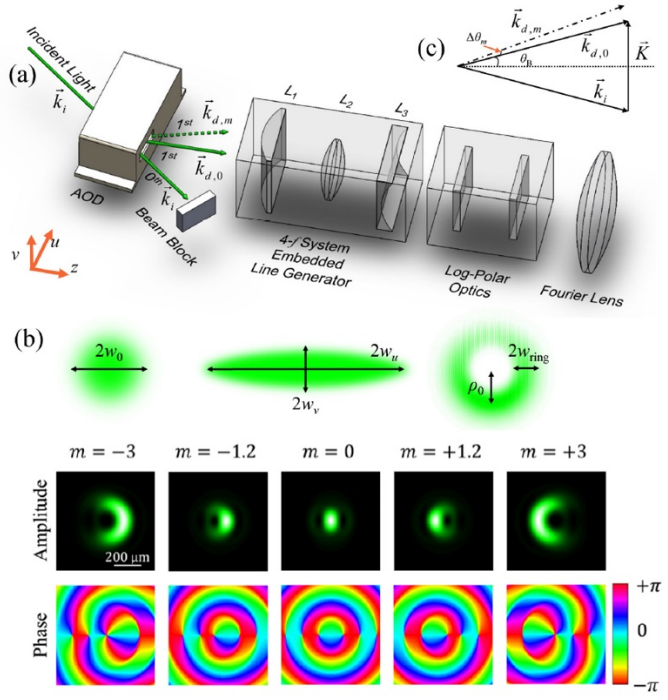

Fig. 1.2.3. The HOBBIT system [11].

The fractional OAM offers an extension to the degree of freedom of the spatial modes. But the complication of the mode structure also brings some limitations to applications of these modes. In the next section, OAM-related nonlinear processes will be introduced. The nonlinear interaction shows a new vision to generate and manipulate OAM.

1.3 OAM-related nonlinear conversion

Nonlinear optics not only is a good way to generate new frequencies, but also provides a method to manipulate OAM. Energy and momentum conservations are basic rules in nature. Since the OAM charge is used to represent momentum, how OAM charge performs in nonlinear processes is what we concern.

It has been shown that the second-harmonic generation (SHG) of LG mode is used to generate higher OAM charges [13, 14]. Using a so-called naïve theory of SHG in [14],

the complex amplitude of the generated field, $E(2\omega)$, is proportional to the square of the fundamental beam's complex amplitude, $E(2\omega) \propto \left(E(\omega)\right)^2$. Then if $E(\omega) = \exp(i\ell\theta)$, the generated SHG field will carry a phase term of $\exp(i2\ell\theta)$, which tells that not only the light frequency but also the OAM charge are doubled in the SHG process. Other OAM-related nonlinear processes involving a single OAM pump also follow the momentum conservation law and it is easy to get the OAM charge changing rule.

The situation is a little complicated when multiple OAM work as input to a nonlinear process since the multiple OAM interaction needs to be considered. Let us still take SHG for example, if two OAM having the same light frequency are input and the field can be described as $E(\omega) = \exp(i\ell_1\theta) + \exp(i\ell_2\theta)$, mathematically the SHG field can be expressed as $E(2\omega) \propto \left(E(\omega)\right)^2 = \exp(i2\ell_1\theta) + \exp(i2\ell_2\theta) + 2\exp\left(i(\ell_1+\ell_2)\theta\right)$. But some references do not show this result. In 2014, Zhou et al. [15] show that if $LG_0^2 + LG_0^{-2}$ works as the pump in the SHG, the generated field has a complex amplitude as $LG_0^4 + LG_0^{-4} - LG_2^0$, where LG_p^ℓ denotes an LG mode and p is the radial index and ℓ is OAM. The mode cross-interaction part does not have a coefficient of 2. This is because for OAM modes whose beam size is OAM-dependent, the propagation will be different and only the overlapping section in the nonlinear medium will generate frequency doubling. A similar phenomenon is shown in [16], a four-wave mixing process with different OAM as pumps, the amplitude coefficients of the generated fields depend on the mode overlapping and all the coefficients can be evaluated by an integral describing the overlapping.

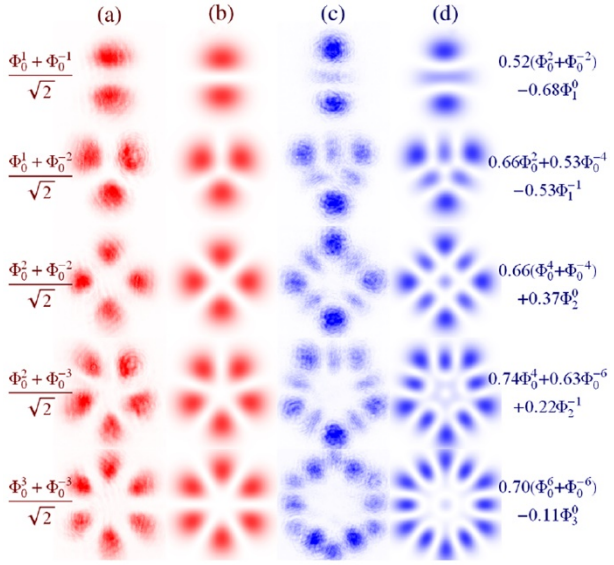

Fig. 1.3.1. Four-wave mixing of multiple OAM beams and mode overlapping [16].

As demonstrated in section 1.2, the fractional OAM can be decomposed into an integer OAM basis. As a result, the nonlinear interaction of fractional OAM can be treated as multiple OAM interaction to some extent. However, the decomposition of fractional OAM usually has a large bandwidth and for each component, the complex amplitude coefficients may vary. This variation will increase the calculation complexity of the mode overlapping integral. Another key factor that matters a lot is the phase-matching condition. Since phase-matching is the basic nature of nonlinear interaction, it will determine the nonlinear conversion efficiency directly. As mentioned in [2], the Poynting vector of OAM beams spirals along the propagation direction, and the skew angle between the Poynting vector and the propagation direction is $\frac{\ell}{kr}$, where k is the wave number and r is beam radius in the radial direction. According to this expression, the skew angle is both OAM and beam size related. When multiple OAM interaction needs to be considered in nonlinear

processes, different OAM may have a different phase-matching condition which will affect the final complex amplitude coefficients. Then simply considering the mode overlapping integral may be not accurate enough but still is a good approximation. In Ref. [17, 18], the SHG of fractional OAM generated by fractional phase step SPP and shifted SPP are discussed and the OAM decomposition method is the method in [6].

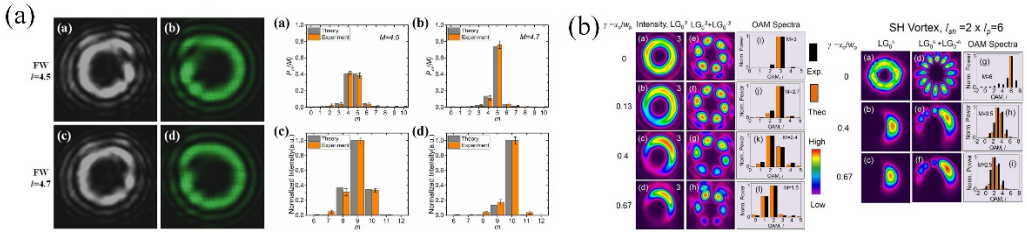

Fig. 1.3.2. (a) SHG of fractional OAM beams generated by fractional SPP [17]. (b) SHG of fractional OAM beams generated by off-axis SPP [18].

The nonlinear optics technique offers a chance to manipulate both light frequency and OAM at the same time which could be beneficial to applications involving light wavelengths that are not easy to directly generate from a resonator. For example, blue/green wavelengths are more used in underwater maritime environments, and to get a light wavelength of 532 nm the most convenient way is to do frequency doubling based on a 1064 nm laser which can be easily generated.

1.4 Peer work and state of art

Because of the high-dimensionality of OAM-carrying beams, since the spiral Poynting vector was first discussed in [2], OAM has drawn a lot of attention and in the past 20 years a lot of achievement have been done. In 2012, OAM-carrying beams have been used in a free-space optical communication channel and a 2.56 Tbit s^{-1} rate and 95.7 bit s^{-}

[1] Hz^{-1} spectral efficiency have been realized [3]. The OAM-matter interaction has stimulated the OAM optical tweezer and it can be used to trap or rotate small particles [7]. Due to the natural property of high-dimensionality, OAM is also a perfect choice for quantum information technique. In [19], Dada et al. utilized an ultraviolet (UV) Gaussian pump and a type-I BBO crystal to generate a spontaneous parametric down-conversion (SPDC), and the generated two-photon state can be described as $|\Psi\rangle = \sum_{\ell=-\infty}^{\ell=\infty} c_\ell |\ell\rangle_A \otimes |-\ell\rangle_B$, where A and B are the signal and idler photons respectively, c_ℓ is the complex coefficient for each component in the superposition and $|c_\ell|^2$ denotes the probability for each component. The signs for the two photons' OAM indicate the momentum conservation in this SPDC process. Spatial modes or structured light with high dimensionality are a perfect tool for applications requiring more degrees of freedom. The first key issue will be how to generate and detect OAM beams.

Usually, the OAM generation methods can also be used for detection. As mentioned above, photolithography and displaying devices are common methods to generate OAM beams because it is easy to simulate phase variance across the transverse plane. For the photolithography method, a common way is to etch the phase pattern on a glass substrate to generate SPP and due to the thickness difference in the cross section, the light path will be different in the transverse 2D plane. The SPP is widely used in OAM-related research, for example in [20] it is used for an underwater communication link to generate OAM. An SLM or DMD mirror is very convenient to simulate the phase pattern, and in [3] SLM is used to generate high-order OAM beams. Different phase patterns can be involved together

to realize multiple functions such as in [21] a 2D forked grating is used to generate a 3 by 3 OAM array and two different types of gradually-changing-period gratings are used to detect the OAM order by observing the petal numbers in the far-field plane. Compared to the gradually-changing-period gratings, a similar far-field intensity pattern can be gotten by simply using a cylindrical lens [22]. Using a cylindrical lens, there is also quantitative measurement by using a single or two lenses [23, 24] and the far-field intensity distributions are used to calculate the OAM mean value utilizing the Electro-Magnetic theory. In 2002, Jonathan Leach et al. put forward a cascaded Mach-Zehnder interferometer scheme to sort OAM and by setting more stages the input OAM can be sorted perfectly [25]. In 2019, a multiple plane LG mode sorter was demonstrated by Nicolas K. Fontaine, and by reflecting the laser beam multiple times between an SLM and a mirror, the input beam can be decomposed into a Cartesian grid of spots which tell the OAM charge [26]. In 2020, a reconfigurable OAM sorter using Gouy phase accumulation based on cascaded optical resonators was demonstrated in [27] and this method works dynamically and can be used for different wavelengths. Similarly based on Gouy phase accumulation, a Gouy phase radial mode sorter was demonstrated in [28], and by using the Gouy phase differences of LG beams the radial and azimuthal modes can be sorted by cascaded schemes. When an OAM beam illuminates a spinning object, the reflected beam will show a Doppler frequency shift which can be described as $\Delta f = \ell\Omega / 2\pi$, where Ω is the rotating rate of the spinning object [29]. This rotational Doppler effect was used to detect OAM in [30] by measuring the beating frequencies. In [11], Li et al. developed a HOBBIT system that can generate tunable OAM rapidly using AOD and log-polar coordinate transformation

optics. Doing coordinate transformation is another way to manipulate OAM. The log-polar optics was first used for sorting OAM in [31] by mapping the azimuthal phase gradient of OAM to the linear phase in cartesian coordinate, and the linear phase is Fourier transformed by a lens to a shifted line shape in the far-field whose shifted position is dependent on OAM charge. The log-polar optics is a perfect tool to detect integer OAM, however, the resolution might be a problem since the line shape is not extremely thin which causes overlapping between modes. The potential method to enhance the resolution is embedding fan-out grating into the phase pattern and the linear phase is duplicated to multiple pieces whose Fourier transform corresponds to a much narrow line shape [32, 33]. For rapid manipulation of structured light, the HOBBIT method is not the only one. In [34], Braverman et al. developed a method to generate Hermite-Gauss mode by using an acousto-optic modulator (AOM) which basically is an AOD and the switching speed also reaches sub-MHz level.

Structured light including OAM beams is widely used for sensing tasks since any phase disturbance caused by complex media could produce an OAM spectrum broadening. By measuring the OAM spectrum change or broadening, information like amplitude, or phase can be extracted. As mentioned above, OAM beams can be used to detect the rotating speed of a spinning object [29]. Some related research using different types of detection schemes, direction-sensitivity, and spatially incoherent light can be found in [35-37]. Another remote sensing task is to probe the dynamic properties of flowing media. As demonstrated in [38], LG beams are used to estimate the flow vorticity of a fluid. And in [12], the HOBBIT beams are used to probe the continuous spectrum of atmospheric

turbulence. OAM beams can also be used to do traditional and quantum imaging. By using SLM to generate LG beams basis, a sequence of LG modes is used to sense an amplitude object in [4]. Spatial modes are widely used in quantum information technology since their natural high dimensionality and OAM beams can be used to do quantum imaging [39]. When OAM beams are utilized to do remote sensing, one key requirement of the OAM-carrying beams is the dynamic mode control which can be considered as a high mode switching speed. However, conventional OAM generation and detection methods usually do not have a high enough mode switching speed to do real-time sensing. The SLM-based method is no more than 60 Hz, and the DMD method is usually several kHz. One potential way might be the HOBBIT concept. By using AOD which can do fast modulation to incident laser beams, the mode switching speed can be up to MHz level [11].

Nonlinear conversion is a useful tool to study the basic phenomena of OAM beams since the energy and momentum conservation rule. As shown in [13, 14], in an SHG process the integer OAM is exactly doubled by the input charge. This result can be simply thought as the OAM conservation law. The similar relation between the input and output charges have been observed in many other nonlinear processes, such as sum-frequency generation (SFG) [40], difference-frequency generation (DFG) [41], high-harmonic generation (HHG) [42, 43], SPDC [44], four-wave mixing [45-47] and vortex-pumped optical parametric oscillator [48]. The OAM charges discussed here are all integers, however, for fractional OAM beams the nonlinear conversion will be more complicated and the OAM charges may not follow the phenomena above. In [23], a quantitative method was demonstrated by using the far-field intensity of fractional OAM which is diffracted by

a cylindrical lens and the OAM mapping curve follows a winding trace. Even the OAM mapping curve without any nonlinear process does not give a linear one-to-one relationship, the nonlinear conversion of fractional OAM seems not to be predictable. The study of SHG using fractional OAM which is generated by a fractional SPP was demonstrated in [17]. In 2017, Stanislovaitis et al. studied the nonlinear conversion of integer and half-integer OAM and found that the OAM conservation law stands for these OAM charges [49]. In 2018, Alam et al. studied SHG of fractional OAM by shifting integer SPP [18]. Most nonlinear studies involving fractional OAM do not give the OAM mapping curve directly since the complicated process. Instead, the OAM spectrum is used to study the nonlinear conversion, as shown in [17, 18]. Finding a way to quantize the nonlinear converted fractional OAM is potential since it is essential to decern different OAM in applications employing complex modulation and demodulation technique.

To address the problems of applications using fractional OAM, the study of OAM generation and detection needs to be done. For real-time sensing applications, it is essential to find a method to increase the mode switching speed which should be much faster than SLM and DMD methods. The second requirement for fractional OAM is the OAM mapping curve for fundamental and nonlinear-generated OAM should have a linear one-to-one feature. The related discussion will be made in the following chapters.

1.5 Dissertation outline

In this dissertation, chapter 1 discussed the relative concept, the background of our work as well as the state of art, and motivation.

Chapter 2 will introduce the real-time generation and detection of both integer and fractional OAM based on the HOBBIT and reverse HOBBIT systems. The OAM modes generated by a HOBBIT are known as asymmetric perfect vortex (APV). The AOD in both systems will increase the mode switching rate up to MHz level. The log-polar coordinate transformation optics provide a convenient way to make a transfer between the linear phase and azimuthal OAM phase. The acoustic wave generated Doppler frequency shift offers the ability to map the generated OAM modes to a Poincaré sphere and this property will be used to study the fraction OAM nonlinear conversion. Several real-time sensing tasks will also be illustrated.

Chapter 3 will demonstrate the scheme of the 2D HOBBIT system which can generate APV not only having the OAM dimension but also having the radial dimension control. Another AOD is used to control the beam position in the log-polar mapping which corresponds to different beam sizes. The generated APV with radial control is analogous to LG modes which have both OAM and radial charges. The 2D HOBBIT system is also used for remote sensing tasks. Phase measurement, amplitude pattern recognition, and measurement of rotating fog density are illustrated as examples. The theory and experiment of using the 2D HOBBIT and the reverse HOBBIT to measure partial coherence is also demonstrated.

Chapter 4 will discuss the nonlinear conversion of asymmetric Bessel-Gaussian (BG) beams carrying integer and fractional OAM. The asymmetric BG beams are one beam model generated by the HOBBIT system. The OAM mapping curves of both fundamental and SHG OAM are measured based on the cylindrical lens method. The

experimental results show a good one-to-one correspondence of OAM charges mapping. The SHG-related parameters impacting the OAM nonlinear conversion will be discussed. The SHG conversion of multiple OAM as input will be studied and the conversion efficiency of the SHG will be given.

Chapter 5 will demonstrate the nonlinear conversion of APV which is the other beam model of the HOBBIT system. The analysis of OAM calculation based on Electro-Magnetic theory will be given which shows the reason why APV beams carry fractional OAM having a linear one-to-one mapping curve in both fundamental and SHG fields. The reverse HOBBIT will be used to study this nonlinear process. The multiple OAM interaction in SHG will be studied and measured by the reverse HOBBIT system. The spatial APV generated by the 2D HOBBIT will be used to study the phenomena of multiple OAM and radial modes involved process and the deep ultra-violate (UV) OAM generation by the 2D HOBBIT nonlinear conversion is also illustrated.

Chapter 6 will summarize the studies throughout the dissertation and outline the future work.

CHAPTER TWO

THE HOBBIT AND THE REVERSE HOBBIT SYSTEMS

2.1 Introduction

Previously the basic concepts of OAM beams which are a special kind of structured light carrying a spiral phase wavefront have been introduced. The purpose is to develop the generation and detection method which can do OAM encoding and decoding in real-time. For current OAM generation and detection schemes, the mode switching rate is limited to under a few kHz which may not satisfy the demand of sensing media dynamically. To sense even a tiny change in disturbance, a continuous manipulation of the OAM spectrum which means the arbitrary control of integer and fractional OAM are necessary.

Since OAM can be considered as a phase structure, most generation and detection methods are based on optical phase elements. Static methods like SPP [50], diffractive gratings [21, 51], and cylindrical lenses [22-24] are very easy to implement. Dynamic methods are mainly dependent on SLM or DMD which is mainly limited by the refresh rates of the devices. The refresh rates of SLM tend to be lower than 60 Hz and the DMD can reach a refresh rate of kHz but is limited in resolution based on the space bandwidth product. There are also some bulky schemes that can be used to sort OAM states. These methods include cascaded Mach-Zehnder interferometers [25], LG mode sorter based on multi-plane method [26], a mode sorter using rotating rob to add different Doppler frequency shifts to modes [30], methods using Gouy phase accumulation to sort OAM and

LG radial modes [27, 28]. There are also mode sorting methods based on coordinate transformation by using the concept of log-polar mapping. The first log-polar detection scheme is illustrated in [31] which does the polar-cartesian transformation. The OAM azimuthal phase gradient is mapped to a linear phase which is Fourier transformed by a lens. The far-field of a beam with a linear phase corresponds to a linear shift, so by measuring the shifted distance one could extract the OAM information from this method. However, the issue of log-polar optics is the detection resolution which is decided by the relation between the limited beam size and the linear phase gradient. Methods have been developed to solve this problem. In [32, 33], a fan-out grating method is embedded into the log-polar transformation and a few copies of the linear phase have been made to increase the beam size dimension and narrow the bandwidth of the far-field. These methods work perfectly for integer OAM charges but not for fractional OAM. Deformation of the log-polar transformation is the so-called spiral transformation and in [52] this method is demonstrated and can achieve superior resolution with integer OAM. By introducing multiple circular-sector transformations into the coordinate mapping optics, OAM multiplication and division can be accomplished and this method provides a way to generate higher-order OAM beams [53]. In most cases, the far-fields which tell the OAM information from the coordinate transformation optics are still captured by a detector array which might be a charge-coupled device (CCD). The CCD camera determines the low refresh rate of the detection scheme. In a recent paper, a set of static phase masks and an AOM are used to generate OAM states at a mode switch rate up to 500 kHz [34]. Many of these static and dynamic methods have proven to be effective for OAM generation or

detection under some specific conditions. However, the combination of the log-polar coordinate transformation and the AOD is demonstrated in [11] and the linear phase is generated by the AOD and mapped to the azimuthal phase gradient by the log-polar optics. This HOBBIT concept gives an insight into how to generate OAM states in real-time. And in [12], the HOBBIT system is used to sense the tiny disturbance of the atmospheric turbulence with a continuous OAM spectrum including both integer and fractional OAM.

In this chapter, the concept of the HOBBIT system including the introduction of AOD and log-polar coordinate transformation will be introduced. Then the detailed theory of the reverse HOBBIT system will be demonstrated. By combining the log-polar mapping and the AOD technologies and exploiting different ways to create driving radio frequency (RF) signals, the AOD works as a time-varying linear phase generator on the transmitter side (HOBBIT) and phase correlator on the receiver side (reverse HOBBIT). Due to the fast refreshing of the RF signals on both the transmission and detection sides, the HOBBIT and the reverse HOBBIT system yield a real-time varying OAM generation and mode sorting. Another interesting feature of the AOD-based HOBBIT system, the Doppler frequency shift, will be discussed. The Doppler frequency shift caused by the momentum conservation of the AOD will provide the ability to create the Poincaré sphere by adding an initial phase difference to different OAM modes and the RF signal also offers the convenience to control the power ratio of each mode. The reverse HOBBIT system will provide coherent detection to verify the generation of single or multiple OAM-varying beams with both integer and fractional charges at MHz level. All these features will be supported by experimental results and relative analyses. Lastly, several remote sensing

examples will show the ability of the HOBBIT and the reverse HOBBIT to do real-time scanning of complex media.

2.2 The HOBBIT system

As mentioned above, two essential elements of the HOBBIT concept are the log-polar optics and the AOD. The coordinate transformation was first used in imaging processing for rotation invariant pattern recognition [54]. There are two phase elements included in this transformation, one to do an optical geometric transformation which maps the linear phase gradient and OAM azimuthal phase gradient to each other, and the second one to correct the phase error from the wrapping process [31]. The acousto-optic devices are widely used to do laser beam modulation and beam shaping [55-57]. The AOD and the log-polar optics construct the main part of the HOBBIT system. This time-varying OAM generation system is shown in Fig. 2.2.1. In this system, a linear-polarized incident Gaussian beam works as input and travels through an AOD which will be named the transmitter AOD compared to the receiver AOD in the reverse HOBBIT system which will be demonstrated later in this chapter. The transmitter AOD (Gooch & Housego AODF 4120-3) is driven by a time-varying RF signal $S(t)$. Any change in $S(t)$ corresponds to a frequency change and will result in a deflection angle difference which means embedding a linear phase to the incident Gaussian beam. A typical deflection efficiency of 70-80% can be achieved by using the AOD. The Gaussian beam carrying a linear phase will be mapped to the log-polar optics by a well-designed lens system ($F_1 = 50mm, F_2 = 100mm, F_3 = -50mm$ as shown in the figure). This lens system will reshape the Gaussian spot to an elliptical Gaussian beam with specific widths in both

horizontal and vertical directions. The following optics after the AOD are aligned with the light path which corresponds to the Bragg angle deflection of the AOD. As a result, the angle difference caused by different linear phases will deflect the beam away from this light path. However, the lens system will still image the beam back to the axis which will be the position of the first log-polar optics. The advantage of mapping the elliptical Gaussian beam to a ring shape is the interference effect from any phase discontinuity when the two ends of the beam recombine can be eliminated so that one can generate both integer and fractional OAM. Another benefit of using the AOD is to use all kinds of filters based on digital signal processing (DSP) techniques to modulate the RF signal which will then be used to manipulate the laser beam and control the intensity distribution around the whole ring shape. After the log-polar mapping, the elliptical Gaussian line beam will be wrapped to an asymmetric ring which is called the near-field of the HOBBIT with the name of APV. The APV shown in the figure carries an OAM charge of +1 whose colormap indicates the phase gradient changing from 0 to 2π. Then this complex amplitude of APV is Fourier transformed by a Fourier lens and in the Fourier plane the far-field distribution which is called the asymmetric BG beam can be observed and the nonlinear interaction of the asymmetric BG beams will be discussed in chapter 3.

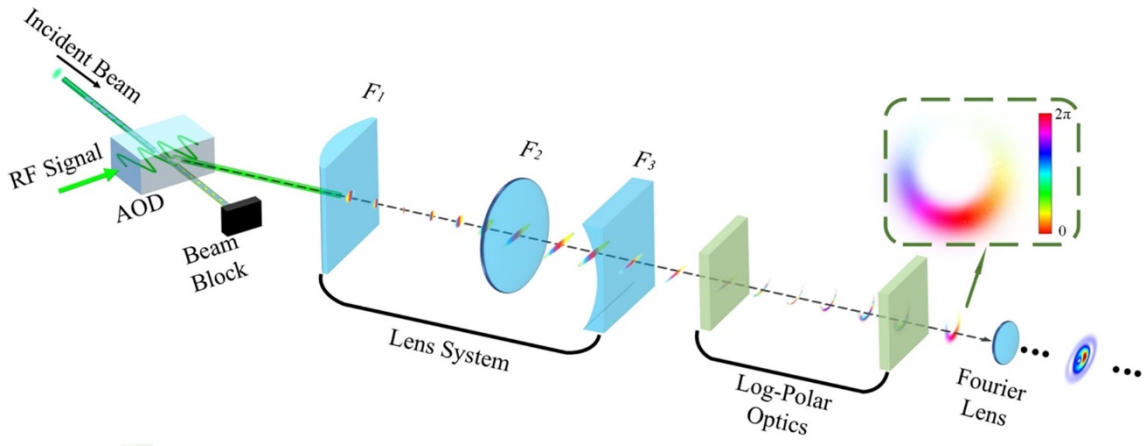

Fig. 2.2.1. The HOBBIT system [58].

The RF signal $S(t)$ can be described in a general form as follows:

$$S(t)=\sum_{n} c_n \sin\left(2\pi f_n(t)t+\varphi_n\right), \tag{2.1}$$

where c_n is the weighting factor of each sinusoidal component which will determine the power ratio of each mode, $f_n(t)$ is the time-varying frequency function describing the frequency change of each sine wave, and φ_n is the initial phase of each sinusoidal component. When the incident Gaussian beam propagates through the AOD, the RF signal will generate an acoustic wave traveling through the AOD which will deflect the Gaussian beam with the Bragg condition. The general Bragg angle can be expressed as follows:

$$\theta_B=\frac{\lambda_0 f_{AOD}}{2V_{at}}, \tag{2.2}$$

where $\lambda_0=\dfrac{c}{f_c+f_{AOD}}$ is the light wavelength after the AOD which is affected by the Doppler effect, c is the speed of light, f_c is the incident light frequency, $f_{AOD}=125MHz$ is the central working frequency for Bragg condition, and V_{at} is the acoustic velocity of

the transmitter AOD. As mentioned earlier, the light path is aligned based on the Bragg condition of the AOD, then when the transmitter AOD works at its central frequency, the generated beam from the HOBBIT will carry an OAM charge of 0. When driven by a different frequency, the AOD will deflect the beam and the generated beam will carry an +/- OAM depending on the blue or red shift of the RF frequency. The deflection angle change of the beam can be described as

$$\Delta\theta_{\ell n} = \frac{\lambda_{\ell n}}{V_{at}\eta_t}\left(f_{AOD} - f_n(t)\right), \tag{2.3}$$

where $\lambda_{\ell n} = \dfrac{c}{f_c + f_n(t)}$ is the Doppler shifted wavelength for an OAM charge ℓ after passing through the transmitter AOD, and $\eta_t = \dfrac{F_2}{F_1}$ is the amplification factor of the lens system where F_1 and F_2 are the focal lengths of the lenses shown in the figure. Now based on paraxial approximation, the OAM $\ell_n(t)$ can be expressed by the angle change $\Delta\theta_{\ell n}$,

$$\Delta\theta_{\ell n} = \frac{\lambda_{\ell n}\ell_n(t)}{2\pi a}, \tag{2.4}$$

where $a = \dfrac{3.6\,mm}{2\pi}$ is the parameter of the log-polar optics. From Eq. (2.3) and Eq. (2.4), the relation between the generated OAM and the RF driving frequency can be described as

$$\ell_n(t) = \frac{2\pi a}{V_{at}\eta_t}\left(f_{AOD} - f_n(t)\right). \tag{2.5}$$

The generated OAM charge above $\ell_n(t)$ is the result of the frequency in a single sine wave component and it is time-varying. When the transmitter AOD is driven by a

combination of sine waves, the generated OAM is also a superposition of time-varying OAM charges. From Fig. 2.2.1., the near-field has not only the typical feature of PV whose beam size is OAM-independent, but also the asymmetry property. Considering the asymmetry and the combination of the RF signal, the complex amplitude of the near-field can be expressed as follows:

$$\begin{aligned}\overrightarrow{U}(r,\theta,z,t) &= \vec{x}S(t)\exp(i2\pi f_c t)\,A(r,\theta)\exp(-i\ell\theta - ikz) \\ &= \vec{x}\sum_n c_n \exp\left[i\left(2\pi f_n(t)t + \varphi_n\right)\right]\exp(i2\pi f_c t) \\ &\cdot \exp\left(-\frac{(r-r_0)^2}{w_r^2} - \frac{\theta^2}{w_\theta^2}\right)\exp\left(-i\ell_n(t)\theta - ik_{zn}z\right),\end{aligned} \tag{2.6}$$

where $\vec{x}$ stands for horizontal polarization and here $S(t) = \sum_n c_n \exp\left[i\left(2\pi f_n(t)t + \varphi_n\right)\right]$ is in its exponential formation representing the coherent superposition of the desired OAM beams. This representation is more suitable for the definition of complex amplitude and will directly reflect the Doppler effect caused by the transmitter AOD. $A(r,\theta)$ is the amplitude term for the APV which corresponds to $\exp\left(-\frac{(r-r_0)^2}{w_r^2} - \frac{\theta^2}{w_\theta^2}\right)$, with r_0 as the ring radius and w_r is the radial $1/e^2$ Gaussian width, and describes the asymmetry of the APV, β is the so-called asymmetry factor. β has a value which is the ratio of the elliptical Gaussian line length to $2\pi a$. The longitudinal wave vector is described as $k_{zn} = 2\pi\cos\left(\lambda_{\ell n}\ell_n(t)/2\pi a\right)/\lambda_{\ell n}$. Since the generated OAM states are determined by the RF driving signal, the summation sign indicates all the potential output results carrying arbitrary superposition with power and phase differences of OAM beams. As mentioned

earlier, the Fourier transform of a PV is the Bessel beam. The far-field, as known as the asymmetric BG beam, can be expressed as the following equation which corresponds to Eq. (2.6)

$$\vec{U}_{far} = \vec{x}\sum_{n} c_n \exp\left[i\left(2\pi f_n(t)t + \varphi_n\right)\right]\exp\left(i2\pi f_c t\right)\exp\left(-\frac{r^2}{w_G^2}\right)\sum_{m=-\infty}^{\infty} B_m J_m\left(\frac{k_{tm}r}{\mu_m}\right)\exp\left(-im\theta\right), \tag{2.7}$$

where the m summation of integer OAM corresponds to the far-field of the single time-varying OAM component $\ell_n(t)$. This phenomenon can be explained by the uncertainty between the angular position and the angular momentum [59]. $w_G = \lambda_{\ell n}(t)F/(\pi w_r)$ is the Gaussian envelope width. F is the focal length of the Fourier lens. $B_m = (-i)^m \exp\left[-w_\theta^2\left(\ell_n(t)-m\right)^2/4\right]$ is the discrete weighting factor for each $\ell_n(t)$ giving the OAM spiral spectrum. $J_m\left(\frac{k_{tm}r}{\mu_m}\right)$ is the first-order Bessel function with k_{tm} as the transverse wave vector and μ_m as the scaling factor [60].

2.3 The reverse HOBBIT system

Since the HOBBIT system can arbitrarily manipulate OAM generation in real-time, it is important for us to detect the OAM faster than the changing rate of the transmitter. The solution is the reverse HOBBIT system. By simply using the AOD and log-polar optics in a reverse order, the reverse HOBBIT system is developed for real-time OAM demultiplexing. To clarify, the sequence of the two log-polar optics is also in a reverse way. In this case, the input to the reverse HOBBIT will be the OAM states. The OAM

azimuthal phase will be unwrapped to a linear phase gradient by the log-polar optics. And this linear phase gradient will be Fourier transformed to the far-field corresponding to different transverse positions which indicate the input OAM information. In the reverse HOBBIT system, a second AOD, the receiver AOD, works as a linear phase correlator to cancel the linear phase gradient and make it back to a plane wavefront. To do real-time detection, the receiver AOD is driven by a carefully designed RF signal which is slightly different from the one used for the transmitter AOD. The reverse HOBBIT system is shown in Fig. 2.3.1. Because of the limited aperture size of the receiver AOD (BRIMROSE TEF-90-60-532) and the relatively large elliptical Gaussian line after the coordinate mapping, a reducing telescope ($F_1' = 50mm, F_2' = 500mm$) is used to narrow the beam size down to a reasonable value. After the receiver AOD, a Fourier lens is used to couple the filtered beam into a multi-mode fiber which is connected to an Avalanche Photodetector (APD) and works as an aperture. The detection results will be directly shown on the scope and the waveforms will be used to extract OAM information.

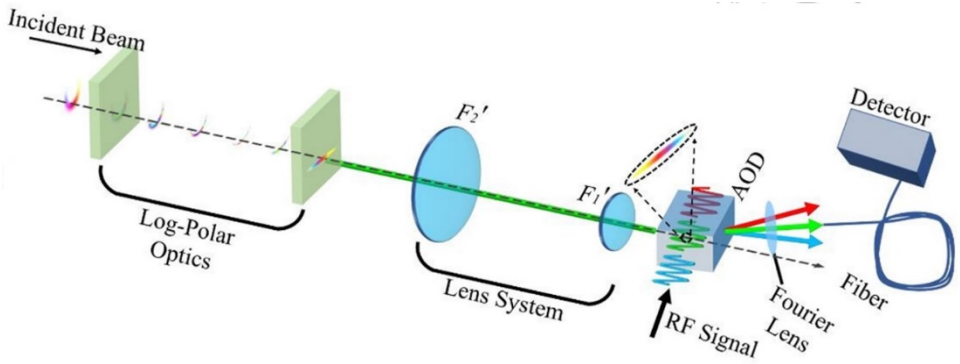

Fig. 2.3.1. The reverse HOBBIT system [58].

The assumption is taken that the reverse HOBBIT system sees time-varying OAM states which can be described by only a complex phase pattern

$\sum_n \exp\left(-i\ell_n(t)\theta\right)\exp\left[i2\pi\left(f_c + f_n(t)\right)t + i\varphi_n\right]$. The reverse log-polar optics will transfer this phase distribution to a superposition of linear phases. This superposition can be described as follows:

$$t_1 = \sum_n \exp\left(-i\frac{\ell_n(t)x}{a}\right)\exp\left[i2\pi\left(f_c + f_n(t)\right)t + i\varphi_n\right], \tag{2.8}$$

where x represents the horizontal coordinate at the receiver side. The same log-polar optics are used in the reverse HOBBIT system resulting in the same parameters for the optics. Considering the reducing telescope with two lenses whose focal lengths are F_1' and F_2', the linear phase of the original elliptical Gaussian beam is imaged to a smaller size but with a larger gradient. This change will be considered in the following design. Same as the transmitter side, $\eta_r = \frac{F_2'}{F_1'}$ works as the reducing factor of the lens system. The new linear phase can be expressed as

$$t_2 = \sum_n \exp\left(i\frac{\eta_r\ell_n(t)x}{a}\right)\exp\left[i2\pi\left(f_c + f_n(t)\right)t + i\varphi_n\right]. \tag{2.9}$$

Then the new linear phase function t_2 is sent to the receiver AOD which works as a matched filter and cross-correlates the linear phase generated by the RF signal loaded on the receiver AOD. The RF signal $R(t)$ loaded on the receiver AOD has a similar form as $S(t)$ for transmitter AOD and can be described as Eq. (2.10). The difference between $S(t)$ and $R(t)$ is that $R(t)$ is not a superposition of sine waves but only a linear chirp signal

$$R(t) = d_n \sin\left(2\pi g(t)t\right), \tag{2.10}$$

where d_n is the weighting factor used to balance the power ratio across the whole scanning OAM spectrum, $g(t)$ is the frequency time-varying function which usually is a linear frequency function. But $g(t)$ can be designed for specific mapping purposes and is not limited only to a linear chirp. This RF signal $R(t)$ generates a relative acoustic wave traveling across the receiver AOD can be considered as a phase grating and has a transmittance function expressed as follows:

$$t_G = \exp\left(i2\pi \frac{g_{AOD} - g(t)}{V_{ar}} x \right) \exp\left(i2\pi g(t) t \right), \tag{2.11}$$

where V_{ar} is the acoustic velocity of the receiver AOD and $g_{AOD} = 90MHz$ is the central working frequency of the receiver AOD. The cross-correlation happens in the receiver AOD between the incident linear phase gradient and the phase grating caused by the acoustic wave. The Fourier lens and the multi-mode fiber will be expressed as a spatial integration of the product of the linear phase and the RF time signal. Then the power captured by the APD can be derived as follows:

$$\begin{aligned} P(t) &= \left| \int_{-\infty}^{\infty} t_2 t_G^{*}(x,t) rect(\frac{\eta_r x}{2\pi a}) dx \right|^2 \\ &= \left| \sum_n \int_{-\infty}^{\infty} \exp\left[i\left(\frac{\eta_r \ell_n(t)}{a} - 2\pi \frac{g_{AOD} - g(t)}{V_{ar}} \right) x \right] \right. \\ &\quad \left. \times rect(\frac{\eta_r x}{2\pi a}) \exp\left[i2\pi \left(f_c + f_n(t) + g(t) \right) t + i\phi_n \right] dx \right|^2 . \end{aligned} \tag{2.12}$$

The power collected by the APD will reach its maximum if $\frac{\eta_r \ell_n(t)}{a} - 2\pi \frac{g_{AOD} - g(t)}{V_{ar}} = 0$, which leads to the correlation spot for detecting the OAM information in the incident beams:

$$\ell_n(t) = \frac{2\pi a}{V_{ar}\eta_r}\left[g_{AOD} - g(t)\right]. \tag{2.13}$$

The Eq. (2.13) has a very similar form compared to Eq. (2.5) on the transmitter side. This result tells that the OAM generation and detection are mapped to a frequency matching problem. By designing all the parameters based on the devices used in the systems, the OAM encoding and decoding using the HOBBIT and reverse HOBBIT can be controlled with a high degree of freedom. When the correlation happens on the receiver side, the deflected beam will be coupled into the multi-mode fiber. Since the use of RF signal on the receiver AOD, the real-time correlation will directly be displayed on the scope as a waveform. The voltage level reflects the weighting of the OAM spectrum. The real-time detection procedure is illustrated in Fig. 2.3.2., where the blue curve indicates the time-varying OAM information in the incident beam, and the red line represents the linear scanning across an OAM bandwidth of the receiver AOD RF signal. The time scale is exaggerated in the figure just for clarification purposes and in fact, the time scale is in μs level which results in a detection rate of up to MHz level. Considering the time scale of the scanning is so small that the correlation results will show a continuous recovery of the OAM information. If the incident beam carries more than one single OAM information, different OAM components will be deflected at different time points in one scanning but at different RF frequencies. This frequency difference will add different Doppler effects to

different OAM components. In this case, the interference of different OAM components will show oscillations on the waveform captured by the scope. Single OAM is not impacted by the Doppler effect since $R(t)$ including one sinusoidal waveform which will add an identical frequency shift to the input beam at one time point. However, the interference caused by the Doppler effect will not affect the OAM measurement considering the OAM information can still be extracted from the envelope of the waveform. This interference pattern will be shown in the experimental section. Our reverse HOBBIT not only works for the HOBBIT generated beams but also is available to any OAM-carrying beams. For example, if the LG beams are the input, the mapping procedure is mostly the same except there is no Doppler frequency difference in the input beam for each OAM component. Because the sweeping of $R(t)$ is much faster than the changing rate of OAM in the incident beam, the cross-correlation procedure can be done in real-time.

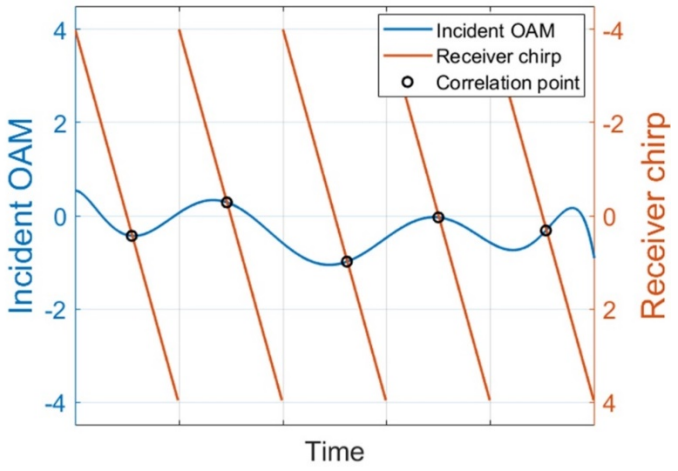

Fig. 2.3.2. Illustration of the correlation of the incident OAM and the RF chirp signal on the receiver side. The actual receiver chirp signal changes faster than the time varying OAM and the correlation points (black points) reflect the OAM change in real-time [58].

2.4 Experimental results for OAM measurement

In this section, the experimental results of the creation and detection of beams carrying time-varying OAM, detection of coherent OAM modes generated by HOBBIT, and creation of the Poincaré sphere by using the Doppler effect will be demonstrated.

To verify the real-time sensing as shown in Fig. 2.3.2. using the reverse HOBBIT, the single OAM measurement results are shown first. The HOBBIT is used to generate static single OAM first with 5 different integer OAM values of -2, -1, 0, +1, and +2. The waveforms collected by the scope are shown in Fig. 2.4.1(a). The difference between different peaks is due to the diffraction efficiency of the system. The ratio for each peak can be balanced very easily by controlling d_n. Figure 2.4.1(b) gives the OAM spectrogram which shows the continuous measurement of OAM in a time period of 100 μs. The input OAM is a static charge of 0. Each column in (b) is one frame of the waveform as shown in (a). In this result, $R(t)$ is a linear chirp lasting 1 μs which can scan or correlate OAM with a range from -4 to +4. Since $R(t)$ lasts 1 μs, the scanning rate by using this RF signal can reach an MHz level. From Fig. 2.4.1(a), we can see the resolution for adjacent integer OAM is poor which is determined by the basic nature of the design of the log-polar optics. When multiple OAM components are included in the incident beam, such as multiple LG modes, the scope will collect a continuous waveform which will indicate a result of a continuous OAM spectrum. This continuous OAM spectrum is still useful to estimate the global OAM change in the beam.

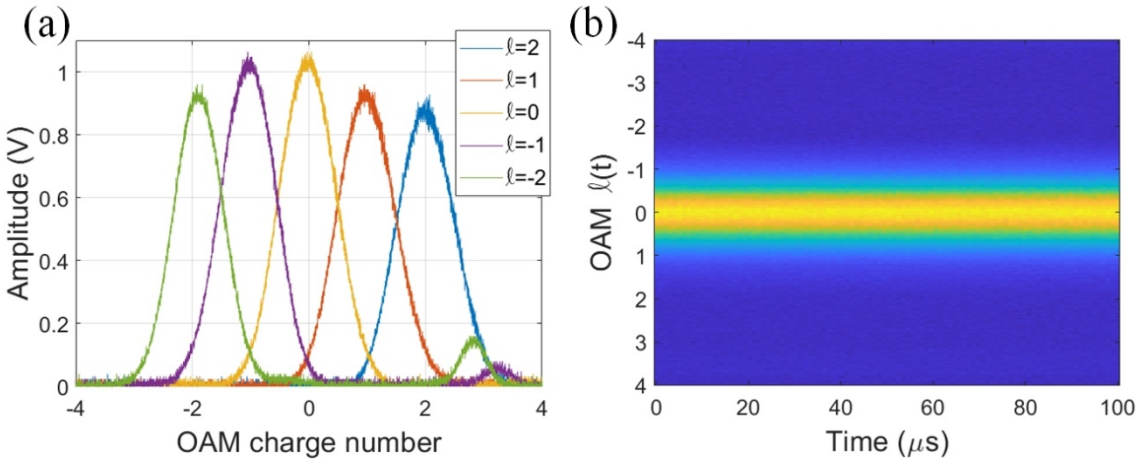

Fig. 2.4.1. Single static OAM measurement results. (a) Waveform collected by the scope which shows the results for measuring 5 integer OAM from -2 to +2. (b) The spectrogram for measuring OAM continuously during a time period of 100 μs . Each column in (b) is a Gaussian-like waveform as shown in (a) with a linear chirp of 1 μs [58].

To show the ability of the reverse HOBBIT to measure transient OAM, several RF signals are designed to generate time-varying OAM beams. Based on Eq. (2.5), the OAM $\ell_n(t)$ is related to the frequency function $f_n(t)$. Four different frequency functions are chosen: linear, quadratic, concave quadratic, and sinusoid, and use these four functions to create relative RF signals to drive the transmitter AOD. The measurement results are shown in Fig. 2.4.2. In all the results, a 1 μs linear chirp scanning through -4 to +4 is still used to drive the receiver AOD. In each result, the function of $\ell_n(t)$ is given to show the changing tendency of the transient OAM. From the results, we can see the HOBBIT system can be used to encode arbitrary OAM information to the laser beam and the generated modes can be used as probes for sensing. The corresponding detection using the reverse HOBBIT is

ideally matched to each architecture. Further manipulation of $R(t)$ will provide the ability to control the degree of freedom on the time scale.

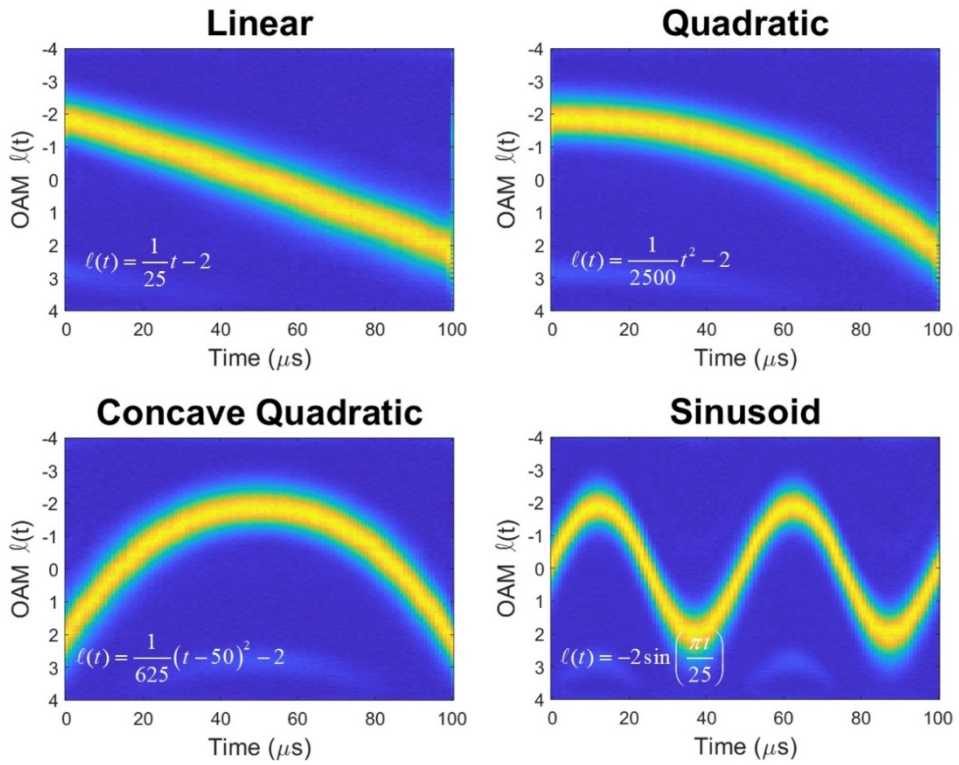

Fig. 2.4.2. Temporal OAM generation and verification using the HOBBIT and the reverse HOBBIT systems. Four different RF signals are designed to generate the transient OAM beams. The relative OAM function $\ell_n(t)$ is labeled in each figure above [58].

If the RF signal contains multiple sine waves which can generate multiple OAM components, for example $n = 2$ in Eq. (2.6), the coherent combinations of OAM beams can be generated. However, the utilizing of AOD will add a Doppler frequency shift to the incident beam which brings the benefit of controlling both amplitude and phase in the generated modes. This amplitude and phase encoding can be used to map the spatial information on a Poincaré sphere. In this case, the reverse HOBBIT system will extract

both amplitude and phase as a function of time from the OAM spectrogram results. Coherent combinations have been used for many applications and the mapping of the Poincaré sphere provides convenient modulation which is widely used in applications such as optical communications [61, 62]. A point U_a on the Poincaré sphere can be expressed as follows:

$$U_a = \cos\left(\frac{\theta_a}{2}\right)U_\ell + \sin\left(\frac{\theta_a}{2}\right)U_{-\ell}\exp\left(i\varphi_a\right), \tag{2.14}$$

where θ_a is the angle between the vector and the z axis, U_ℓ and $U_{-\ell}$ construct the two-dimensional Hilbert space, and φ_a denotes the phase difference between the two orthogonal vectors which is the angle between the projection of the vector and the x axis.

The measurement results for coherent states are shown in Fig. 2.4.3. There are clear oscillations in the waveform which is due to the Doppler effect. Three waveforms with different colors are shown and overlapped in Fig. 2.4.3(a) and the 3 phase differences are $0, \pi/4, \pi/2$. A 100 μs linear chirp signal works as $R(t)$ on the reverse HOBBIT system. More details will be introduced later. In Fig. 2.4.3(b), the details for the oscillated waveforms are shown and the delay caused by the phase differences can be clearly observed which could be used to extract the information from DSP analysis.

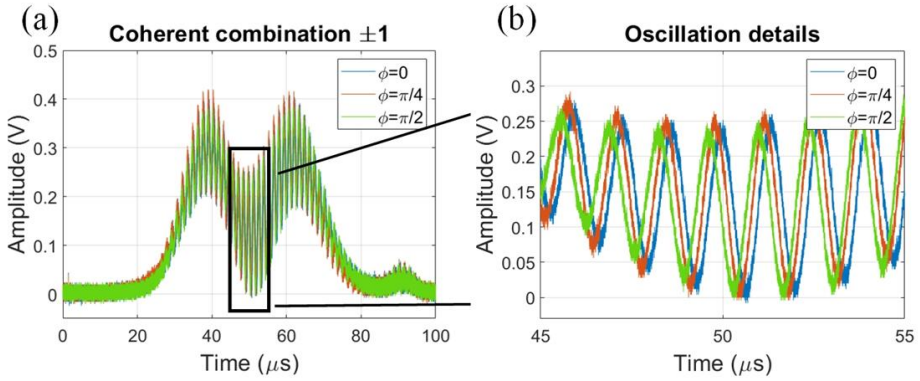

Fig. 2.4.3. The waveforms captured on the scope for measuring coherent states. (a) The oscillation shape for coherent states $\ell = \pm 1$ for 3 phase differences. (b) The detailed delays for the phase differences.

When one wants to measure the point coordinate on the Poincaré sphere, several measurements which are similar to the Stokes measurements for polarization states should be made. If a coherent combination of OAM states is used to represent this Poincaré sphere, the output beam will show an interference pattern which is typical for coherent OAM states. Here $\ell = \pm 1$ work as the two orthogonal states and to generate OAM $\ell = \pm 1$ using the HOBBIT system, the RF signal driving the transmitter AOD can be described as follows:

$$S(t) = \frac{1}{2}\left[c_1 \sin(2\pi f_1 t) + c_{-1} \sin(2\pi f_{-1} t + \varphi_a)\right], \tag{2.15}$$

where c_1 and c_2 denote the weighting factor for the two orthogonal states, specifically $c_1 = \cos\left(\frac{\theta_a}{2}\right)$, $c_2 = \sin\left(\frac{\theta_a}{2}\right)$.

For generating OAM $\ell = \pm 1$ with the HOBBIT system, according to the concept, the two frequencies are calculated as $f_1 = 124.6389 MHz$ and $f_{-1} = 125.3611 MHz$. The relative phase difference between the two states can be set in a range from 0 to 2π. To

illustrate this concept, the parameters are chosen as $c_1 = c_2 = 1$, $\varphi_a = 0, \pi/2, \pi, 3\pi/2$, and two poles which are OAM +1 and -1. All these six points on the Poincaré sphere correspond to 6 different RF signals on the transmitter side (the HOBBIT). The time intervals for all the points are not restricted any way, but are chosen to show the fidelity of this scheme for illustrative purposes. According to the log-polar parameters, lens system, and the acoustic velocity in Eq. (2.5), the frequency step for one OAM charge in the HOBBIT system is 0.3611 MHz. If $\ell = \pm 1$ are used as the two poles, the beating frequency in Fig. 2.4.3. will be 722 kHz. To resolve and measure this beating frequency, there is a requirement for the time interval used in the reverse HOBBIT. If the time intervals are too short, there will not be enough oscillations in the waveform and the information cannot be extracted. In this case, the $R(t)$ is a linear 100 μs chirp and there will be enough resolution for the beat frequency measurement in the following processing. The demonstration of the Poincaré sphere and the measurement results are shown in Fig. 2.4.4. The selected 6 points including the two poles and four points with phase differences on the equator are labeled on the sphere. The measured OAM spectrogram is shown in Fig. 2.4.4(b) and 6 time windows correspond to the 6 points. In this case, the two poles are shown in time window 1, 2 and there are only two bright peaks in each window indicating the positions of the poles. Time windows 3-6 represents the four points on the equator and on the right side of the figure a typical oscillation waveform is used to illustrate the interference of the two states. However, from the OAM spectrogram it is hard to extract the phase information since all the oscillations seem pretty similar to each other. To address this problem, the DSP analysis is exploited. Considering each column in the OAM spectrum is a waveform collected on the

scope and by knowing the sampling rate and time period a fast Fourier transform (FFT) analysis is performed to each column and extract the frequency spectrum from the results. The FFT analyzed results are shown in Fig. 2.4.4 (c-d). The frequency spectrogram is shown in Fig. 2.4.4(c) and the red line indicates the beating frequency position centered at 722 kHz. The time windows 3-6 show the predicted beat frequency and there is no frequency information in time windows 1-2 since only one OAM mode is measured. Next from the frequency information, the phase information can be extracted and the results are shown in Fig. 2.4.4(d). Again in windows 1-2 there are only meaningless phase noises and in windows 3-6 the phase gradient structure is shown. The same red line is centered at 722 kHz and phase values can be extracted from this position. The measured phase information indicates the phase changes of $0, \pi/2, \pi, 3\pi/2$ with an accuracy of $0.01\,\pi$. Although only 6 points are selected to illustrate the concept of constructing the Poincaré sphere, based on the accuracy of the phase measurement, more points can be chosen on the sphere to encode more information. Moreover, this method can be extended to recover the more complex amplitude and phase combinations of more than two OAM modes generated by the HOBBIT using only a single-pixel detector.

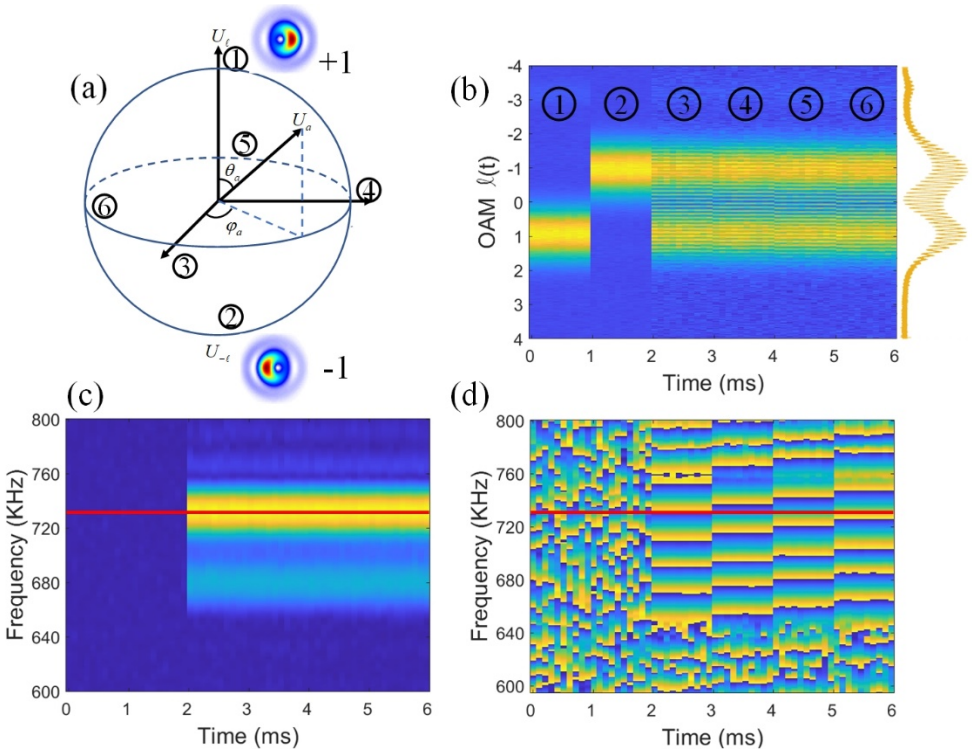

Fig. 2.4.4. The creation and detection of the Poincaré sphere using the HOBBIT and reverse HOBBIT systems. (a) The Poincaré sphere using two OAM orthogonal states. Six points are selected and labeled. (b)-(d) The measured OAM, frequency, and phase spectrograms [58].

2.5 Probing the variable density fog clouds

Compared to current spatial modes generation and detector methods, the HOBBIT and the reverse HOBBIT systems provide a perfect tool for rapid sensing applications. The MHz mode switching rate satisfies most sensing tasks. For free space optical communications links, the atmosphere turbulence caused wavefront distortion has a great impact on the channel capacity and the data rate. To understand the environment better, it is essential to sense and evaluate the environment much faster than any disturbance. Like

in Ref. [12], the HOBBIT system was used to map the small disturbance caused by the atmosphere using a continuous OAM spectrum with both integer and fractional charges. There are some rotating features in nature or human activities, like tornadoes or the wingtip vortices generated by an aircraft, which might be hazards to human life or properties. People are trying to search methods to measure, predict and avoid these hazards by developing lots of laser-based techniques, such as lidar [63].

In the lab, the water steams are blown into a plastic tube to make rotating fog density as shown in Fig. 2.5.1.. The tube has a length of 1.4 m and a transverse diameter of 100 mm. The APV generated by the HOBBIT system is imaged by a 10X telescope and has a beam size of 25 mm in the tube. The green line starts at the HOBBIT and ends at the reverse HOBBIT denoting the light path. From the inset, the fog is injected into the tube tangentially at three different positions along the tube with equal spacing. The red curve in the inset shows the coarse trace of the fog rotation. However, the real distribution of the fog rotation is quite complicated and the impact of the fog can be analyzed from the OAM spectrum change. The 1 μs linear chirp scanning OAM from -4 to +4 continuously is used in this case, which is much faster than the dynamics of the fog. Consecutive scans will be compiled to get the OAM spectrogram which is then used to trace the OAM change. When the APV propagates through the tube with dynamic fog, the measured spectrogram indicates the OAM components which are produced by the fog rotation. By simply flipping the tube, the fog rotation can be changed in both right-handed and left-handed rotation directions. The fog sensing results are shown in Fig. 2.5.2. The measurement result without any fog will be similar to Fig. 2.4.1(b). The spectrograms using OAM 0 and -1 to sense

right-handed rotating fog are shown in Fig. 2.5.2(b). The total sensing time is 30 s and from the spectrograms, we can observe that the OAM spectrum is deflected to the positive direction. This is because when the fog is blowing into the tube, the fog density changes with time and will cause a refractive index difference across the transverse plane in real time which introduces an OAM component to the incident APV. The difference between the spectrograms using different OAM is due to the fog generation process is not exactly the same every time. From the spectrograms, the OAM spectrum has a tendency going back to charge 0 which is because when the tube begins filling with more fog, although the fog is still rotating, the fog density will become more uniform which causes less refractive index difference across the transverse plane.

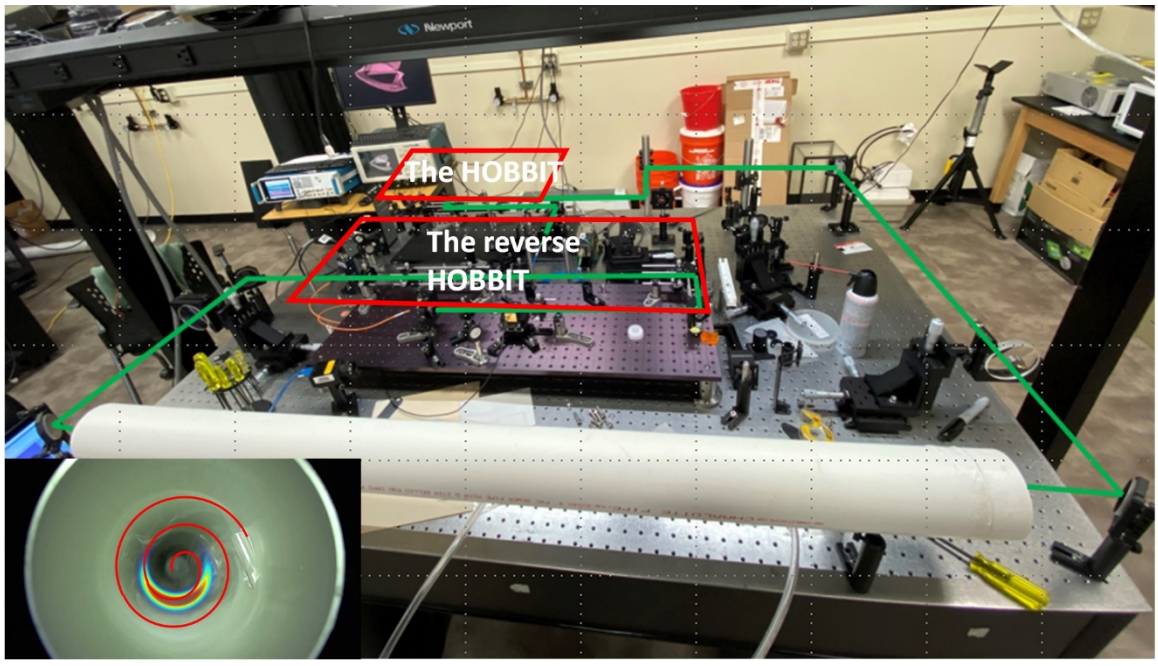

Fig. 2.5.1. The experimental setup for sensing the rotating fog density. The inset shows the transverse plane about how the fog moves in the tube and the input APV probe.

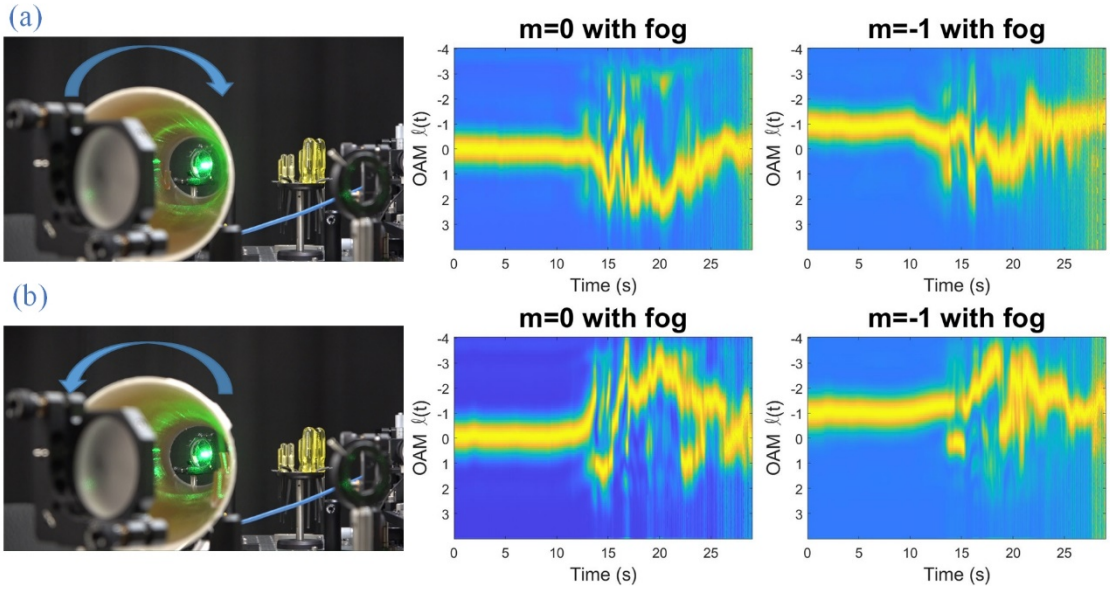

Fig. 2.5.2. Fog sensing results of both right-handed and left-handed rotation using OAM 0 and -1.

From the above results, we can see the measured OAM spectrogram is not a simple solid trace and there are lots of scattered-like information across each column which is because the fog distribution is very complicated. Besides, the measured OAM spectrum information is an accumulation result of the whole ring. It is important to measure the localized information in the azimuthal direction which can help us to understand the environment better. The OAM information is related to spatial scale and the beam size used in the sensing procedure also matters. To address these problems the 2D HOBBIT system was developed and will be demonstrated in chapter 3.

2.6 Summary

In this chapter, the concepts of the HOBBIT and the reverse HOBBIT systems to generate and detect OAM spectrograms which can map the space-time information of

OAM are demonstrated in detail. Both the HOBBIT and the reverse HOBBIT use log-polar optics and AOD. The log-polar optics are well-known for geometrical optical transformation and the AOD is for RF signal processing. The log-polar optics are used to transfer azimuthal phase gradient and linear phase to each other. The AODs are perfect tools to generate and correlate linear phase which are much faster than conventional phase modulators such as SLM and DMD. In this work, the AOD works as a linear phase generator in the HOBBIT system and a matched filter on the reverse HOBBIT side. Because of the use of AOD, the mode switch rate can reach MHz level with arbitrarily time-varying single or multiple OAM multiplexing and demultiplexing. The detailed theories for the HOBBIT and the reverse HOBBIT were derived and experimentally shown. Experimental results for measuring single static and dynamic OAM show the ability of generating and detecting spatial mode in real-time. Another important feature of the HOBBIT and the reverse HOBBIT is the ability to encode OAM with the so-called Doppler effect caused by the AOD. The beating frequency between different OAM can be used to create an information encoding and decoding system and map all the coherent combinations on a Poincaré sphere. This technique can be combined with the DSP analysis to extract the amplitude and phase information from the Poincaré sphere. Finally, the HOBBIT and reverse HOBBIT systems are used to sense a dynamic rotating fog density which is made in lab by injecting water steam into a plastic tube. The real-time sensing results show that the HOBBIT and the reverse HOBBIT systems are perfect tools to sense any disturbance of the media. However, the complexity of the media like the fog requires

more detailed measurement in localized and radial positions which will be illustrated in the next chapter.

CHAPTER THREE

THE 2D HOBBIT SYSTEM

3.1 Introduction

In the former chapter, the HOBBIT and the reverse HOBBIT system which can rapidly generate and detect OAM in real-time were introduced. The utilization of AOD in the system allows a fast mode switching rate for generating and correlating linear phases. The induced linear phase can be wrapped into an azimuthal phase gradient from a cartesian to the polar coordinate system. This process is done by two elements called the log-polar optics. The log-polar optics use two phase patterns to do this transformation, the first one to wrap a line into a ring structure and the second one to correct any phase errors during the wrapping and propagation. The generated field by the HOBBIT system is called the asymmetric perfect vortex whose beam size is OAM-independent and can carry both integer and fractional charges. The far-field of the APV is called the asymmetric Bessel-Gauss beams which will be studied in chapter 4 for the nonlinear interaction. The mode switching rate of the HOBBIT is related to the acoustic velocity of the AOD and the incident beam size [11]. The reverse HOBBIT system has the same key elements as the HOBBIT system. The log-polar optics work as mode sorters which unwraps an azimuthal phase gradient into a linear phase gradient and the receiver AOD correlates the linear phase and transforms it into a plane phase. A multi-mode fiber connected with an APD works as a single-pixel detector and the whole system can measure OAM in real-time at a refresh rate of MHz. Since the RF signals driving the transmitter and receiver AODs provide us

the ability to control the mode switching rate, different designs of these signals provide different functions for the system. The AOD-induced Doppler frequency shift is another important feature of using the AOD, and it can be used to generate multiple OAM modes with different amplitudes and phases which enables the construction of the Poincaré sphere. This is very useful in applications that need to encode and decode information in high-dimension. The HOBBIT and the reverse HOBBIT were used to sense the complicated phase information of the rotating fog density. Since the mode switching rate is much faster than the media change and the OAM-independent APV beam sizes, the phase information on the annular structure can be extracted. However, the flowing of the rotating fog density is very complicated and the local phase information might be more important. This leads to the development of the 2D HOBBIT system in this chapter.

Studies using high dimensionality of laser beams show potential and promising applications. For example, in [4] the OAM and the radial modes of the LG beams are used to sense an amplitude structure. With only OAM it is hard to do a similar process since except for APV or PV, most OAM modes have an OAM-dependent beam size. However, a fast mode switching rate is also essential in this process, considering the SLM used in [4] needs over 30 minutes to finish one scan. New efforts to discover new types of beams have been made to enrich the structured light family. These new types include the manipulation of both intensity and phase structures. In [64], Rego et al. developed a method to generate a UV beam carrying time-varying OAM through an HHG by combining two femtosecond (fs) pulses with different OAM, and since the OAM varies extremely fast in fs scale the generated field is also called self-torque which may have promising applications in

nanoscale. The regular OAM beams have a phase distribution on the transverse plane which is perpendicular to the propagation direction and the conventional OAM is called a longitudinal OAM. Different from the longitudinal OAM, the spatiotemporal transverse OAM is demonstrated in [65, 66]. The nonlinear study of the spatiotemporal transverse OAM shows similar OAM conservation law and the generation of multiple-phase singularities [67]. The multiple optical-frequency-comb lines are used to generate dynamic spatiotemporal beams as illustrated in [68] and the generated fields including two independent and controllable OAMs can rotate around the propagation axis. Although new types of structured light show great potential in applications like particle manipulation and information encoding and decoding, relative studies need to be done both theoretically and experimentally.

In this chapter, the beam modal including not only OAM but also a localized degree of freedom with a fast mode switching rate will be developed. The potential solution for this topic involves the use of the HOBBIT concept. The scheme of the 2D HOBBIT system will be introduced which contains two AODs and the log-polar optics. By utilizing not only a localized coordinate mapping, but different lines to rings with different beam sizes are mapped this time. The new AOD introduced to the system is used to control the vertical positions in the log-polar mapping. To manipulate each mode component precisely, a pulse laser as the source will be used and this will eliminate the Doppler effect that caused the phenomenon to some extent. At first, the spatial APV theory analogous to the LG modes with both OAM and radial modes is demonstrated. Then the 2D HOBBIT system will be illustrated in detail. The examples of 11 radial modes and OAM charges as high as 20 will

be demonstrated. A mode switching rate of 406.25 kHz can be realized by the 2D HOBBIT system. By carefully designing the parameters, the mode switching speed can be extended to the MHz level. Some remote sensing scenarios including sensing phase structure, amplitude patterns, and rotating fog density will be used to show the ability of the 2D HOBBIT system. At last, the pulsed 2D HOBBIT system and the reverse HOBBIT system are used to extract the spatial partially coherence information by measuring the cross spectral density (CSD) of a complex field.

3.2 The spatial APV basis

Perhaps the most used OAM modes are the LG beams carrying both OAM and radial modes. As mentioned in [2], the spiraling k vectors of the LG modes can be used to construct a high-dimensional Hilbert space which shows great potential in fields requiring high data rates. Not only the OAM degree of freedom but the radial dimension draw a lot of attention. In [4], both the radial and azimuthal charges of LG beams are used to sense the transmittance function of an amplitude object. In [28], a Gouy phase radial mode sorter is illustrated. The radial dimension of LG beams also shows great potential in quantum technology [69, 70]. In this section, the construction of spatial APV basis with both OAM and radial degrees of freedom will be introduced. Compared to the LG basis, the advantage of APV is that the beam size of APV is OAM-independent which allows the exploration of the effects only caused by OAM. However, the OAM-independent beam size also limits the utilization of APV for localized measurement as shown in the former chapter. Instead, a group of APV with a bunch of different beam sizes to emulate the LG basis can be generated . The spatial APV can be described by

$$APV_{n,\ell}(r,\theta)=\exp\left(-\frac{(r-r_n)^2}{w_r^2}-\frac{\theta^2}{w_\theta^2}\right)\exp(i\ell\theta), \tag{3.1}$$

where n and ℓ represent the radial index and the OAM, r_n is the ring radius for each radial charge, w_r is the $1/e^2$ Gaussian width, w_θ is the $1/e^2$ azimuthal Gaussian width which is closely related to the parameter called asymmetry of the APV. Note that the APV carries fractional and integer OAM with a linear one-to-one correspondence which will be illustrated in the later chapters.

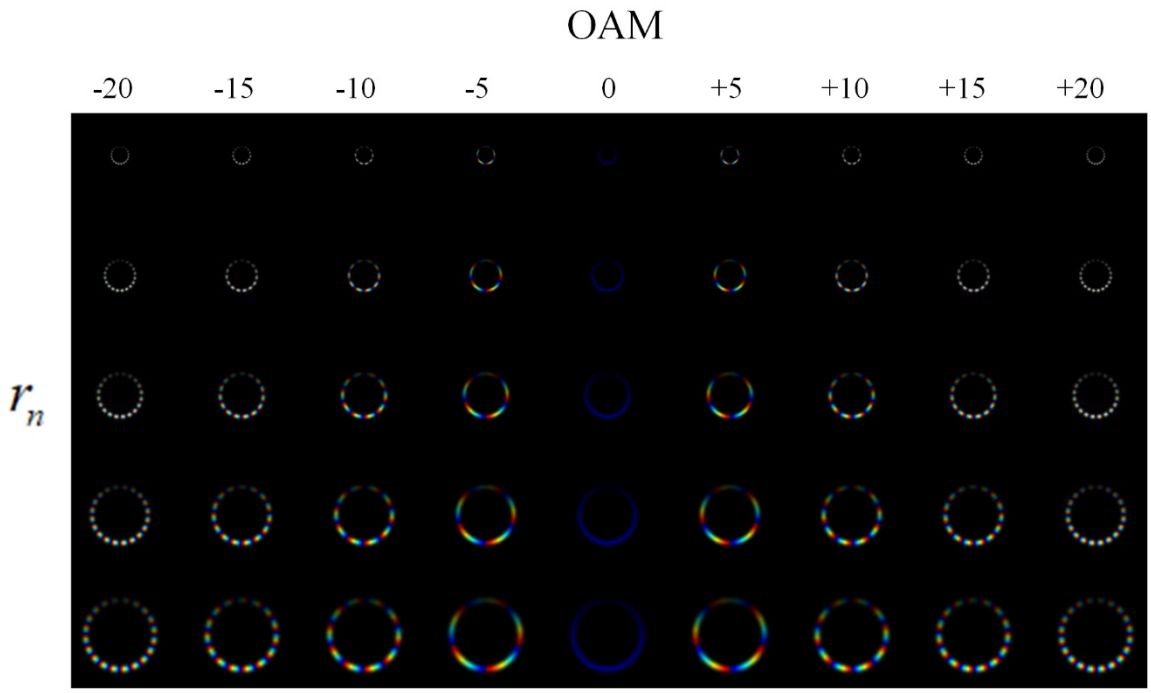

Fig. 3.2.1. The spatial APV basis.

One issue with Eq. (3.1) is that the asymmetry property of APV does not give a purely orthogonal azimuthal basis. As a result, the spatial APV is not an ideal orthogonal basis for describing the space. However, since the applications only require some degrees of freedom, the spatial APV basis is still a very good approximation. Later how to use the

spatial APV basis to sense the complex structure of some media will be demonstrated. In Fig. 3.2.1., some simulation results of the spatial APV modes are shown to illustrate the radial and azimuthal manipulations of the field.

3.3 The 2D HOBBIT system

Considering the generation of LG beams and the mode switching rate is relatively slow, it is necessary to manipulate the spatial APV rapidly for real-time remote sensing tasks. The concept of the HOBBIT system by using AOD and log-polar optics can be used to create spatial APV beams. The HOBBIT system shown in our former work [11] can arbitrarily generate integer and fractional OAM at a very high mode switching speed. However, since the beam size of APV is OAM-independent, the concept of APV needs to be extended to a controllable radial dimension. This function is realized by adding an extra AOD to the HOBBIT system. The 2D HOBBIT system is shown in Fig. 3.3.1(a). The source used in the system is a 517 nm pulsed laser (Coherent, Monaco) whose pulse width is 242 fs. The first AOD adds a vertical linear phase to the incident beam. This linear phase is Fourier transformed by a cylindrical lens labeled with a focal length of $F_2 = 500\,mm$ in the figure and in the Fourier plane, this linear phase becomes a linear shift. Then by driving the first AOD with different frequencies, the vertical position of the beam can be controlled. The second AOD has the same function as illustrated in the former chapter and it works as the OAM generator. The second AOD deflects the incident beam horizontally which corresponds to a horizontal phase gradient and this linear phase will be imaged to the first log-polar optics by two cylindrical pairs which work as a 4-f imaging system to reshape the beam. The focal lengths of the cylindrical lens pair are $F_1 = 50\,mm$ and

$F_3 = 250\,mm$. After the 3 cylindrical lenses, the incident Gaussian beam becomes an elliptical Gaussian beam with a horizontal linear phase. The log-polar optics include two elements, one to do an optical geometric transformation and locates at the Fourier plane of F_2 and F_3, and the other one which is at the Fourier plane of the first element to correct any errors in the wrapping process. Based on the log-polar coordinate mapping, vertical positions correspond to different radial scales. As shown in Fig. 3.3.1(b), two elliptical Gaussian beams with different colormaps are incident at the first log-polar element, and after the wrapping procedure, two ring structures with different radiuses are generated. For precise control of the generated field, the laser pulse and the two RF signals driving the two AODs are synchronized.

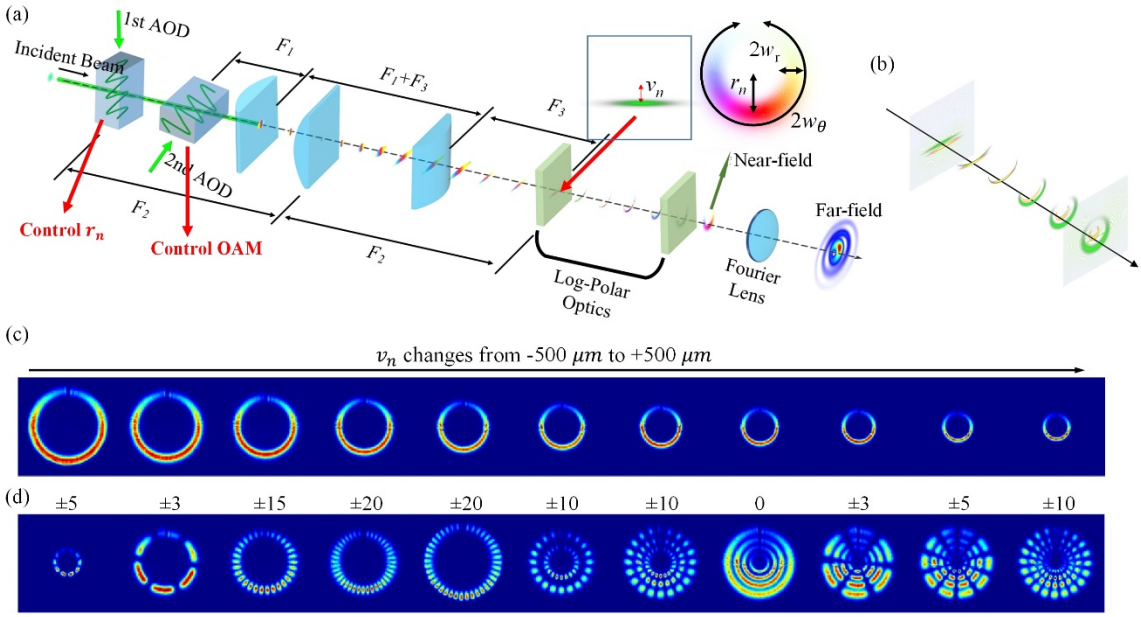

Fig. 3.3.1. (a) The 2D HOBBIT system. (b) The log-polar coordinate transformation for the spatial APV generation. (c) Experimental results of spatial APV with different r_n. (d) Experimental results of multiple radial and OAM modes generation.

The experimentally generated radial and OAM modes are shown in Fig. 3.3.1(c-d). By designing the RF signals, single or multiple radial and azimuthal modes can be generated. Due to the use of an ultrafast pulsed laser, the short period of a pulse is too short to show any oscillations caused by the Doppler frequency shift, compared to the results in the former chapter. As a result, the interference pattern of the coherent combination of OAM modes can be observed in the experimental results. As high as OAM charge 20 can be generated from the 2D HOBBIT system where the ± 20 shows the typical interference pattern with a total number of 40 petals. From Fig. 3.3.1(d), multiple ring structures that correspond to the generation of multiple radial modes can be observed.

The RF signal will be given first. Similar to the one demonstrated in the former chapter, here the RF signals are needed to drive the two AODs. The two RF signals can be described as follows:

$$S_n(t) = c_n \sin\left(2\pi f_n(t)t + \phi_n\right), \tag{3.2}$$

$$S_\ell(t) = c_\ell \sin\left(2\pi f_\ell(t)t + \phi_\ell\right), \tag{3.3}$$

where c_n and c_ℓ are the coefficients of each frequency component in the RF signal, $f_n(t)$ and $f_\ell(t)$ are the frequency functions in the sine waves, ϕ_n and ϕ_ℓ are the initial phases for each sine wave. The RF signals can be any combination of different frequency functions which are used to generate a coherent combination of different modes. Same to the HOBBIT concept, the RF signal has an arbitrary form to generate specific modes.

The RF signals $S_n(t)$ and $S_\ell(t)$ can be used to control the generated field which has a spatiotemporal feature. For the first AOD, it adds a linear phase to the incident beam vertically and after the Fourier transform by the cylindrical lens F_2, in the Fourier plane, the vertical linear phase is transferred to a vertical linear shift. The vertical linear shift can be described as v_n which is the distance of the incident beam away from the center of the first log-polar optics and can be represented by

$$v_n = \frac{\lambda_n F_2}{V_{at}}\left(f_{AOD} - f_n(t)\right), \tag{3.4}$$

where λ_n is the new wavelength after the first AOD which is caused by the Doppler effect, $V_{at} = 0.65\,mm/\mu s$ is the acoustic velocity, $f_{AOD} = 75\,MHz$ is the AOD central driving frequency. Note that the Doppler frequency shift caused by the AOD still exists in the system, but the use of a short pulse will allow us to see the interference patterns of the coherent modes.

The ring radius of the spatial APV can be described by the vertical linear shift v_n as follows:

$$r_n = b\exp(-v_n / a), \tag{3.5}$$

where $a = \frac{6\,mm}{2\pi}$ and $b = 1.5\,mm$ are the designed parameters of the log-polar optics.

After the first AOD, the beam is deflected by the second AOD horizontally and the generated horizontal linear phase will be mapped to the azimuthal phase gradient by the log-polar optics. This process is demonstrated in the former chapter and in [11]. The generated OAM is related to the RF frequency and can be described by

$$\ell = \frac{2\pi a}{V_{at}\eta}\left[f_{AOD} - f_{\ell}(t)\right], \tag{3.6}$$

where $\eta = \frac{F_3}{F_1}$ is the amplification rate of the lens system and $f_{\ell}(t)$ is the frequency used to generate OAM charge ℓ.

The log-polar optics map the incident elliptical Gaussian beam into the spatial APV, and the spatial APV can be described by

$$APV_{n,\ell}(r,\theta,t) = \hat{x}\exp\left(-\frac{(r-r_n)^2}{w_r{}^2} - \frac{\theta^2}{w_\theta{}^2} - \frac{(\tau - t)^2}{\Delta\tau^2}\right)\exp\left(i2\pi\left(f_c + f_n(t) + f_{\ell}(t)\right)t - ik_z z\right)\exp\left(i\ell\theta\right), \tag{3.7}$$

where $\hat{x}$ describes the horizontal polarization, $w_r = \frac{w_v r_n}{a}$, w_v is the half-width of the elliptical Gaussian beam in the vertical direction, w_θ is the ratio of the line length of the elliptical Gaussian beam to $2a$ and has a value of 1.3π in the 2D HOBBIT system, τ is the local time for the pulse, $\Delta\tau$ is the pulse duration, and f_c is the frequency of the incident light, $k_z = 2\pi\cos\left(\lambda_{n\ell}\ell / 2\pi a\right)/\lambda_{n\ell}$ is the longitudinal wave vector and $\lambda_{n\ell}$ is the wavelength after the two AODs. The utilization of a short pulse enables us to program the radial and OAM modes in each pulse and then a group of pulses can be chosen to create a pulse train used for remote sensing applications.

In Fig. 3.3.1(c), 11 radial modes are shown with beam diameters changing from 5.06 mm to 1.78 mm. The relative v_n changes from -500 μm to +500 μm according to Eq. (3.5). The far-field, the asymmetric BG beams, usually work as the correlation points

when measuring any phase disturbance since the phase of a complex media will change the OAM spiral phase back to a plane phase. The intensity distribution of the APV and their relative far-field is shown in Fig. 3.3.2.

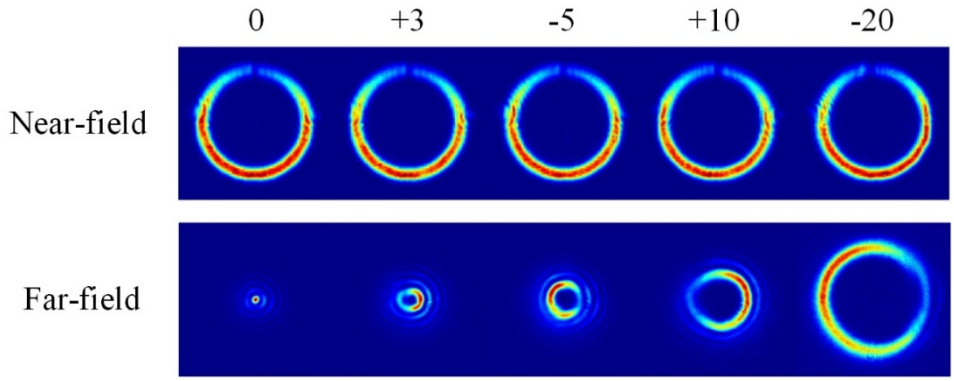

Fig. 3.3.2. Intensity distributions of the APV and the relative far-fields carrying different OAM [71].

From Chapter 2, for complex media such as the rotating fog density, the particles will create a refractive index distribution. By using a localized measurement, more information about a complex distribution can be recovered. In the former several paragraphs, the generation of the spatial APV with both radial and azimuthal manipulation has been introduced. However, it will be beneficial if another degree of freedom, the azimuthal position can be introduced to the beam model. Next, how to generate spatial APV with more asymmetry and how to rotate the beam around the annular ring by designing the appropriate RF signal driving the AODs will be shown.

When the acoustic wave generated by the RF signals propagates through the AOD, it will modulate and deflect the incident beam. The acoustic wave can be considered as a traveling wave during that time window. Then the digital signal processing (DSP)

technique can be used to control the RF signal and the generated acoustic wave will have the same features as the DSP methods. For example, a Gaussian filter can be exploited to work on the sine waves and the RF signal will become a wavelet-like waveform. And if time delays are added to the Gaussian filter, the acoustic wave will modulate different spatial locations on the incident beam. This process is illustrated in Fig. 3.3.3. In the first row, the RF signal which has a sinusoidal form, the elliptical Gaussian beam incident at the first log-polar optics, and the wrapped APV after the log-polar elements are shown. Then a Gaussian filter filtering the sine wave at different time points corresponds to rows 2-6. The relative elliptical Gaussian and azimuthal APV beams are given.

By combining the azimuthally localized wavelet-like APV beams and the radial manipulation of the first AOD, the azimuthal phase gradient across the transverse plane in the polar coordinate system can be measured. This procedure is basically to decompose the transverse phase distribution into the OAM basis, which is similar to the methods used in optical communications which analyze the OAM spectrum after the OAM beams propagate through the atmospheric turbulence. Compared to the experiment demonstrated in chapter 2 measuring the rotating fog density, now the localized phase information with the radial, azimuthal, and OAM control can be measured. The phase measurement resolution will be greatly enhanced by using this method. More detailed experimental results and analyses will be given in the following sections.

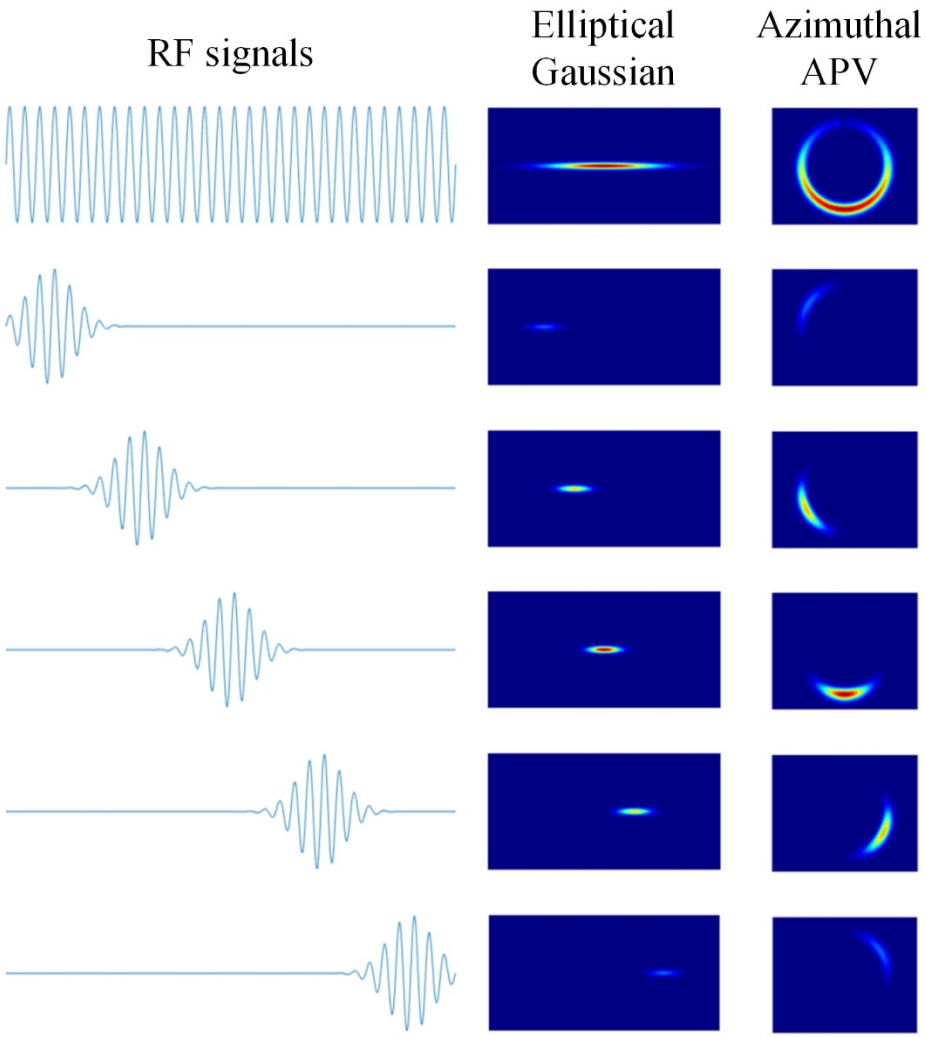

Fig. 3.3.3. Using filtered RF signal to generate azimuthally localized APV.

The same as the HOBBIT and reverse HOBBIT systems, one advantage of the 2D HOBBIT system is the fast mode switching speed. The mode switching rate is determined by the acoustic velocity of the AODs and the beam size propagating through the AODs. In the 2D HOBBIT system, the incident Gaussian beam has a typical beam diameter of 1.6 mm and the acoustic velocity is 0.65 $mm/\mu s$ which lead to a mode switching rate of 406.25 kHz. The mode switching rate can be further improved by changing the parameters

of the setup. However, this mode switching speed is much faster compared to most dynamics of the complex media. In the next section, two remote sensing scenarios will be illustrated to show how to use the spatial APV pulse train to sense phase and amplitude objects.

3.4 Sensing amplitude object using the spatial APV

Previous work describing amplitude pattern recognition using the LG basis including radial and OAM modes is illustrated in [4]. A sequence of laser beams carrying different radial and azimuthal information propagates through an amplitude object, and by collecting the transmitted power the complex coefficients for all the modes are calculated. Four measurements are used to determine one complex coefficient for each mode and the amplitude and phase of the LG modes are used to reconstruct the transmission function of the amplitude object. However, in this reference, the LG beams are generated by an SLM whose mode switching rate has a typical value of 60 Hz. The sequence includes 31 different radial modes and 31 different OAM modes which results in the period for one scan taking more than 30 minutes. This time is too long to fulfill the requirement of real-time sensing. The 2D HOBBIT system has a much faster mode switching rate which can be used to do real-time pattern recognition and the extension from a regular APV to a spatial APV also provides the ability to scale the beam basis. In this section, the detailed theory of using the spatial APV to do the amplitude pattern recognition will be illustrated. The construction of the spatial APV pulse train will also be demonstrated.

The spatial APV pulse train is a sequence of pulses each one carries a specific radial and OAM information. However, four pulses are required to get the complex coefficient

for these specific radial and OAM modes. With this radial and OAM information, a reference is used in each pulse to give the interference and in the four pulses, the reference carries four phase differences compared to the radial and OAM mode: 0, 0.5π, π, 1.5π. Then the complex coefficient can be calculated by Eq. (3.8). The transmitted power values, $P_{n,\ell,0}$, $P_{n,\ell,0.5\pi}$, $P_{n,\ell,\pi}$, $P_{n,\ell,1.5\pi}$, are collected by a power meter and used to calculate $C_{n,\ell}$.

$$C_{n,\ell} = P_{n,\ell,0} - P_{n,\ell,\pi} + i\left(P_{n,\ell,0.5\pi} - P_{n,\ell,1.5\pi}\right). \tag{3.8}$$

Then the transmission function of the amplitude object can be reconstructed by summing all the spatial APV modes with their complex coefficients,

$$O = \sum_{n,\ell} C_{n,\ell} APV_{n,\ell}. \tag{3.9}$$

The sensing process is illustrated in Fig. 3.4.1(a). The amplitude object is several 3D printed letters. The whole pattern has a size of 80 mm by 30 mm, and the height of each letter is about 10 mm. Since the real-time property of the 2D HOBBIT system, the amplitude object is moved horizontally across the beam. In the figure, two groups including 8 pulses are used to show the interference patterns of the OAM modes and the reference beam. Only one radial mode is chosen to illustrate this method. In this figure, the parameter Δt is closely related to the repetition rate of the laser. A total number of 3280 pulses are used to create this spatial APV pulse train. This pulse train includes 20 radial modes (diameters from 3 mm to 12 mm changing linearly) and 41 OAM modes (integer charge from -20 to +20). A telescope with a 3X magnification is used to expand the beam size. When there is no amplitude object in the light path, the spatial APV pulse train should be able to get a transmission matrix with ones. However, since the asymmetric property of our

beam, the recovered pattern is also asymmetric as shown in Fig. 3.4.1(b). The simulated and experimental results are illustrated. A high-speed camera (Phantom Miro C110) is used in the experiment to work as the power meter and the captured gray-scale picture is used as the power values. In the experiment, a laser repetition rate of 1kHz is used. In Fig. 3.4.1(c), the reconstructed amplitude transmission function of the letters "OPTICA" is shown. Since the object moves across the beam, a total number of 11 scans are recorded. We can see the shapes of all the letters are recovered perfectly.

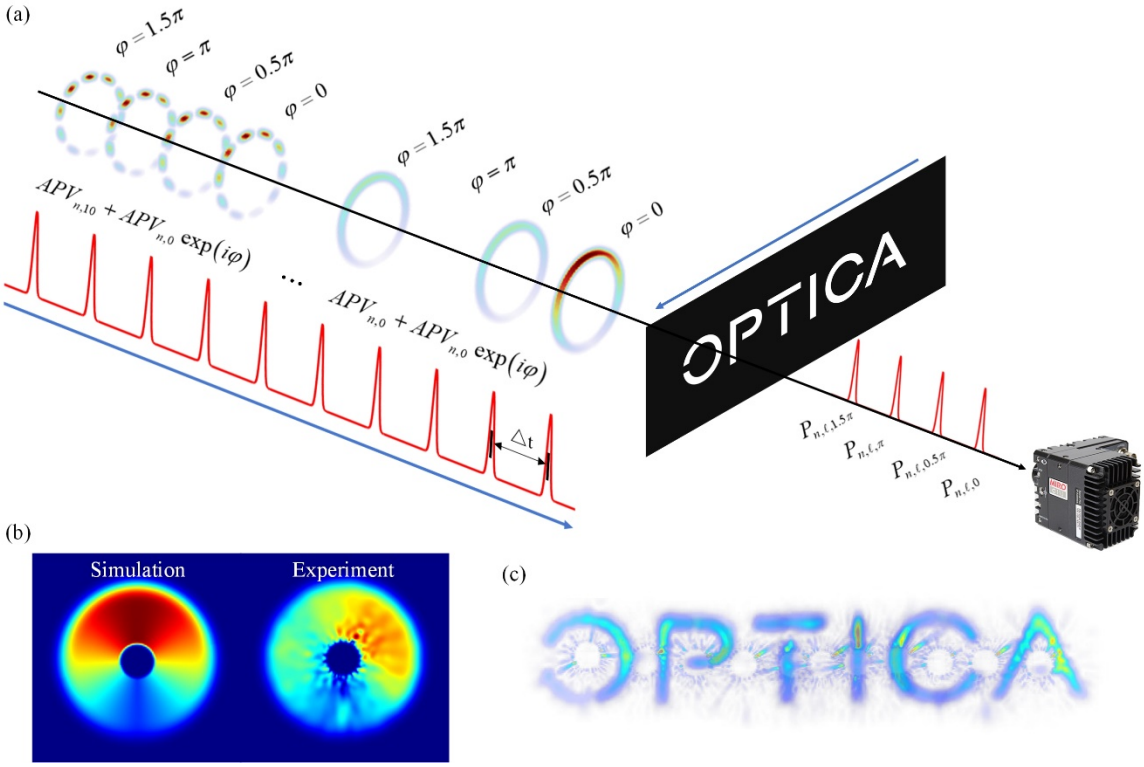

Fig. 3.4.1. (a) The amplitude object sensing procedure using the spatial APV pulse train. (b) The reconstructed transmission function without the amplitude object. (c) The reconstructed amplitude object "OPTICA" experimentally [71].

The spatial APV pulsed train for amplitude transmission function sensing is much faster than the SLM-based method. In our experiment, a 1 kHz repetition rate is used and it takes about 3s to finish one scan. One issue of the spatial APV is that the basis does not include a mode to fill the central area of the transverse plane. This can be observed from the simulated and experimental results in Fig. 3.4.1(b). However, with a continuous scan, the central region can be detected by the next scan and when the scanned results are overlapped and processed, the recovered pattern shows very good consistency with the original amplitude object. Based on the radial ring sizes and the OAM charges used in this pulse train, the spatial resolution can be determined by the spacing of radial modes and the interference pattern of the OAM and the reference. In the experiment, the resolutions in radial and azimuthal directions are calculated as 0.24 mm and 0.1π. Note that the 2D HOBBIT system is not limited to these exact radial and OAM numbers and the resolution and the detection speed can be further enhanced by optimizing the whole process.

3.5 Sensing rotating fog density using the spatial APV

In chapter 2, examples of using the HOBBIT and the reverse HOBBIT systems to sense the dynamics of the rotating fog density in real-time are shown. The water steam flows into a plastic tube tangentially and rotates inside the tube. Because when there is a fog density difference across the transverse direction of the tube, the rotating fog results in a refractive index distribution which will add an extra OAM component to the input beam. The global OAM was traced by the reverse HOBBIT and the collected OAM spectrogram is quite complicated and the OAM spectrum shows multiple peaks. These results reflect the complexity of the rotating fog and if we want to know more information about the

complex media, the localized measurement is necessary. In this chapter, the development of the 2D HOBBIT system which can manipulate the radial and OAM information per pulse has been introduced, and the RF signals driving the AODs can be modulated by the DSP methods and the generated modes can be further tailored. When using a Gaussian-shape filter to work on the RF signal, the wavelet-like waveforms can be created and the acoustic waves stimulated by these wavelet-like waveforms will only function on part of the incident beam. Specifically, only a part of the elliptical Gaussian beam will be incident at the log-polar optics and mapped to a localized azimuthal position. This small part of the APV ring still can carry the OAM information. Combined with the radial control, the generated modes by the 2D HOBBIT can cover the transverse plane in the polar coordinate. These modes enable us to sense the rotating fog density locally. In the experiment, the size of the Gaussian filter is 1/4 of the ring circumference which corresponds to a spiral bandwidth of OAM 5 with both sides of the picked OAM value.

The fog generator is similar to the one used in chapter 2. The length of the tube is 1 m and three pipes are stretching into the wall of the tube tangentially with equalized spacing. The water steam is pumped into the tube through these pipes by an ultrasonic source. The experimental setup of the tube for generating fog rotating in clockwise and counter-clockwise directions is shown in Fig. 3.5.1. By simply flipping the tube the rotating direction of the fog can be changed.

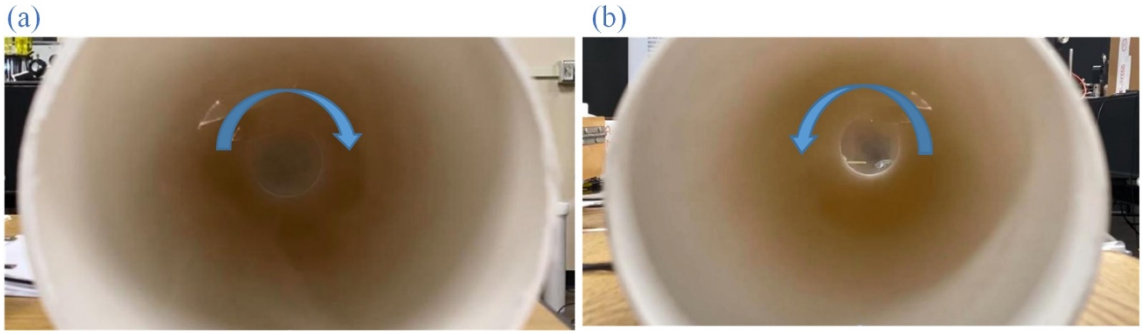

Fig. 3.5.1. The tube for generating the rotating fog density in clockwise and counter-clockwise directions.

To show the localized measurement simply and directly, here only one radial diameter of the APV will be used to illustrate the method. The 3D illustration can be seen in Fig. 3.5.2. The azimuthal and OAM information are encoded on the beam pulse by pulse. As a result, in 3D space, the light trace will be like a spiraling curve. This pulse train includes 20 azimuthal positions (from 0 to 2π with equal spacing) and 33 OAM states (from -4 to +4 with a step of 0.25). Since from the results measured in chapter 2, the OAM components added by the rotating fog usually fall in a range of ± 4, a small range is chosen and the fractional OAM is used to get a high-resolution of the phase measurement. The scanning procedure is as follows, the 33 OAM states are sent at the first azimuthal position, and then the 33 OAM states will be sent at the second azimuthal position. To finish one scan, a total number of 660 pulses is required in this pulse train. After the pulse train propagates through the rotating fog density, a reducing telescope is used to change the beam size which is not shown in the figure. Then a Fourier lens is used to do the correlation measurement. When the phase information in the fog density correlates with the OAM carried by the APV, there will be a bright spot on the axis. An ultrafast camera is used to

collect all the beam intensity distributions. The laser repetition rate used in this scheme is 3.5 kHz.

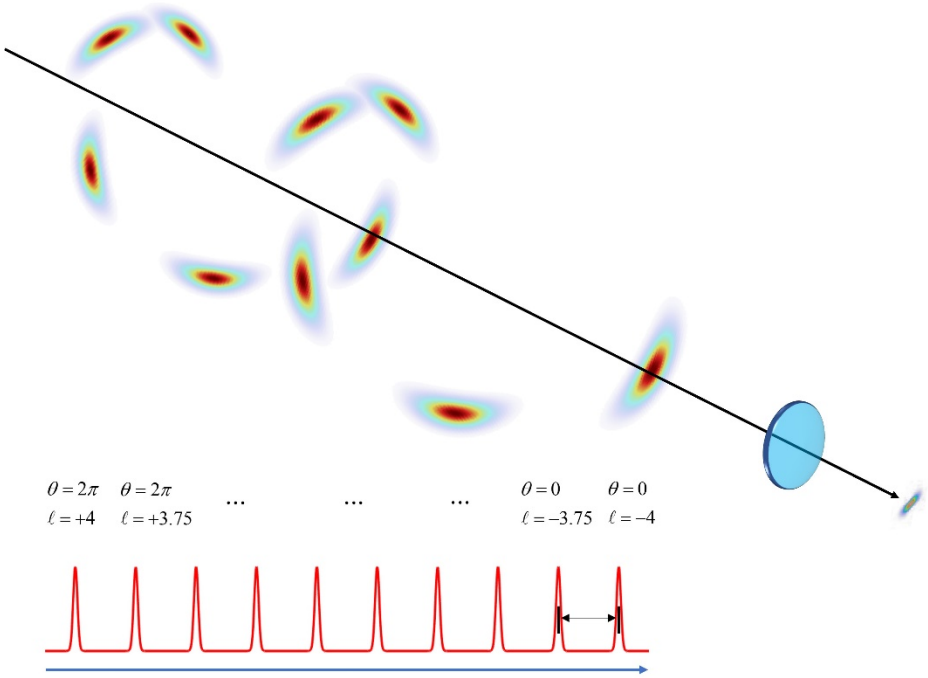

Fig. 3.5.2. The spatial APV pulse train for localized phase measurement.

The experimental results are shown in Fig. 3.5.3. The sensing results measuring the clockwise rotation of the fog density at several time points are shown in Fig. 3.5.3(a). The first row is the measured OAM spectrogram where the y axis denotes the OAM spectrum and the x axis represents the 20 azimuthal positions. From the result at different azimuthal positions the measured OAMs are different which proves our prediction in chapter 2 is correct. The second row is the reconstructed OAM information on the annular ring. The colorbar on the bottom right tells the correspondence of the colors and the OAM. The color information or the OAM here in fact tells the phase gradient across the azimuthal direction. Based on this measurement result, the phase distribution on this annular structure can be

recovered. The counter-clockwise measurement results are shown in Fig. 3.5.3(b) which give similar results.

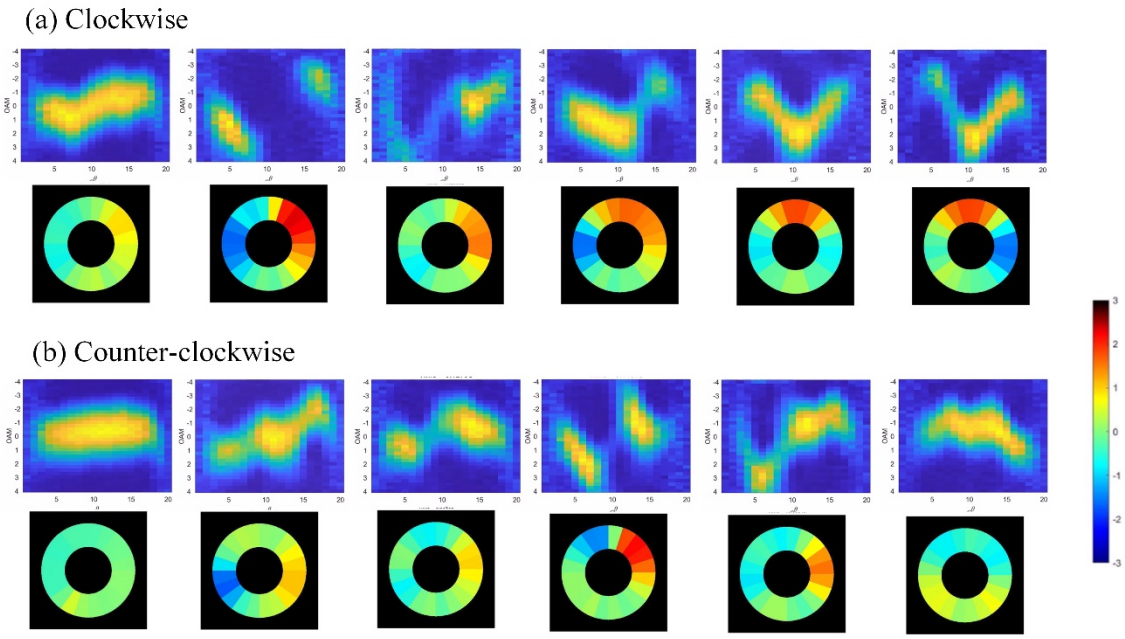

Fig. 3.5.3. The rotating fog density sensing results with the localized measurement.

The rotating fog density has very complicated and unrepeatable dynamics which is hard to get the information directly. In chapter 2, the HOBBIT and the reverse HOBBIT systems were used to sense the OAM changing with time. The results in chapter 2 traced the global OAM change and gave a complicated OAM spectrum. Since the fog density may cause a refractive index distribution across the transverse plane, measuring the global channel information may not be able to provide detailed information. The measured OAM spectrogram indicated that a localized measurement is necessary to extract the phase distribution of the rotating fog density. The 2D HOBBIT system can generate not only OAM and radial modes but also a small portion of the APV at different azimuthal positions carrying OAM. This feature enables us to do localized measurement of the phase

distribution. The measured OAM spectrograms and the recovered phase/OAM gradient information prove the correctness of our prediction. The sensing speed is in real-time which is another important feature of the HOBBIT-based concept. Future work will involve multiple radial position sensing which will allow us to reconstruct the whole phase structure across the transverse plane.

3.6 Partial coherence measurement

In former sections 3.5 and 3.6, the spatial APV basis is used to sense the binary amplitude pattern and the phase spectrum of a concentric phase plate. The results show the features of the objects. However, a complex object may change the inherent properties of the light field, such as the spatial coherence. The characterization of spatial coherence using the HOBBIT system will be demonstrated in this section. The spatial coherence of a random light source refers to the correlation of any two points in the light field. It is quantified by the CSD function and hard to measure directly from the light's intensity distribution. The spatial coherence shows great potentials in applications such as optical communications [72], optical coherence tomography (OCT) [73], imaging [74], and particle manipulation [75]. Then it is essential to measure the spatial coherence of a light field fast and accurately. However, since the CSD has a complex distribution, in most cases, an interferometer scheme and multiple measurements [76-78] are required to detect the CSD. Considering the spatial property of the proposed beam model, the spatial APV with azimuthal manipulation generated by the HOBBIT might provide a new and rapid way to characterize the spatial coherence information when the spatial APV propagates through a complex media. Besides the programable property of the HOBBIT system also makes it

possible to design a beam with a specific spatial coherence distribution. In this section, the basic concept and measurement method will be introduced, then a four-shot measurement method based on the 2D HOBBIT and reverse HOBBIT is proposed. Simulation and experimental results will be given.

According to [79], any type of partially coherent beams can be considered as a superposition of mutually orthogonal and coherent optical fields. The partially coherent beam can be described by,

$$PCB = \sum_{n,m} C_{n,m} \Phi_{n,m}, \tag{3.10}$$

where $\Phi_{n,m}$ is the orthogonal modes, $C_{n,m}$ is the relative coefficient, and n and m can be considered as radial and azimuthal numbers if OAM is used as the basis.

Then the CSD function can be expressed as,

$$W(r_1, r_2, z) = \sum_{n,m} \lambda_{n,m} \Phi^*_{n,m}(r_1, z) \Phi_{n,m}(r_2, z), \tag{3.11}$$

where r_1 and r_2 are the radial positions of the two measured points, $\lambda_{n,m}$ is the coefficient for each component.

From Eq. (3.11), we can conclude that the CSD is the multiplication of the complex amplitude of one point with the complex amplitude conjugate of the other point. Now, it will be how to measure the CSD of an arbitrary complex field. If an interferometer is built to make the complex amplitudes of the two points interfere, the interfered field can be described as,

$$\Phi_{out} = \lambda_1 \Phi(r_1, z) + \lambda_2 \Phi(r_2, z) \exp(i\delta), \tag{3.12}$$

where δ is the phase difference between the complex amplitudes of the two points which can be changed by using an Michelson interferometer and changing the lengths of the two legs.

Then the intensity of the output field can be described as,

$$\begin{aligned} I_{out} &= \Phi_{out}^{*}\Phi_{out} \\ &= \lambda_1^2\Phi^{*}(r_1,z)\Phi(r_1,z)+\lambda_2^2\Phi^{*}(r_2,z)\Phi(r_2,z) \\ &\quad +\lambda_1\lambda_2\Phi^{*}(r_1,z)\Phi(r_2,z)e^{i\delta}+\lambda_1\lambda_2\Phi(r_1,z)\Phi^{*}(r_2,z)e^{-i\delta} \\ &= \lambda_1^2 I(r_1,z)+\lambda_2^2 I(r_2,z)+\lambda_1\lambda_2 W(r_1,r_2)+\lambda_1\lambda_2 W^{*}(r_1,r_2) \\ &= \lambda_1^2 I(r_1,z)+\lambda_2^2 I(r_2,z)+\lambda_1\lambda_2\left(\mathrm{Re}\left(W(r_1,r_2)\right)\cos\delta-\mathrm{Im}\left(W(r_1,r_2)\right)\sin\delta\right). \end{aligned} \tag{3.13}$$

From Eq. (3.12), we can see the CSD information is embedded in the interference of the two points in the beam profile. By choosing a series of phase values δ, the CSD information can be recovered from several intensities captured by a CCD camera. The changing of the phase δ can be realized by accurately controlling the leg lengths of the interferometer. When the phase δ takes the values of 0 and π as shown in [78], two intensity values are collected from the interference patterns. The intensity difference can be described as Eq. (3.14). The real part of the CSD function can be extracted from the result.

$$\Delta I_1 = I(\delta=0)-I(\delta=\pi)=2\lambda_1\lambda_2\,\mathrm{Re}\left(W(r_1,r_2)\right). \tag{3.14}$$

Similarly, if the phase δ takes the values of $0.5\,\pi$ and $1.5\,\pi$, the intensity difference is described as Eq. (3.15) and the imaginary part of the CSD can be extracted.

$$\Delta I_1 = I(\delta=1.5\pi)-I(\delta=0.5\pi)=2\lambda_1\lambda_2\,\mathrm{Im}\left(W(r_1,r_2)\right). \tag{3.15}$$

How to measure the CSD of any beam has been shown above, but building an interferometer and changing the phase difference between the two legs require accurate mechanical control and are time-consuming. Fortunately, our HOBBIT system shows an ability to do rapid mode manipulation and two parts of the beam can interfere with arbitrary and precise phase differences using the technique shown in Fig. 3.3.3. The concept of using the 2D HOBBIT and the reverse HOBBIT is shown in Fig. 3.6.1. The pulsed 2D HOBBIT is used to generate the probe beams, and send it through the reverse HOBBIT system. Two positions on the ring shown in Fig. 3.6.1(a) are to be measured. The probe beam may propagate an arbitrary complex medium and gain some type of partial coherence. The ring structure of the beam will be mapped to a line, based on the former knowledge. By tailoring the RF signal driving the receiver AOD as shown in Fig. 3.6.1(c), two beamlets will be deflected and interfere at the interference plane. The position 1 works as a fixed point and the position two works as a scanning point. A total number of 30 positions are chosen in the simulation. As a result, the CSD of point 1 and other positions across the ring will be measured. A simulated example of the four-shot measured intensity distributions with the four phase values is given in Fig. 3.6.1(d). By extracting the intensity values in the center from the four intensities, the CSD can be calculated and the phase information can be recovered using Eq. (3.16).

$$\varphi = \tan^{-1}\left(\frac{I\left(\delta = 1.5\pi\right) - I\left(\delta = 0.5\pi\right)}{I\left(\delta = \pi\right) - I\left(\delta = 0\right)}\right). \tag{3.16}$$

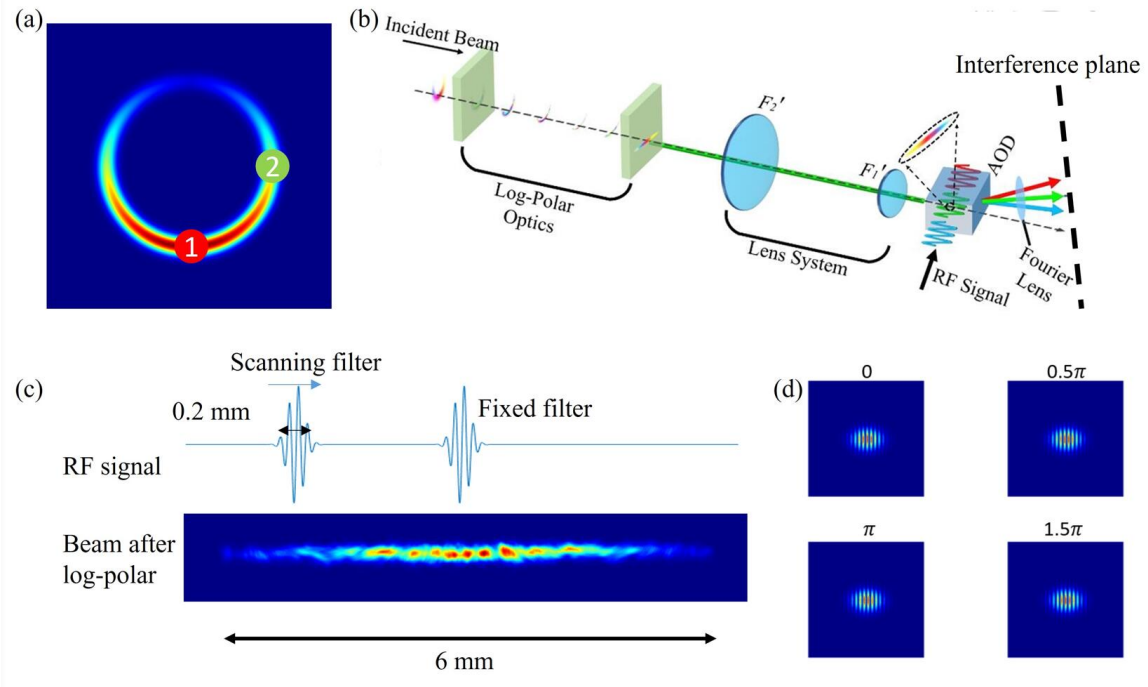

Fig. 3.6.1. The partial coherence measurement using the HOBBIT.

The simulation results of measuring the CSD and phase of OAM 0 and 5 are shown in Fig. 3.6.2. The first and second columns show the real and imaginary parts of the CSD function. Since the APV is unwrapped to a line shape, a vector is used to represent the CSD function. The third column is the recovered phase around the ring based on the real and imaginary parts of the CSD. The phases of OAM 0 and 5 are recovered with an unexpected fluctuation. This fluctuation is due to the uncertainty relation between the position and the phase. With a larger filter size, the curve shown in Fig. 3.6.2. will be more linear. However, the phase resolution will be compromised.

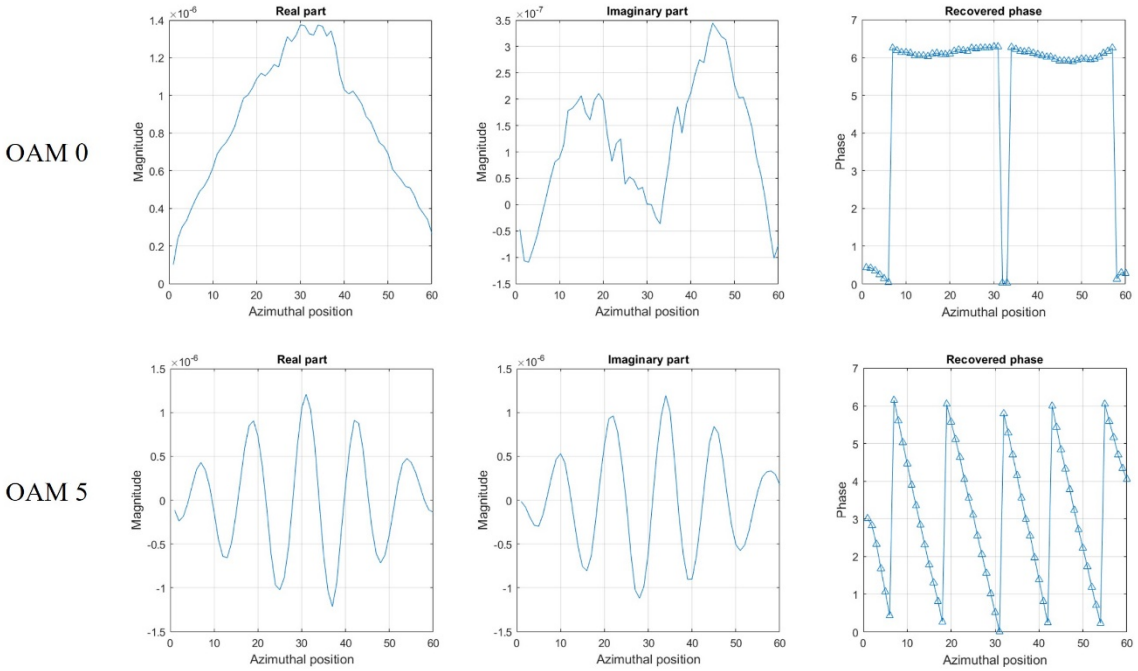

Fig. 3.6.2. The simulated CSD and phase measurement of the OAM 0 and 5.

The experimental results are shown in Fig. 3.6.3. A laser repetition rate of 10 kHz is used, an azimuthal position number of 60 are chosen, and a filter size of 0.48 mm is used. This filter size is to avoid the low intensity caused measurement errors. The similarities of the shape of the curves between the simulation and the experiment can be seen. Because of the small filter size, a small ratio of the intensity is deflected, resulting in a poor signal-noise ratio (SNR). However, when the scanning filter moves close to the fixed filter, the power density of the interference is very low, causing issues to detect the CSD and recover the phase which can be observed from the results. The recovered phase of OAM 5 shows five regions indicating the winding number of the charge but the phase curve is not as good as the simulation. This is due to several parameters including the beam quality, alignment, SNR and the trigger accuracy of the RF signal.

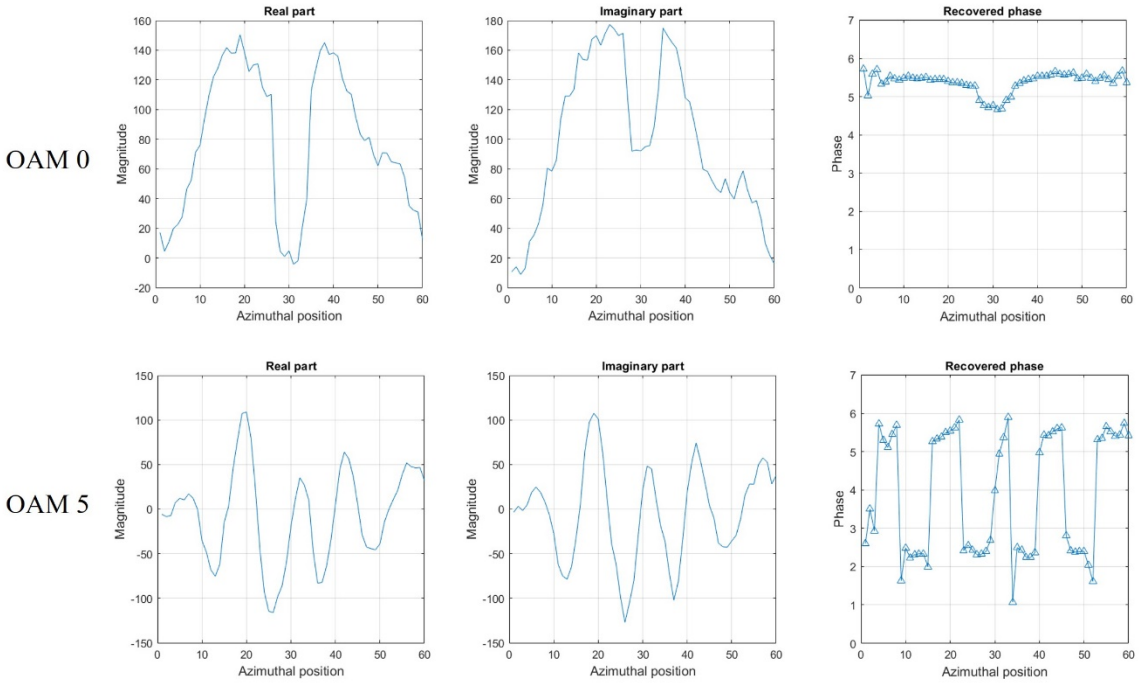

Fig. 3.6.3. The experimental CSD and phase measurement of the OAM 0 and 5.

In this section, the theory and experimental results of the CSD and phase measurements of an OAM beam have been demonstrated. This method can be used to characterize the partial coherence information rapidly, compared to other interferometer schemes. By measuring the interference of two points in the light field with designed phase difference, the real and imaginary parts of the CSD can be measured through a four-shot measurement. Then the measured CSD is used to recover the phase. Our results fit well with the simulation results. The current performance of this method is limited by the beam quality, filter size, alignment, and SNR. Further improvement may be to change the filter method to the whole beam interference by deflecting the beam to different angles with a phase difference.

3.7 Summary

In this chapter, the spatial APV basis which can be used to do localized measurement was demonstrated. The spatial APV is analogous to the LG basis which not only has the OAM degree of freedom, but also the radial dimension control. The LG basis is a good tool to sense the transverse structure. To do similar sensing tasks, the 2D HOBBIT system was developed to generate the spatial APV. The spatial APV basis is a group of APV with controllable beam diameters. Compared to the HOBBIT and the reverse HOBBIT systems, two AODs are included in the 2D HOBBIT system. The first AOD adds a vertical linear phase to the incident beam and this vertical linear phase is transferred to a vertical linear shift at the Fourier plane of a cylindrical lens. The first log-polar optics locates on this Fourier plane and wraps beams at different locations to different ring sizes. The second AOD does the same task as the one in the HOBBIT system which deflects the beam horizontally and after this horizontal phase gradient is imaged by two cylindrical lenses to the first log-polar optics, the incident Gaussian beam becomes an elliptical Gaussian beam. 11 radial modes and OAM charge as high as 20 are shown experimentally as examples. Because of the use of the short pulsed laser source, the Doppler effect caused intensity distribution is overcome and the clear interference pattern for coherent OAM can be observed in the fields. The mode switching rate of the 2D HOBBIT system is rapid which is related to the acoustic velocity of the AODs and the beam size in the AODs. A theoretical value of 406.25 kHz can be realized using the current setup but can be further improved by optimizing the system parameters. Since the use of AODs, the RF signal driving the AODs and the waveforms can be modulated and filtered using the DSP

technique. By using a Gaussian filter which has a size of 1/4 of the ring circumference, the wavelet-like RF signals which will only deflect part of the incident beam can be created. The final beam is a highly asymmetric APV whose intensity can rotate along the annular direction by changing the delay of the wavelet-like signal. The Gaussian filter size provides an OAM spiral bandwidth of 5 around the picked OAM value for the wavelet-like beam. More work on how to choose the filter size based on different media will be studied in the future. The OAM, radial control, and the wavelet-like APV enable us to do local phase measurement in real-time.

The spatial APV basis was used to illustrate how to reconstruct the transmission function of an amplitude object. By using the same method with LG beams, each radial and OAM mode is sent four times with a reference beam carrying four phase values, 0, 0.5 π, π, 1.5π. The transmitted power was collected by a fast camera and the four values determined a complex coefficient for a specific mode. By creating a spatial APV pulse train including a group of radial and OAM modes, a group of complex coefficients which were used to reconstruct the amplitude transmission function can be retrieved. A 3D printed pattern having the letters "OPTICA" was recovered by this method. A total number of 3280 pulses, including 20 radial modes and 41 OAM states, are used to sense the amplitude object. A 1 kHz repetition rate was used leading to 3 s to recover the information in one scan. The measurement speed can be greatly enhanced by using a higher repetition rate.

Then the spatial APV pulse train including OAM and localized position control was used to sense the rotating fog density. As demonstrated in chapter 2, the phase distribution generated by the density difference across the whole transverse plane is very complicated,

and measuring the global OAM may not reflect the detailed information about the channel. Using the designed spatial APV pulse train, the OAM spectrogram based on different azimuthal positions can be measured and then recover the OAM/phase gradient distribution based on the OAM spectrogram. The measured results proved our prediction of the complexity of the rotating fog density. A total number of 660 pulses are included in this pulse train containing 20 different azimuthal positions (from 0 to 2π with equal spacing) and 33 OAM states (from -4 to +4 with a step of 0.25). The choosing of the OAM range is dependent on the small OAM changing due to the fog density and the use of fractional OAM improves the phase measurement resolution.

The rapid measurement of the CSD was demonstrated with theoretical and experimental results. By using the 2D HOBBIT and the reverse HOBBIT, it is very easy to filter two points of the beam out and make them interfere. The real-time property of the HOBBIT enables us to characterize the partial coherence rapidly. The simulation and experimental results show that the measured CSD can be used to recover the phase information of the light field.

The 2D HOBBIT system shows great potential for real-time dynamics measurement of complex media. In the future, the radial control, OAM and the azimuthal manipulation will be combined to reconstruct the phase distribution of the whole transverse plane which will help us to understand the media better. Since the measured results focus on the transverse plane which are still accumulated results of the channel along the propagation direction, the compressive imaging method might enlighten us to get the longitudinal channel information which is a promising field to discover.

CHAPTER FOUR

SECOND-HARMONIC GENERATION OF ASYMMETRIC BESSEL-GAUSSIAN BEAMS

4.1 Introduction

In the former chapters, the HOBBIT, the reverse HOBBIT, and the 2D HOBBIT systems which are all capable of creating both integer and fractional OAM in real-time have been introduced. The two essential elements of the HOBBIT are the AOD and the log-polar optics. The AOD deflects the beam which can be seen as adding a linear phase to the incident beam, and this linear phase is used to generate OAM or to change the beam scale. The log-polar optics performs a geometric coordinate transformation and wraps an elliptical Gaussian beam into an APV whose beam size is OAM independent. The PV and Bessel beams are a Fourier pair which means the far-field of a PV or APV is a Bessel beam. However, the details of why the APV or asymmetric BG beams carry OAM with a linear one-to-one correspondence as shown in [12] have not been discussed. However, most fractional OAM beams do not show a linear measurement curve between the prepared and the measured charges. The most common method to generate a fractional OAM is using an SPP with fractional order whose azimuthal phase gradient is not integer times of 2π. The fractional-order SPP has a phase step in its phase profile which will generate multiple singularities propagating along the axis. The multiple singularities can be considered as constructive and destructive interference with the propagation. The relationship between the prepared and measured OAM can be described by a winding curve [23]. Other methods

to generate fractional OAM like the transverse shifted SPP [8] or the superposition of different OAM modes such as LG beams or Bessel beams [9, 10] have a very complicated OAM mapping curve. This complexity will impact the nonlinear interaction of OAM beams. In this chapter, the OAM measurement theory will be discussed in detail. The linearity of the HOBBIT generated asymmetric BG beam will be illustrated for the fundamental and nonlinear generated beams.

Nonlinear optical processes not only provide methods to generate new light frequencies but also to manipulate the OAM charges from the fundamental to the nonlinear generated beams. Due to the energy and momentum conservation rule in nature, the OAM-involved nonlinear interaction has been summarized as the OAM conservation law [13, 14]. The OAM-involved nonlinear processes have been widely studied, such as SHG [13, 14, 17, 18, 49, 80], SFG [40], DFG [41], HHG [42, 43], SPDC [44], four-wave mixing [45-47] and vortex-pumped optical parametric oscillator [48]. For each of the nonlinear processes mentioned, integer OAM is used to create the new converted charge. In this chapter, more discussions will focus on the SHG of both integer and fractional OAM. Padgett et al. first demonstrated the SHG of LG beams in [13, 14], and they put forward the OAM conservation law. In [80], Bovino et al. illustrated a non-collinear scheme and used a combination of opposite OAM charges as the pump which proves the global OAM value is zero. In [81], Li et al. confirmed the OAM conservation law by studying the SHG of arbitrary OAM combinations with a non-collinear setup. In 2016, the SHG of fractional OAM generated by a fractional-order SPP was studied by R. Ni [17], and the OAM decomposition theory was used to study the multi-mode interaction. In 2017, Stanislovaitis

et al. used a collinear scheme to study the SHG of fraction OAM [49], and they show that the SHG of a half-integer OAM will generate an integer charge which proves the OAM conservation law at both integer and half-integer charges with SHG. In 2018, Alam et al. generated fractional OAM with shifted SPP and used the OAM decomposition method to analyze the SHG of fractional OAM [18], and they analyzed the global OAM conversion in this process. The fractional-order SPP and the transverse shifted SPP are two methods widely used to generate fractional OAM and are used to study the nonlinear conversion in most cases. However, even the global OAM in the fundamental beam is not strictly linearly mapped which brings lots of difficulties to manipulating the SHG OAM accurately. The results prove the conservation of integer and half-integer OAM beams is limited, and the OAM cannot be arbitrarily controlled. Our motivation is to study the OAM mapping of the prepared and measured OAM charges by the HOBBIT system and to illustrate the behavior of the asymmetric BG beams in the SHG process.

In this chapter, the SHG of the asymmetric BG beams carrying both integer, fractional, and multiple OAM modes will be studied. The OAM SHG theory will be discussed. The key factors impacting the OAM conversion in nonlinear processes will be discussed. The global OAM measurement theory based on a cylindrical lens [23, 24] will be adopted to measure the fundamental and SHG OAM. The measured OAM curves for the fundamental and the SHG fields have a good one-to-one correspondence to the prepared OAM charges by appropriately generating the RF signal driving the AOD. Our results show the first time the mapping curve of fractional OAM was generated through a nonlinear process. The nonlinear conversion efficiency will also be discussed.

4.2 The HOBBIT system and the OAM SHG theory

The HOBBIT system used in this chapter is similar to the system demonstrated in chapter 2 [11]. Both an APV and asymmetric BG beams can be generated using the HOBBIT. The APV is the field right after the log-polar optics, and by simply using a Fourier lens, the APV can be transformed into the asymmetric BG beams. The APV can be described by,

$$\begin{aligned}\vec{U}(r,\theta,z,t) &= \vec{y}S(t)\exp(i2\pi f_c t)A(r,\theta)\exp(-i\ell\theta - ikz) \\ &= \vec{y}\sum_n c_n \exp\left[i\left(2\pi f_n(t)t+\varphi_n\right)\right]\exp(i2\pi f_c t) \\ &\cdot\exp\left(-\frac{(r-r_0)^2}{w_r^2}-\frac{\theta^2}{w_\theta^2}\right)\exp\left(-i\ell_n(t)\theta - ik_{zn}z\right),\end{aligned} \tag{4.1}$$

where $\vec{y}$ represents the vertical polarization, $S(t)=\sum_n c_n \exp\left[i\left(2\pi f_n(t)t+\varphi_n\right)\right]$ is the RF signal driving the AOD, c_n is the scaling factor, $f_n(t)$ is the frequency function that can be programmed to any form to arbitrarily manipulate the generated beam, φ_n is the initial phase for each component, $A(r,\theta)=\exp\left(-\frac{(r-r_0)^2}{w_r^2}-\frac{\theta^2}{w_\theta^2}\right)$ is the amplitude distribution, r_0 is the ring radius of the APV, w_r is the ring half-width, $w_\theta=\beta\pi$ is the azimuthal half-width of the APV, β is the asymmetry, f_c is the incident light frequency, $k_{zn}=2\pi\cos\left(\lambda_{\ell n}\ell_n(t)/2\pi a\right)/\lambda_{\ell n}$ is the longitudinal wave vector, $\lambda_{\ell n}$ is the Doppler-shifted wavelength. $\ell_n(t)=\frac{2\pi a}{V_{at}\eta_t}\left(f_{AOD}-f_n(t)\right)$ is the generated OAM which is closely

related to the AOD driving frequencies, a is one designed parameter of the log-polar optics, V_{at} is the acoustic velocity, η_t is the magnification ratio of the lens system reshaping the Gaussian beam to an elliptical Gaussian beam, f_{AOD} is the central driving frequency.

Since we want to discuss the SHG of the asymmetric BG beams, a Fourier lens must be used with the APV to generate the far-field which is the so-called asymmetric BG beam. The relation between the input elliptical Gaussian beam, the APV, and the asymmetric BG beams is illustrated in Fig. 4.2.1. The far-field equation can be described as follows,

$$\vec{U}_{far} = \vec{y}\sum_n c_n \exp\left[i\left(2\pi f_n(t)t + \varphi_n\right)\right]\exp\left(i2\pi f_c t\right)\exp\left(-\frac{r^2}{w_G^2}\right)\sum_{m=-\infty}^{\infty} B_m J_m\left(\frac{k_{tm}r}{\mu_m}\right)\exp\left(-im\theta\right), \tag{4.2}$$

where $w_G = \lambda_{\ell n}(t)F/(\pi w_r)$ is the Gaussian envelope width, F is the Focal length of the Fourier lens, and the summation in the equation indicates that the far-field of the APV is a superposition of OAM states, $B_m = (-i)^m \exp\left[-w_\theta^2\left(\ell_n(t)-m\right)^2/4\right]$ is the discrete weighting factor giving the OAM spectrum. $J_m\left(\frac{k_{tm}r}{\mu_m}\right)$ is the first-order Bessel function, k_{tm} is the transverse wave number and μ_m is a complex factor [60].

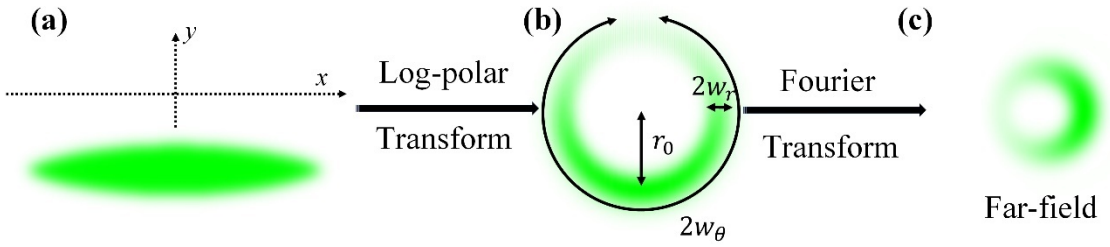

Fig. 4.2.1. The mapping procedure to generate the asymmetric BG beams. (a) The elliptical Gaussian beam. (b) The APV distribution. (c) The asymmetric BG beam [82].

Then the SHG theory to analyze the OAM conversion of the asymmetric BG beams will be discussed. The SHG theory in [13] is applied and in this scenario, the complicated complex amplitude of OAM beams and the SHG process is simplified. Assuming the pump OAM beam has a very simple description as follows,

$$U(\omega) = U\exp(i\ell\theta), \tag{4.3}$$

where U is an amplitude distribution which has a very simple distribution profile.

The OAM conservation law tells the OAM conversion from the fundamental field to the nonlinear generated beam. After the SHG process, the final output can be considered as the square operation of the fundamental beam if the input beam has a simple structure in its amplitude and phase. This process can be described as Eq. (4.4). Through the square operation, the generated field will carry a doubled OAM charge.

$$U(2\omega) \propto \left[U(\omega)\right]^2 = \left[U\exp(i\ell\theta)\right]^2 = U^2\exp(i2\ell\theta). \tag{4.4}$$

However, the beam profile of the fractional OAM is usually very complicated. This includes fractional OAM generated using a fractional-order SPP or the shifted SPP methods. The complexity of the amplitude distribution and the discontinuity in the phase profile make it difficult to explain the process just using Eq. (4.4). The advantage of the

asymmetric BG beams is the asymmetric structure in the complex amplitude which makes the beam modal easier than other fractional OAM beams. As a result, Eq. (4.4) could work as a very good approximation to analyze the SHG of the asymmetric BG beams.

Now the situation that the input fundamental beam is a superposition of multiple OAM states will be discussed. For simplicity, two modes are included in the incident beam. Substitute this beam into Eq. (4.4) , the result can be described as Eq. (4.5) mathematically,

$$\begin{aligned} U(2\omega) &\propto \left[U(\omega)\right]^2 = \left[U_1 \exp(i\ell_1\theta) + U_2 \exp(i\ell_2\theta)\right]^2 \\ &= U_1^{\,2} \exp(i2\ell_1\theta) + U_2^{\,2} \exp(i2\ell_2\theta) + 2U_1U_2 \exp\left[i(\ell_1+\ell_2)\theta\right]. \end{aligned} \tag{4.5}$$

The above equation describes the ideal case for multiple OAM interaction in a nonlinear process. However, the real interaction is quite complicated. Since fractional OAM can be seen as a combination of the whole OAM basis with different scaling factors, the multiple OAM interaction is not just as simple as in Eq. (4.5). The real interaction is very difficult to be simulated. Whether the interaction happens during the SHG conversion needs to be considered. Many references studied the multiple OAM interaction in SHG or other process like the four-wave mixing [15, 16, 83]. Because in most cases the size of an OAM beam is OAM-dependent, the interaction between two modes requires overlapping during the nonlinear processes which lead to the actual interaction does not follow the mathematical description as Eq. (4.5). This is also the reason why the fractional OAM nonlinear conversion does not follow a linear one-to-one correspondence. The modified equation to describe the multiple modes interaction can be described as follows,

$$\begin{aligned} U(2\omega) &\propto \left[U(\omega)\right]^2 = \left[U_1 \exp(i\ell_1\theta) + U_2 \exp(i\ell_2\theta)\right]^2 \\ &= C_1U_1^{\,2} \exp(i2\ell_1\theta) + C_2U_2^{\,2} \exp(i2\ell_2\theta) + C_{12}U_1U_2 \exp\left[i(\ell_1+\ell_2)\theta\right], \end{aligned} \tag{4.6}$$

where C_1, C_2 and C_{12} are the complex coefficients of each mode after the nonlinear conversion which are determined by three factors during the nonlinear conversion. The three factors are the power density of each mode, phase matching condition for different OAM, and the mode overlapping integration along the nonlinear medium [16]. The power density of the fundamental beam will directly affect the nonlinear conversion efficiency. The phase-matching condition is related to the k vector mismatch which is determined by the spiraling k vector of the OAM beams. Since the skew angle of the OAM is described as $\frac{\ell}{kr}$, the phase matching is determined by both the OAM charge and the beam size. Finally, for different OAM, the propagation situations are different and in the nonlinear medium, only overlapped parts of different modes interact which leads to the fundamental beam is not converted efficiently. All these factors result in Eq. (4.6) and for the fractional OAM nonlinear conversion case, the generated OAM charge is not exactly doubled and has a large shift from the supposed charge value.

The far-field of the APV, the asymmetric BG beams, is a combination of a large set of OAM modes with different scaling factors which is described by its global OAM, ℓ. Here the far-field Eq. (4.2) is simplified as follows,

$$U_{FF}^{(\ell)}(\omega) = \sum_{m=-\infty}^{+\infty} C_m J_m\left(\frac{k_{tm} r}{\mu_m}\right) \exp(-im\theta), \tag{4.7}$$

where m denotes each component in the spectrum of ℓ, $C_m = c_m A_m GB_m$ is the complex coefficient for each m, c_m is the weighting factor, A_m is the asymmetric amplitude, GB_m is the Gaussian envelope.

Substituting Eq. (4.7) into Eq. (4.6), an approximation result of the final SHG field can be described as follows,

$$U_{FF}^{(2\ell)}(2\omega) = \sum_{m=-\infty}^{+\infty} C_{pq} J_p J_q \exp\left[-i(p+q)\theta\right], \tag{4.8}$$

where p and q are any two interacting OAM charges in the summation of m, $C_{pq} = c_{pq}\gamma_{pq} B(\Delta k_{pq}) A_{pq} GB_{pq}$ is the complex scaling factor of the generated OAM component due to the interaction of p and q, γ_{pq} describes the overlapping coefficient, $B(\Delta k_{pq})$ is the phase-matching coefficient, A_{pq} is the asymmetric amplitude, and GB_{pq} is the Gaussian envelope, $J_p J_q$ is the Bessel term. In this equation, the power density, phase-matching condition, and mode overlapping are all considered as contributions to the final field. The nonlinear process will change the original spectrum distribution and generate a relatively random distribution of the final spectrum which will cause the OAM charge to shift away from the doubled value.

4.3 Global OAM measurement method

In this section, the global OAM measurement method using cylindrical lens will be introduced and the simulation results with different OAM carrying beams and the SHG beam will be shown.

The cylindrical lens method described in [23, 24] is used to measure the global OAM charge of a complex field. When a beam carrying OAM propagates through a cylindrical lens, the far-field in the Fourier plane will have a specific intensity distribution.

By capturing the intensity distribution using a CCD camera, the global or average OAM charge can be calculated by the following equation,

$$\ell_{mean} = \frac{J_z}{W} = \frac{\mathrm{Im}\int_{-\infty}^{\infty}\int_{-\infty}^{\infty} U(x,y,z)_\ell^* \left(x\frac{\partial}{\partial y} - y\frac{\partial}{\partial x} \right) U(x,y,z)_\ell \, dxdy}{\int_{-\infty}^{\infty}\int_{-\infty}^{\infty} U(x,y,z)_\ell^* U(x,y,z)_\ell \, dxdy} \tag{4.9}$$

where $U(x,y,z)_\ell$ is the complex amplitude of the incident beam and $U(x,y,z)_\ell^*$ is its complex conjugate, $\left(x\frac{\partial}{\partial y} - y\frac{\partial}{\partial x} \right)$ is the differential operator in Cartesian coordinate.

The cylindrical lens is used to do 1D Fourier transform to the input beams and using the cylindrical lens method, Eq. (4.9) can be related to the measured intensity by rotating the cylindrical lens in horizontal and vertical directions,

$$\ell_{mean} = \frac{2\pi}{f\lambda}\left(\frac{\int\int_{-\infty}^{\infty} I(x',y)_\ell \, x'ydx'dy}{\int\int_{-\infty}^{\infty} I(x',y)_\ell \, dx'dy} - \frac{\int\int_{-\infty}^{\infty} I(x,y')_\ell \, xy'dxdy'}{\int\int_{-\infty}^{\infty} I(x,y')_\ell \, dxdy'} \right), \tag{4.10}$$

here $I(x,y)_\ell$ is the intensity distribution at the focal plane of the cylindrical lens and f is the focal length of the cylindrical lens.

Next, the simulation method will be used to show the advantage of the asymmetric BG beams, compared to other OAM modals carrying fractional OAM. 3 different β values for the asymmetric BG beams are chosen to compare with a plane wave and the hypergeometric Gaussian modes. The fractional OAM range is chosen from -1.5 to +1.5 with a step of 0.1. The simulation results are shown in Fig. 4.3.1(a). The plane wave carrying a fractional OAM will show a global OAM which is close to the nearest integer

value as shown in [5]. When a Gaussian beam propagates through an SPP, the generated beam modal can be considered as the hypergeometric Gaussian (HyGG) beam. As shown in [6, 23], the HyGG beam will show a winding OAM mapping curve. The three β values are 0.5, 0.7, and 1. The mapping curves for the three β in Fig. 4.3.1(a) are very linear but with slightly different amplitudes in their undulations. The differences in these mapping curves indicate that the asymmetric BG beams carry fractional OAM with linear one-to-one correspondence. This is due to the asymmetry avoids the branch-cut at the phase discontinuity. As a result, the interference does not happen along with the propagation. However, in the cases with a plane wave and HyGG beam, the phase discontinuity develops multiple singularities which will contribute to the global OAM measurement. The multiple singularities shift the global OAM value away from the programmed charge which makes the mapping curve nonlinear. Our simulation results show the advantage of the asymmetric BG beams by exploiting the asymmetric structure which decreases the evolution of the phase steps in the beam profile. In Fig. 4.3.1(a), the three intensity distributions at different β are also provided.

Since the nonlinear conversion of the fractional OAM is what we are interested in, the simulation of the OAM mapping curve in SHG with the asymmetric BG beams is shown in Fig. 4.3.1(b). According to Eq. (4.6) and Eq. (4.8), it will be very difficult to get the coefficients for each OAM component. Here Eq. (4.4) is used to estimate the global

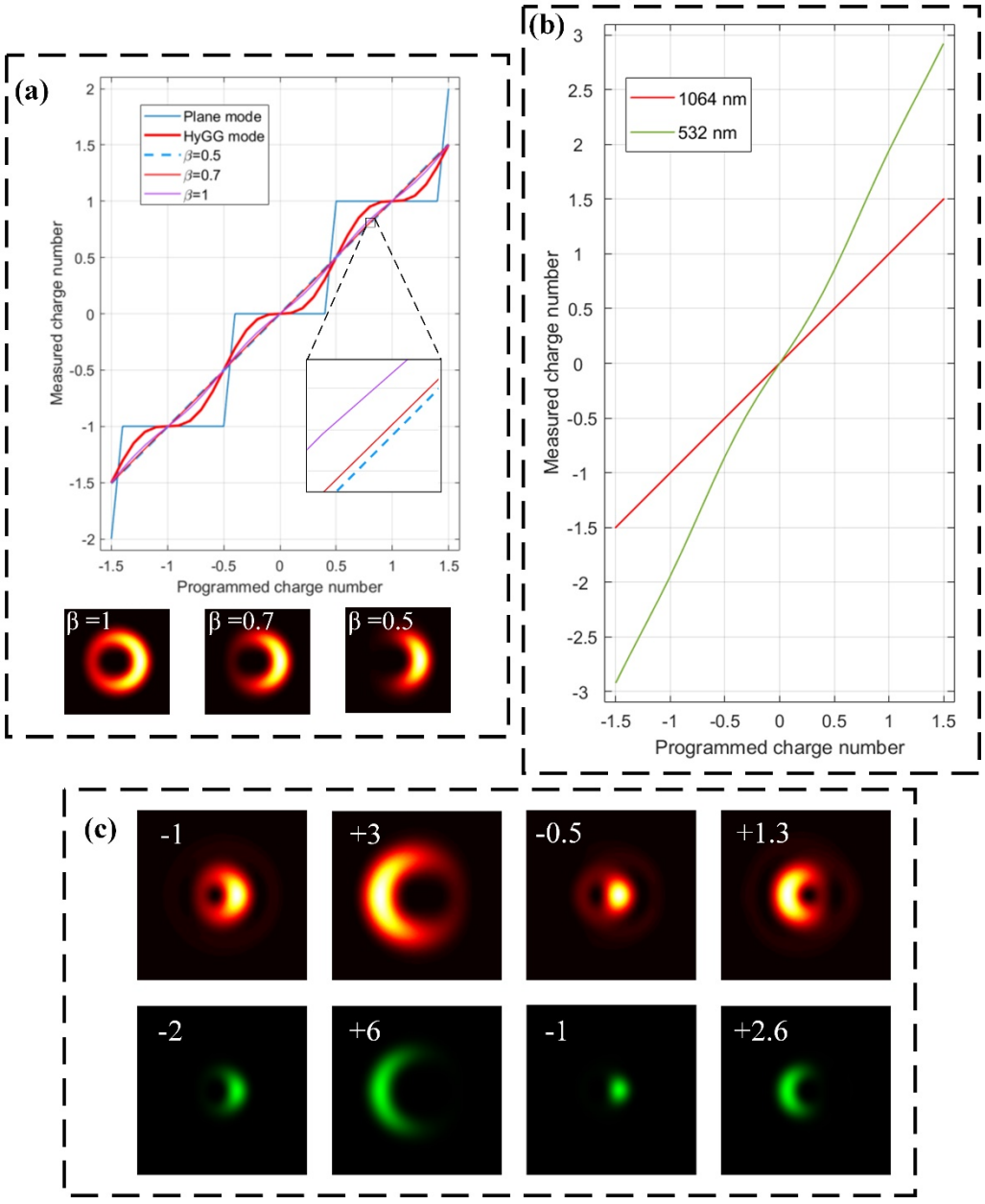

Fig. 4.3.1. Simulation with the asymmetric BG beams. (a) Comparison of the fractional OAM mapping curves among different beam models. (b) Simulated OAM mapping curve for the asymmetric BG beams in SHG. (c) Simulated intensity distributions for fundamental and SHG asymmetric BG beams [82].

OAM values in the SHG field. If our assumption follows the OAM conservation law, the measured global OAM for the input with a range from -1.5 to +1.5 should be from -3 to +3 with a step of 0.2. The asymmetric BG beams are generated in simulation first, then the beams are substituted into Eq. (4.4), and with the output beams, the cylindrical lens method is used to measure the global OAM. From the results, we can see the green curve is not strictly linear but with slight winding. This is due to the basic nature of fractional OAM which is the superposition of integer OAMs. Also, the real process should be worse than this since the interaction is more complicated. In the simulation, the maximum shift happens at charge 0.5 with a shift of about 0.15. But the momentum should still be conserved in the nonlinear process considering the overlapping integration. Figure 4.3.1(c) gives the simulated fundamental and SHG fields by using Eq. (4.4). The labeled OAM charges on each figure are the programmed and the conserved values, ignoring the shift observed in Fig. 4.3.1(b). The SHG field has more asymmetry compared with the fundamental beam which is reasonable because the nonlinear processes are power density related. The simulation results show the advantage of the asymmetric BG beams in the nonlinear process not only due to the better OAM mapping curve for fractional OAM, but also the consistency of the intensity distributions of the fundamental and SHG fields. Considering most fractional OAM beams are not stable when propagating along the axis, our results show similar intensity distributions to the near-field which proves the asymmetric BG beams can retain their shape and OAM charge with propagation.

4.4 Experimental results

A 1064 nm HOBBIT system is used to generate the asymmetric BG beams. The experimental setup can be seen in Fig. 4.4.1. A vertical polarized 1064 nm laser source (Nuphoton 1064 nm Dual Amplifier Assembly) is incident at the AOD. This vertical polarization is required by the AOD and the Magnesium doped Periodically Poled Lithium Niobate (MgO: PPLN) nonlinear crystal for considering diffraction and nonlinear efficiency. The AOD (Gooch & Housego Model #3080-197) adds a horizontal linear phase to the input beam as shown in the former chapters and is controlled with RF signals. A cylindrical lens ($f = 40mm$) and a spherical lens ($f = 200mm$) construct a lens system to reshape the input Gaussian beam into an elliptical Gaussian beam. The log-polar optics do the geometric coordinate transformation and wrap the elliptical Gaussian beam into the APV. A Fourier lens ($f = 200mm$) is used to get the asymmetric BG beams. A 20 mm MgO: PPLN crystal with a period of 6.93 μm (Covesion MSHG1064-1.0-20) is placed at the Fourier plane. By using quasi-phase-matching, the 1064 nm fundamental beam is converted to 532 nm. An imaging lens ($f = 75mm$) is placed after the MgO: PPLN to image the center of the crystal to a CCD camera (Spiricon SP300). Two dichroic mirrors are used to filter the 1064 nm fundamental laser out. A pick-off optic is used then to reflect about 10% of the generated beam to the camera. A cylindrical lens ($f = 100mm$) before the camera is used for the OAM measurement.

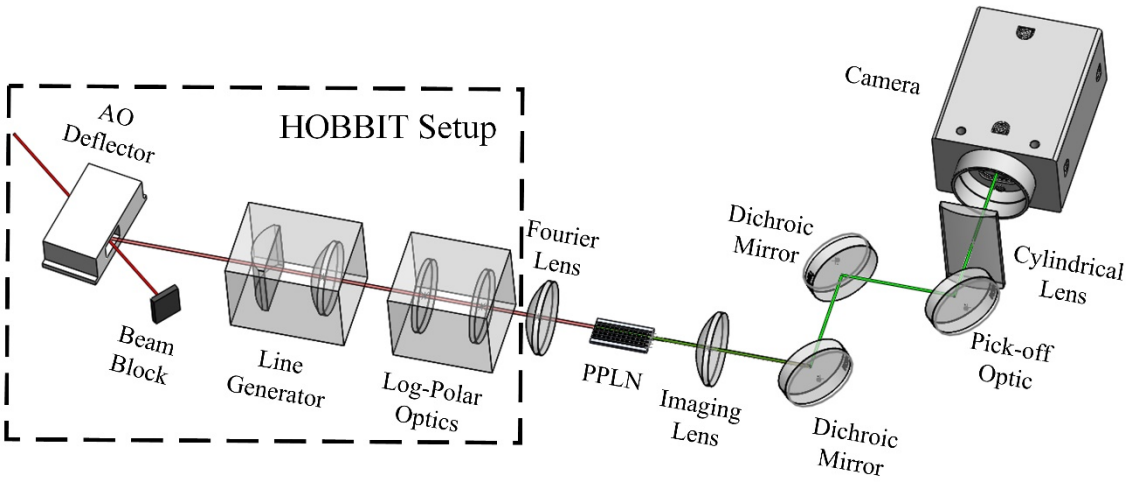

Fig. 4.4.1. Experimental setup for the SHG of the asymmetric BG beams [82].

The experimental results are shown in Fig. 4.4.2. The intensity distributions of the 1064 nm fundamental beams are shown in Fig. 4.4.2(a) and Fig. 4.4.2(c). Both integer and fractional OAMs are included. We can see all the intensity profiles of the fundamental beams have a similar distribution which fits well with the property of retaining the shape. Integer OAM charges from -3 to +3, fractional OAM from -2.5 to +2.5 with a step of 1, and two extra fractional OAM -0.26 and +0.6 are generated by designing relative RF signals. Figure 4.4.2(b) and Figure 4.4.2(d) are the SHG beams corresponding to the fundamental beams. The labeled OAM charges are based on the OAM conservation law. The results shown in the figure have a good agreement with the simulation results in Fig. 4.3.1(c) which proves the good approximation of our theoretical model.

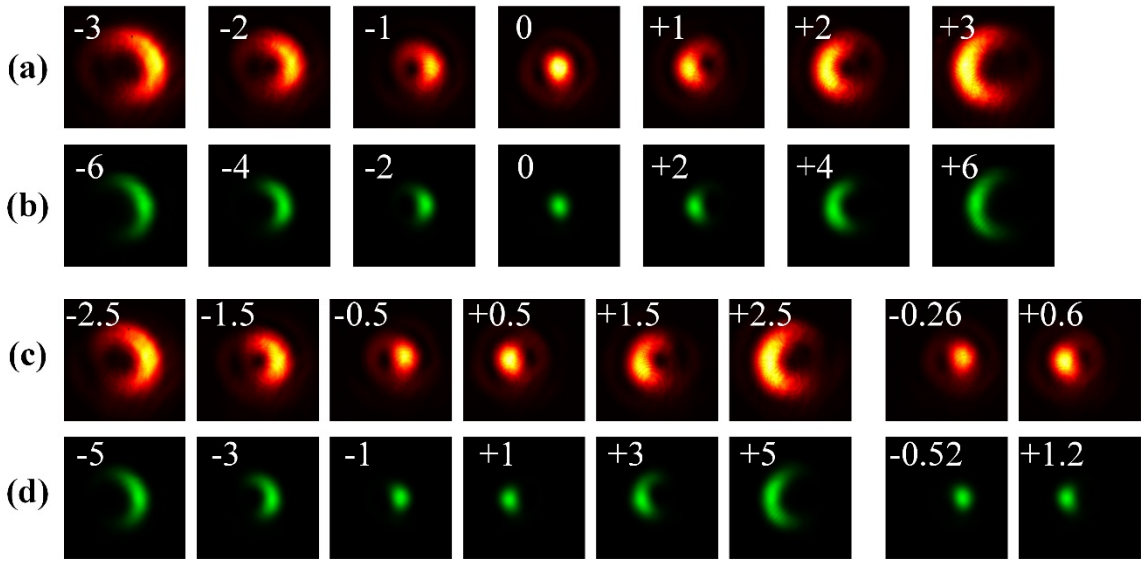

Fig. 4.4.2. Experimental intensity distributions of the fundamental and SHG beams. Row (a) and (c) denote the fundamental 1064 nm beams. Row (b) and (d) are the relative SHG beams. The labeled SHG OAM charges are based on the OAM conservation law [82].

The OAM mapping curve for measuring fractional OAM in a range with small steps is shown in Fig. 4.4.3. Both the simulation and experimental results are included. The error bars in the figure are based on the standard deviation by measuring 9 different frames of the same OAM charge. From the results, for the 1064 nm fundamental beam, the OAM mapping curve shows very good linearity between the programmed and the measured OAM, and for the 532 nm SHG fields, there are more undulations in the experimental results than in the simulation which is as predicted. However, the OAM mapping curve for the SHG field still shows a very good one-to-one correspondence for the fractional OAM which is the first time to show a relative result. The results prove that the asymmetric BG beams can provide fractional OAM in fundamental and nonlinear generated fields. The results also show that by controlling the complex amplitude of the light field, it is possible

to tailor and generate arbitrary OAM charges and the beam can have a better propagation property.

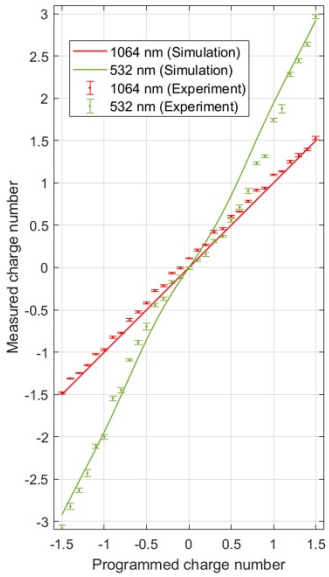

Fig. 4.4.3. The measured OAM mapping curve for the fundamental and SHG beams [82].

The crescent intensity distribution rotates 90 degrees from the APV to the asymmetric BG beam which indicates during the propagation from near-field to far-field the rotation may have an impact on the mode overlapping in the nonlinear crystal. A simulation is done to study the propagation property of the beam using different Fourier lenses first. The results are shown in Fig. 4.4.4(a). Two focal lengths are chosen, 50 mm and 200 mm and the OAM charge is +3. The length of the MgO: PPLN is 20 mm and the relative positions from -10 mm to +10 mm are labeled in the figure. We can observe that with different Fourier lenses, the beam propagation is very different. With the 50 mm lens, the beam rotates almost 180 degrees as it propagates through the crystal. Respectively, with the 200 mm lens, nearly no rotation can be observed. Since the nonlinear conversion of the OAM beams is related to the mode overlapping integral, the generated field can be rather

different. The corresponding experimental results with the two Fourier lenses can be seen in Fig. 4.4.4(b) which is as predicted. Using a shorter focal length, the $\pm\ell$ overlap and interact which will generate OAM 0 component. As a result, there is a bright spot in the center of the intensity. For the 200 mm lens, the $\pm\ell$ overlap is less and no bright spot is observed in the beam profile. The labeled OAM charges in the figure are based on different schemes.

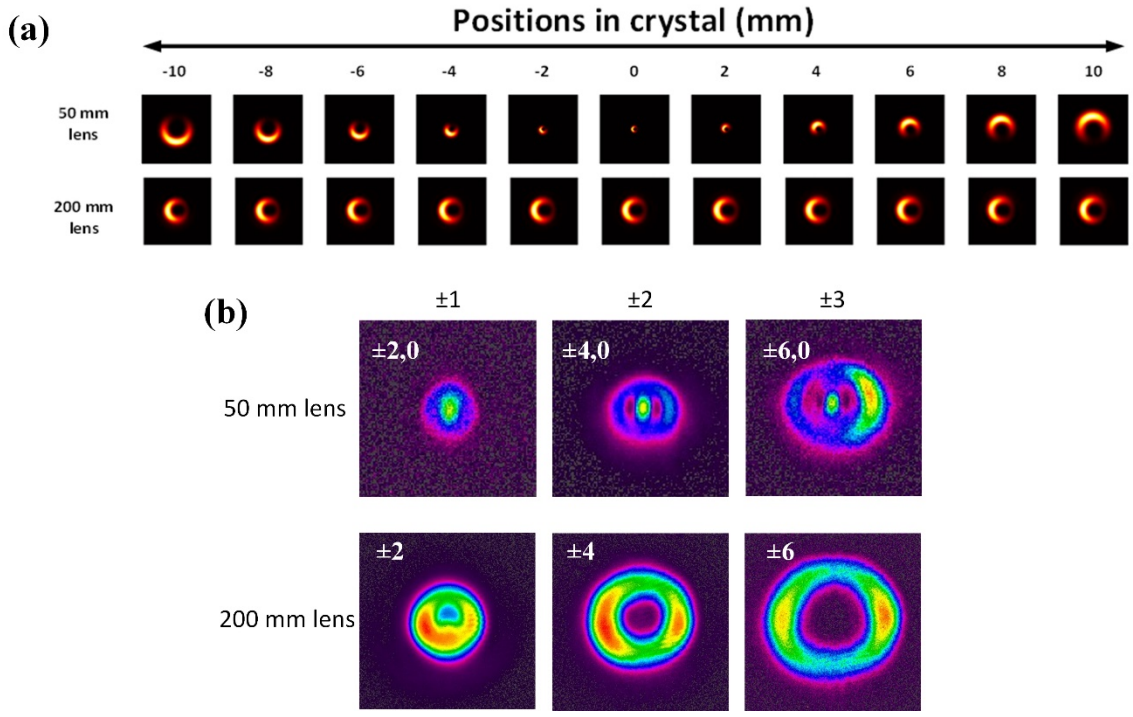

Fig. 4.4.4. (a) Simulation results of the asymmetric BG beams in the MgO: PPLN for using different focal lenses. (b) Experimental results of the generated 532 nm beams for using 50 mm and 200 mm Fourier lenses [84].

The single-pass conversion efficiency of the asymmetric BG beams using the 200 mm Fourier lens is measured to show the differences between different OAM. OAM charges 0 and $\pm\ell$ $(\pm1, \pm2, \pm3)$ are chosen. The $\pm\ell$ intensity distributions are shown in

Fig. 4.4.4(b). Note here since a CW laser source is used and the Doppler frequency shifts for different OAM, the typical interference pattern cannot be observed due to the CCD camera is much slower than the electric field change and only provides an averaging result based on the exposure time. Besides, the AOD's diffraction efficiency varies at different OAM charges. Therefore, different coherent OAM modes may have varying maximum power generated from the HOBBIT which will affect the conversion efficiency. OAM 0 has a maximum pump power of 4960 mW and the generated SHG beam has a power of 149 mW at the phase-matching temperature of 36.7 ℃ which gives an efficiency of 3%. For OAM charge ± 1, the maximum input and output power are 3170 mW and 41 mW and the conversion efficiency is 1.29%. The difference in the phase-matching conditions for OAM 0 and ± 1 is not only because of the power but also because of the mentioned skew angle difference for different OAM. The maximum efficiency for the current system is 3%, 1.29%, 0.72%, and 0.4% for SHG OAM 0, ± 2, ± 4, ± 6. The impact of the Doppler frequency shift and the low efficiency can be further improved by using a pulse source with high peak power.

4.5 Conclusion

In this chapter, the SHG of the asymmetric BG beams carrying integer, fractional and coherent OAM modes has been demonstrated. The beam modal is generated by a 1064 nm HOBBIT system. The AOD in the system is driven by RF signals and will deflect the beam in multiple directions. The linear phase gradient on the beam profile will be mapped to an azimuthal phase gradient by the log-polar optics. After the log-polar optics, the generated near-field, the APV, has an OAM-independent beam size. Using a Fourier lens,

the far-field, the asymmetric BG beam, can be generated. For a single OAM charge generated by the HOBBIT system, the far-field carries a summation of integer OAM charges which are described by a series of Bessel modes. This superposition property indicates the complexity of the modes if we want to do manipulation on this beam model. However, despite the complicated OAM spectrum of the asymmetric BG beams, a very simple SHG theory was used to analyze the OAM nonlinear conversion. When the complex amplitude of an OAM beam has a relatively simple distribution, the SHG field is proportional to the square of the fundamental field, generating a beam carrying a doubled OAM charge which is called the OAM conservation law. For multiple modes interaction, the situation will be more complicated. For a regular OAM beam whose beam size is OAM-dependent, the multi-mode interaction will be affected by the overlapping integration along the nonlinear medium. As a result, the coefficients for each generated OAM component do not follow the mathematical calculation. The factors impacting the multi-mode interaction are summarized in this chapter as follows, the power density, the phase-matching condition, and the mode overlapping. The power density is directly affecting the mode conversion since the nonlinear processes are power density related. The phase-matching condition matters because for OAM-dependent beam size, the skew angle of the k vector is determined by the OAM charge and beam size. The mode overlapping is the most significant factor which will decide the final SHG OAM spectrum.

Fractional OAM can be decomposed into a summation of an integer OAM basis which is also suitable for the asymmetric BG beams since the far-field equation tells this result. Despite the complexity of the OAM spectrum, the cylindrical lens method was

exploited to simulate the measurement of the global OAM of the asymmetric BG beams in the fundamental field and other OAM modes like the plane wave and HyGG beam carrying OAM. The results show that the asymmetric BG beams can carry OAM with a linear one-to-one correspondence. This is due to the asymmetric structure in the complex amplitude and this feature eliminates the branch-cut phase discontinuity and there will be no interference and multiple singularities generation along with the propagation. Compared to other fractional OAM beams, the asymmetric BG beams have a linear OAM mapping and can retain their shape propagating from near-field to far-field. Our asymmetric BG beams have a relatively simple complex amplitude and the SHG theory mentioned above is used to get the SHG field. Then the cylindrical lens method is used to measure the global OAM in the SHG field. The results show a very good one-to-one correspondence and only show slight undulation in the curve which is due to the OAM spectrum in the beam. However, the simulation is ideal and the real interaction will give more undulations which are observed later in the experimentally measured OAM mapping curve. Despite the undulations in the mapping curve, this is the first time to show a one-to-one correspondence of the fractional OAM in SHG. The simulated and experimental intensity distributions of the fundamental and SHG field show great agreement. Then the mode overlapping issue was discussed by using different Fourier lenses to get the fundamental asymmetric BG beams. Two focal lengths were chosen, and the propagation situations of both beams in the nonlinear crystal were executed to show the difference. With a shorter focal length, the beam profile of an OAM +3 in the crystal almost rotates 180 degrees, while for the longer focal length the rotation of the beam profile can be hardly observed. The simulation results

indicate the difference in the SHG field for an input OAM of $\pm\ell$. This difference was observed in the experimental results. For the shorter focal length, there is an OAM 0 component, and a bright spot can be seen in the center of the field. However, for the longer focal length, the OAM $\pm\ell$ was converted to $\pm 2\ell$ through the SHG. Finally, the single-pass nonlinear conversion efficiencies of 0, ± 2, ± 4, ± 6 were measured and a 3% maximum efficiency is obtained for OAM 0. This efficiency was measured with the current setup and can be further improved by changing the parameter in the scheme or by using a pulsed laser source with higher peak energy like the 2D HOBBIT system.

In this chapter, the asymmetric BG beams are utilized as the OAM beam modal to study the SHG of OAM beams. Due to the asymmetric property of the beam modal, the advantages of using the asymmetric BG beams are discussed. Our results show the guidance of using OAM beams to do nonlinear conversion with an OAM-dependent size. The factors impacting the interaction are discussed. In the next chapter, the nonlinear conversion of the APV will be studied. The APV has an OAM-independent beam size, and the nonlinear interaction will only be affected by the OAM. Our nonlinear study on the asymmetric BG beams and the APV will help us understand the basic nature of the fractional OAM and will be promising for applications trying to expand the high-dimensionality of structured light.

CHAPTER FIVE

SECOND-HARMONIC GENERATION OF ASYMMETRIC PERFECT VORTEX

5.1 Introduction

The nonlinear interaction involving OAM provides a way to manipulate both OAM and the wavelength simultaneously, which is very important since it is difficult to generate high charge OAM at some specific wavelength band using regular methods such as the deep UV OAM beams. Most SLMs are unsuitable for deep UV beams and the lithography method may not have enough resolution for shorter wavelengths. However, most OAM-involved nonlinear processes are very complicated, and a lot of factors need to be considered in the conversion process. As demonstrated in the former chapter, power density, phase-matching condition, and mode overlapping are the three parameters that determine the output results of the nonlinear conversion. The power density is a well-known parameter affecting any nonlinear process since the high-order nonlinear coefficient is related to the strength of the light field. The phase-matching condition is ignored by most references since the phase gradient of the OAM azimuthal phase is relatively small, but it is essential when considering multiple OAM interactions. Mode overlapping is a phenomenon that occurs when the OAM modes in the nonlinear process have an OAM-dependent size. For example, the LG modes and Bessel-Gauss modes whose beam sizes increase as the OAM charge increases undergo a very complicated nonlinear integration along with the nonlinear media. All three of these factors are interdependent, which makes the nonlinear interaction hard to predict. In [15, 16], the theoretical and experimental

results in SHG and four-wave mixing show the complexity of the multiple OAM interaction and use the mode overlapping integral to solve the problem. Their results show a very good fitting between the theory and experiment. In [17, 18], the SHG of fractional OAM using fractional-order SPP and transverse shifted SPP are studied, and the multiple OAM interaction based on OAM spectrum decomposition is used to calculate the mode overlapping integral. The fractional OAM can be considered a combination of infinite integer OAM, so the nonlinear conversion of fractional OAM can be treated as a multi-mode interaction. However, the nonlinear studies involving fractional OAM are not direct and the analysis is very complicated. Considering the regular fractional OAM such that the HyGG modes [23] do not have a linear one-to-one correspondence curve, the mapping curve for the nonlinear generated modes is not linear. For most studies, to manipulate the OAM, a linear mapping curve is essential.

In the former chapter, the SHG of the asymmetric BG beams has been introduced. The SHG theory for a fundamental field with simple distribution was demonstrated and the SHG field is proportional to the square of the fundamental beam. Thus, for a single integer OAM input, the SHG field will carry a doubled OAM charge. However, this usually does not work for fractional OAM due to the complicated structure of both the amplitude and the phase. The asymmetric BG beams carry an OAM with a linear one-to-one correspondence which is confirmed by the cylindrical lens method [23, 24] which can measure the global OAM of a field. Compared to the fractional OAM generated with fractional-step SPP or the shifted SPP, the asymmetric BG beams maintain shape during propagation due to the asymmetric property. This asymmetry also causes the SHG field to

carry an OAM with a very good one-to-one correspondence, which is the first time a relationship such as this has been shown. There is a slight undulation in the mapping curve, which is due to the asymmetric BG beams being a superposition of a set of Bessel beams and requires the mode overlapping to be considered. Our SHG study on the asymmetric BG beams shows the considerations when studying nonlinear conversion using OAM-dependent beam sizes, and the asymmetric property provides a method to manipulate the converted OAM in nonlinear processes.

In this chapter, the SHG of the APV will be studied. Compared to the asymmetric BG beams, the APV has an OAM-independent beam size. Due to this feature, the interaction only affected by the OAM can be explored. The theoretical analysis of why the beam generated by the HOBBIT system can carry OAM with a linear mapping curve will be given based on the electromagnetic theory. Our results will demonstrate that the global OAM is impacted by both amplitude and phase distributions. The coupled wave theory will be exploited to study the SHG process. The simple phase structure of the APV will also be beneficial to the SHG interaction. The SHG study with the APV shows that the SHG field carries OAM with a linear one-to-one correspondence, which is a further improvement on the results of the asymmetric BG beams. The reverse HOBBIT system is used to get the fractional OAM mapping curve. Due to the Doppler frequency effect embedded in the CW HOBBIT system, the reverse HOBBIT can be used to study the multiple OAM interaction theory with the APV. The measured results show that the SHG theory using APV can be predicted and manipulated with amplitude and phase. The 2D pulsed HOBBIT system is also used to generate deep UV beams carrying higher-order OAM. The results coincide

with the APV nonlinear interaction theory and are promising in applications such as quantum information technology.

5.2 Theoretical analysis of the global OAM of the APV

It is well-known that OAM beams have features such as a donut-shaped intensity distribution and a spiraling wavefront. The donut shape is due to the transverse phase distribution which causes a phase singularity in the center of the field. As a result, OAM beams are considered phase structured light in most cases. In this section, the significance of the amplitude distribution of the light field based on the electromagnetic analysis of the global OAM will be shown. For simplicity, the APV complex amplitude is expressed as follows,

$$U(r,\theta)=\exp\left(-\frac{(r-r_0)^2}{w_r^2}-\frac{\theta^2}{w_\theta^2}\right)\exp(-i\ell\theta), \tag{5.1}$$

where r_0 is the ring radius, w_r is the radial Gaussian $1/e^2$ width, $w_\theta=\beta\pi$ describes the asymmetry of the APV, and β is the so-called asymmetry factor.

In [7], Padgett discusses the intrinsic and extrinsic properties of the OAM in a light field, and demonstrates the linear momentum density of a light beam that can be calculated with the electromagnetic theory and is described as follows,

$$\vec{p}=\varepsilon_0\left\langle\vec{E}\times\vec{B}\right\rangle=i\omega\frac{\varepsilon_0}{2}\left(u^*\nabla u-u\nabla u^*\right)+\hat{z}\omega k\varepsilon_0|u|^2+\hat{\phi}\omega\sigma\frac{\varepsilon_0}{2}\frac{\partial|u|^2}{\partial r}, \tag{5.2}$$

where ω is the angular frequency of the light, u is the complex amplitude of the light field, ε_0 is the vacuum permittivity, $\hat{\phi}$ and $\hat{z}$ are unit vectors, k is the wave vector, σ

describes the polarization state, and (r,ϕ,z) are the polar coordinates. The first term on the right side is related to the phase gradient which is used to describe OAM, the second term is the linear momentum of the electromagnetic wave in the propagation direction, and the third term is linked to the spin angular momentum (SAM) which is independent of azimuthal phase.

Assuming the light field is linearly polarized, $\sigma = 0$ and the total angular momentum of the field is described as Eq. (5.3). By substituting an unknown complex amplitude into Eq. (5.3), the global OAM can be calculated.

$$J_z = \varepsilon_0 \left(\vec{r} \times \left\langle \vec{E} \times \vec{B} \right\rangle \right)_z = \vec{r} \times i\omega \frac{\varepsilon_0}{2} \left(u^* \nabla u - u \nabla u^* \right). \tag{5.3}$$

Illuminating an SPP with a Gaussian beam will generate fractional OAM which has a nonlinear OAM mapping curve. When substituting this fractional OAM beam into Eq. (5.3), the generated beam has an abrupt phase jump on its transverse plane and, with propagation self-interference of the beam, a smoothing procedure occurs. The calculated global OAM based on Eq. (5.3) will be the same as the one in [23]. However, if the APV is considered, due to the asymmetric distribution, the complex amplitude is continuous in the transverse plane and does not contain any discontinuity because of the amplitude and phase. Then substituting Eq. (5.1) into Eq. (5.3), the calculated result is as follows,

$$J_z = \varepsilon_0 \ell \omega |u|^2 . \tag{5.4}$$

Equation (5.4) is a typical explanation of the OAM carried by the LG beams which can only carry integer OAM [7, 85]. The calculated result with the APV has the same expression, which demonstrates that the APV generated by the HOBBIT system with an

asymmetric structure can carry a global OAM that corresponds to the programmed value. The results have been shown in the former chapters using the asymmetric BG beams and the cylindrical lens method. This can be explained by showing that the free-space propagation is a linear process that will not change the global OAM value. Here the APV structure and the measured OAM mapping curve are shown in Fig. 5.2.1.

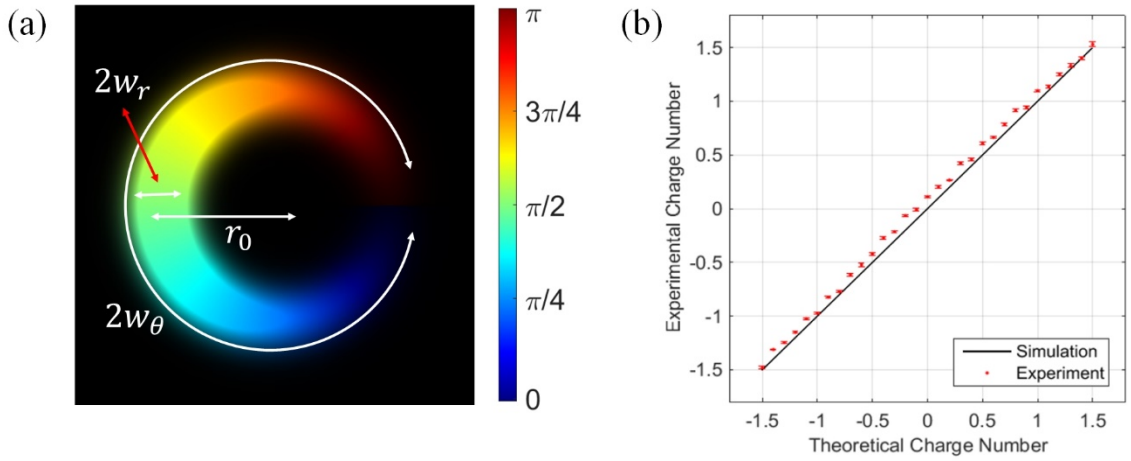

Fig. 5.2.1. (a) The intensity and phase distributions of the APV carrying OAM 0.5. (b) The OAM mapping curve of the APV using the cylindrical lens method [86].

5.3 SHG of the APV: theory and experiment

In section 5.2, that the APV carries a global OAM with a linear one-to-one correspondence is theoretically proved. In this section, the coupled wave equation for the SHG process will be used to for the nonlinear conversion of the APV. Single OAM and multiple OAM interaction will be analyzed. The light source of a CW HOBBIT system and the measurement using the reverse HOBBIT system will be exploited to measure the converted OAM.

The coupled wave equation for the SHG is as follows [87],

$$\frac{dA_1}{dz} = \frac{2i\omega_1^2 d_{eff}}{k_1 c^2} A_2 A_1^* \exp(-i\Delta kz), \tag{5.5}$$

$$\frac{dA_2}{dz} = \frac{i\omega_2^2 d_{eff}}{k_2 c^2} A_1^2 \exp(i\Delta kz), \tag{5.6}$$

where A_1 and A_2 denote the complex amplitudes of the fundamental and the SHG fields, ω_1 and ω_2 are the light angular frequencies, k_1 and k_2 are the wave numbers, d_{eff} is the effective nonlinear coefficient, c is the speed of light, and $\Delta k = 2k_1 - k_2$ represents the wave vector mismatch in the nonlinear conversion.

Assuming the incident pump A_1 has a simple distribution that can be considered as a constant, Eq. (5.6) can be integrated directly to get the SHG field by taking the undepleted-pump approximation [87]. The calculated complex amplitude and the intensity distribution of the SHG field can be expressed as follows,

$$A_2(L) = \frac{i\omega_2^2 d_{eff}}{k_2 c^2} A_1^2 \left(\frac{\exp(i\Delta kL) - 1}{i\Delta k} \right), \tag{5.7}$$

$$I_2 = 2n_2 \varepsilon_0 c \left| A_2 \right|^2 = \frac{n_2 \omega_2^2 d_{eff}^2}{2n_1^2 \varepsilon_0 c^3} I_1^2 L^2 \mathrm{sinc}^2(\Delta kL/2), \tag{5.8}$$

where L is the length of the nonlinear medium, n_1 and n_2 correspond to the refractive indices of the fundamental and SHG field in the medium, ε_0 is the permittivity of free space, and I_1 is the intensity distribution of the fundamental field. Considering the simple amplitude and phase structures of the APV, Eq. (5.1) can be directly substituted into Eq. (5.7) to get the SHG field which carries an OAM of 2ℓ. This also indicates that the OAM mapping curve of the SHG field will have a linear one-to-one correspondence.

The benefit of using the APV is that the intensity distribution of the APV is independent of the OAM carried by the beam. This property allows us to isolate and explore only the impact of the OAM in the nonlinear conversion. Furthermore, since the beam size of the APV is OAM-independent, the mode overlapping issue observed with LG beams and the asymmetric BG beams will not be an issue. Considering the APV is generated by the HOBBIT system, the power ratio among different OAM modes can be arbitrarily controlled indicating that the power density factor is under control. The third factor in the nonlinear processes is phase-matching. Since the Poynting vector of the OAM beams spirals along the propagation axis, the angle of the Poynting vector and the axis can be described by Eq. (5.9). As a result, this angle is determined by the OAM charge and the beam size together. By changing the OAM charge and the beam size, the nonlinear interaction can be controlled.

$$\alpha = \frac{\ell}{kr}. \tag{5.9}$$

If the APV is with a small beam size, the wave vector mismatch will be large, and the nonlinear conversion described by Eqs. (5.7) and (5.8) will be not predicted accurately. Therefore, in this chapter, a relatively large APV is chosen to make Δk for different OAM negligible. When this condition is satisfied, if the multiple OAM modes are generated using the HOBBIT system, Eq. (5.7) can be further expanded to Eq. (5.10). Note that if these conditions are used, the mathematical description of Eq. (4.5) will stand, and the nonlinear interaction will have a much simpler illustration.

$$A_2(L) = \frac{i\omega_2^2 d_{eff}}{k_2 c^2}\left(\frac{\exp(i\Delta kL)-1}{i\Delta k}\right)\sum_{p,q\in n} A_p A_q. \tag{5.10}$$

The 1 μm HOBBIT system is used to generate the APV which is also used in chapter 4 to generate the asymmetric BG beams. The reverse HOBBIT system working at 532 nm is utilized to measure the OAM spectrum. The 1 μm CW HOBBIT system and the reverse HOBBIT system can be seen in Fig. 5.3.1. Two essential elements in the HOBBIT systems are the AOD and the log-polar optics. The log-polar optics perform geometric coordinate transformations which can convert cartesian coordinate and polar coordinate to each other. The coordinate transformation corresponds to the exchange between the OAM azimuthal phase gradient and linear phase which are the processes of generating and detecting OAM. The AOD is driven by an RF signal with a specific frequency which can deflect the incident beam to a designed angle or transfer a beam carrying linear phase back to flat phase. By using the AOD, each OAM mode is tagged to one frequency due to the Doppler frequency shift. This enables us to explore the interaction between different OAM modes by measuring the beat frequencies. The APV generated by the 1 μm HOBBIT system is imaged by a 10X reducing telescope to the center of a 20 mm long PPLN crystal with a period of 6.93 μm which is the same as the one used in chapter 4. The generated APV can be expressed as,

$$\begin{aligned}\vec{U}(r,\theta,z,t) &= \hat{y}S(t)\exp(i2\pi f_c t)A(r,\theta)\exp(-i\ell\theta - ikz) \\ &= \hat{y}\sum_n c_n \exp\left[i\left(2\pi f_n(t)t + \phi_n\right)\right]\exp(i2\pi f_c t) \\ &\quad \times \exp\left(-\frac{(r-r_0)^2}{w_r^{\,2}} - \frac{\theta^2}{w_\theta^{\,2}}\right)\exp\left(-i\ell_n(t)\theta - ik_{zn}z\right),\end{aligned} \tag{5.11}$$

where $\hat{y}$ denotes the vertical polarization, $S(t)=\sum_n c_n \exp\left[i\left(2\pi f_n(t)t+\phi_n\right)\right]$ is the RF signal driving the HOBBIT system, c_n controls the power ratio of each OAM component, $f_n(t)$ is the frequency function which can be used to generate static or dynamic OAM, ϕ_n is the initial phase for each component, f_c is the incident light frequency, $A(r,\theta)$ is the amplitude distribution, $\ell_n(t)=\frac{2\pi a}{V_{at}\eta_t}\left[f_{AOD}-f_n(t)\right]$, $a=\frac{3.6\,mm}{2\pi}$ is the log-polar parameter, V_{at} is acoustic velocity, $\eta_t=\frac{F_2}{F_1}$ is the imaging index of the lens system, f_{AOD} is the central frequency of the transmitter AOD, and $k_{zn}=2\pi\cos\left(\lambda_{\ell n}\ell_n(t)/2\pi a\right)/\lambda_{\ell n}$ is the longitudinal wave number.

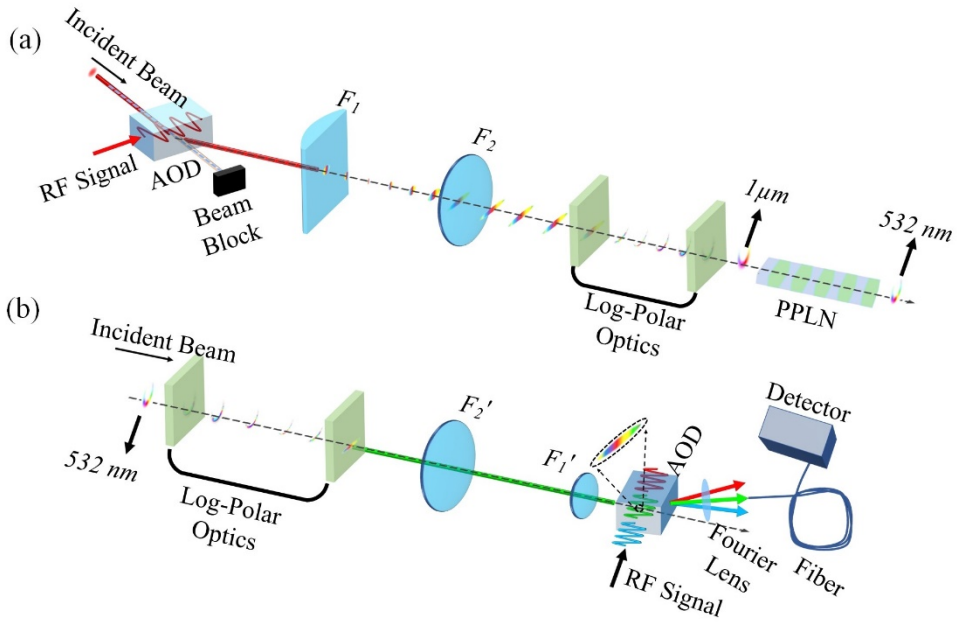

Fig. 5.3.1. (a) The 1 μm HOBBIT system. (b) The reverse HOBBIT system [86].

The reverse HOBBIT system is a real-time OAM cross-correlator, which is the reverse process of the HOBBIT system. The detailed explanation of the HOBBIT and the reverse HOBBIT can be found in chapter 2. The correlation in the reverse HOBBIT can be described by Eq. (2.12). As mentioned earlier, a 20 mm long periodically poled lithium niobate (PPLN) nonlinear crystal (Covesion MSHG1064-1.0-20) with a grating period of 6.93 μm was used as the nonlinear medium. Considering the length of the nonlinear crystal, a beam diameter of 300 μm is chosen to ensure the invariance of the beam propagation in the crystal. Using this beam diameter, the phase-matching condition for different OAM modes is evaluated. Based on Eq. (5.9), the wave vector mismatch for OAM in the range of -10 to +10 can be ignored. This result can be found got by calculating the conversion efficiency for OAM charge 10 at the perfect phase-matching condition for OAM charge 0 using Eq. (5.8), which results in $\mathrm{sinc}^2(\Delta kL/2) = 0.9534$. With a smaller diameter and a larger OAM value, the phase mismatch caused by the OAM spiraling k vector cannot be ignored and relative results will be discussed later with the 2D HOBBIT system.

The experimental results of the SHG of APV are shown in Fig. 5.3.2. Figure 5.3.2(a) shows the intensity distribution of the fundamental and SHG fields. We can see both fields are APV but with different asymmetry due to the nonlinear process being power density related. The 5 discrete SHG OAM charges measurements are shown in Fig. 5.3.2(b) with an incident fundamental APV carrying OAM charges -1, -0.5, 0, +0.5, +1. The measured results show corresponding doubled charges. The OAM mapping curve from the fundamental APV to the SHG APV can be seen in Fig. 5.3.2(c) and the fundamental OAM

range is from -1 to +1 with a step of 0.1. According to the results the mapping curve has a linear one-to-one correspondence and each single fundamental OAM charge is accurately doubled in the SHG which is predicted by the theory discussed earlier.

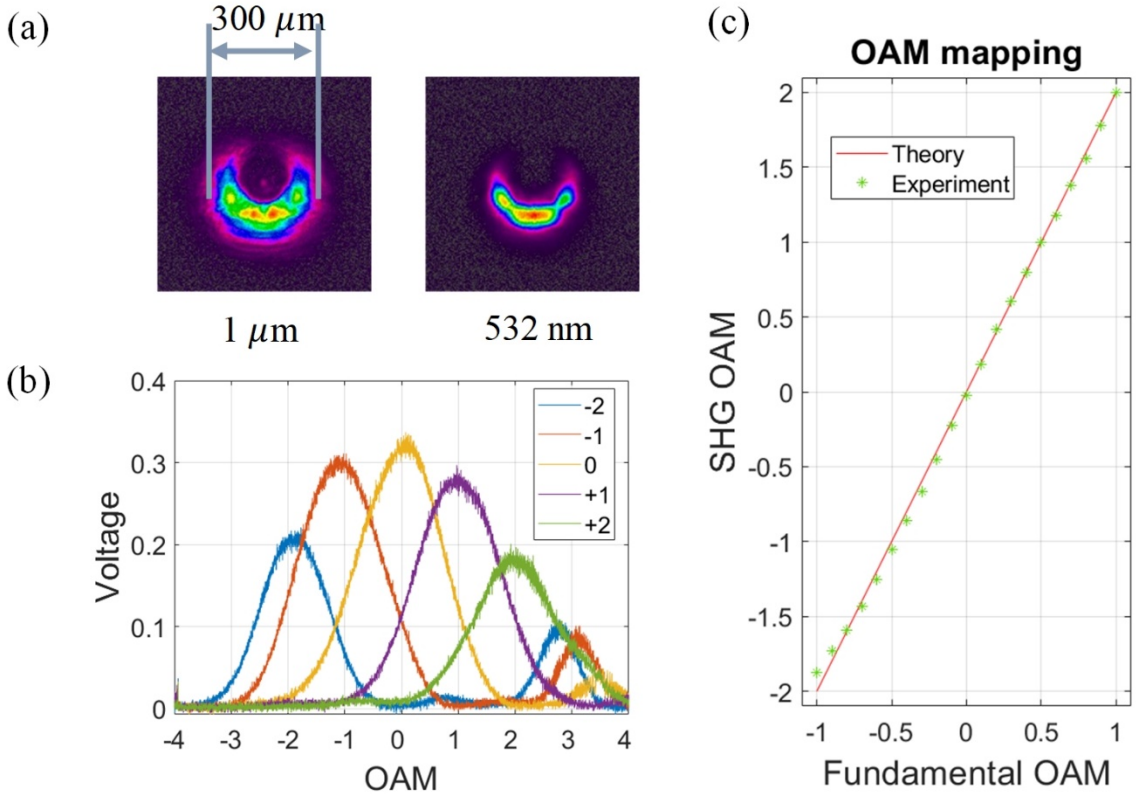

Fig. 5.3.2. (a) Experimentally captured intensity distributions of the fundamental and SHG APV. (b) SHG OAM charges measurements resulting from the fundamental APV with OAM -1, -0.5, 0, +0.5 and +1. (c) The OAM mapping curve of the SHG of APV with fundamental beam carrying OAM from -1 to +1 with a step of 0.1 [86].

The APV not only carries fractional OAM with a linear mapping curve but also simplifies the nonlinear conversion process by having a relatively simple amplitude and phase distribution. The elimination of the phase discontinuity in the beam profile improves the nonlinear conversion property of the APV. Since the nonlinear interaction of multiple

APV beams can be analyzed mathematically. Substituting Eq. (5.11) into Eq. (5.10), the SHG field of multiple APV interaction can be derived as follows,

$$\vec{U}_{SHG} = \exp\left(-\frac{2\left(r-\rho_0\right)^2}{w_{ring}^2}-\frac{2\theta^2}{\beta^2\pi^2}\right)\exp(i2\pi 2f_c t)\sum_{p,q\in n}\exp\left[i\left(2\pi(f_p+f_q)t+\varphi_p+\varphi_q\right)\right] \times \exp\left(-i(l_p+l_q)\theta\right)\exp\left(-i(k_p+k_q)z\right)\hat{y}. \quad (5.12)$$

Since each fundamental OAM is Doppler frequency tagged due to the transmitter AOD, the SHG field of multiple APV interactions will carry different beat frequencies. By measuring the beat frequencies using the reverse HOBBIT system, the complex coefficients of the SHG OAM components can be extracted and then the multiple OAM nonlinear interaction theory can be verified. Considering the interaction of any two OAM charges may give the same OAM charge carrying the same Doppler frequency shift, the summation of sinusoidal waves with the same frequency may change the amplitude and phase on this frequency and by measuring the amplitude and phase, the interaction can be confirmed. First, the sinusoidal waves summation theory will be evaluated. In Eq. (5.13), $z(t)$ is the signal carrying a summation of sine waves, in which every frequency has a specific amplitude and phase. Equation (5.14) shows how to get the information carried by the beat frequencies.

$$z(t)=\sum_{k=1}^{N}A_k\exp\left[i\left(\omega_k t+\varphi_k\right)\right], \quad (5.13)$$

$$|z|^2=\sum_{k=1}^{N}{A_k}^2+\sum_{m=1}^{N}\sum_{k=m+1}^{N}2A_kA_m\cos\left[\left(\omega_k-\omega_m\right)t+\phi_k-\phi_m\right]. \quad (5.14)$$

An example of how to verify the multiple OAM interaction theory with APV in Eq. (5.12) can be seen in Fig. 5.3.3. The fundamental beam includes 3 OAM charges which are

-0.5, 0 and +0.5. Considering all the interactions between any two modes, the SHG field will contain 5 different OAM charges which are -1, -0.5, 0, +0.5, and +1. A sequence of phase values is embedded in the RF signal to generate -0.5, resulting in the beat frequency information being changed due to different phase values. Five phase values are chosen as follows, $\phi_n \in \left[0, \pi/4, \pi/2, \pi, 3\pi/4\right]$. The measured SHG OAM spectrogram with initial phase changing in 2 ms increments is shown in Fig. 5.3.3(a). Since it is a summation of 5 OAM modes, the waveform captured by the scope will not show individual OAM charges. The 1 μm HOBBIT system is designed to have a Doppler frequency difference of 5.8 MHz for an OAM charge. The relationship of the beat frequencies among all the 5 SHG OAM modes is shown in Fig. 5.3.3(b). The beat frequency will be the same for two OAM modes having the same OAM steps, so for simplicity, only one beat frequency is labeled in the figure for each OAM step. By doing an FFT analysis of each column of Fig. 5.3.3(a), the beat frequency information can be extracted and the frequency spectrogram can be seen in Fig. 5.3.3(c). The frequency spectrogram includes 4 main peaks which correspond to the beat frequencies of 2.9 MHz, 5.8 MHz, 8.7 MHz, and 11.6 MHz. The amplitude differences in each increment are due to the initial phase setting of the OAM -0.5 which causes the destructive interference in the spectrogram.

The magnitude and phase information can be extracted from the frequency spectrogram and the results are shown in Fig. 5.3.4(a). The destructive interference can be seen with more details. The Eq. (5.13) and Eq. (5.14) are used to theoretically calculate the final phase values for each increment. These final phases for the beat frequencies 2.9 MHz,

5.8 MHz, 8.7 MHz, and 11.6 MHz are $0.5\phi_n$, ϕ_n , $1.5\phi_n$, and $2\phi_n$ respectively. The experimentally measured phase values in each increment are plotted in Fig. 5.3.4(b). At the beat frequencies 2.9 MHz and 5.8 MHz, we can see the curves show the phase changes of $0.5\phi_n$ and ϕ_n exactly. However, the beat frequencies 8.7 MHz and 11.6 MHz show much noisier curves which is due to a reduced signal level that decreases the phase measurement accuracy. However, the phase measurement verifies the multiple OAM interaction theory in Eq. (5.12) using APV.

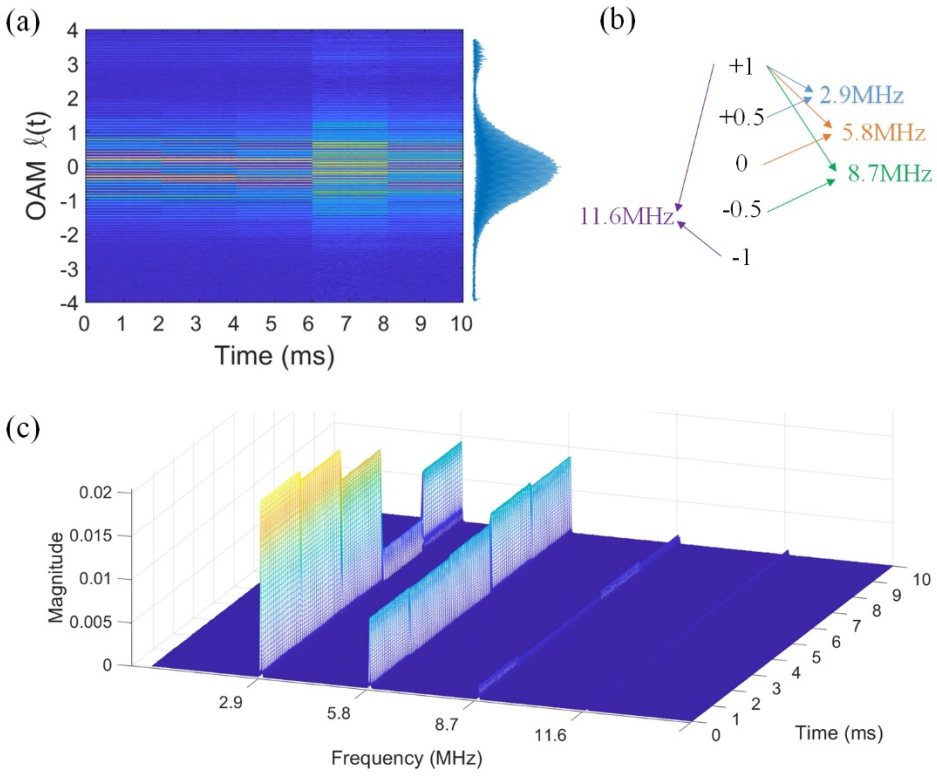

Fig. 5.3.3. Experimental results of multiple OAM interaction in SHG. (a) OAM spectrogram of the SHG field with 5 increments. (b) The beat frequency information for any two OAM modes in the SHG field. For simplicity, only one beat frequency is labeled

for two OAM with a step. (c) The measured frequency spectrogram after applying FFT to the OAM spectrogram [86].

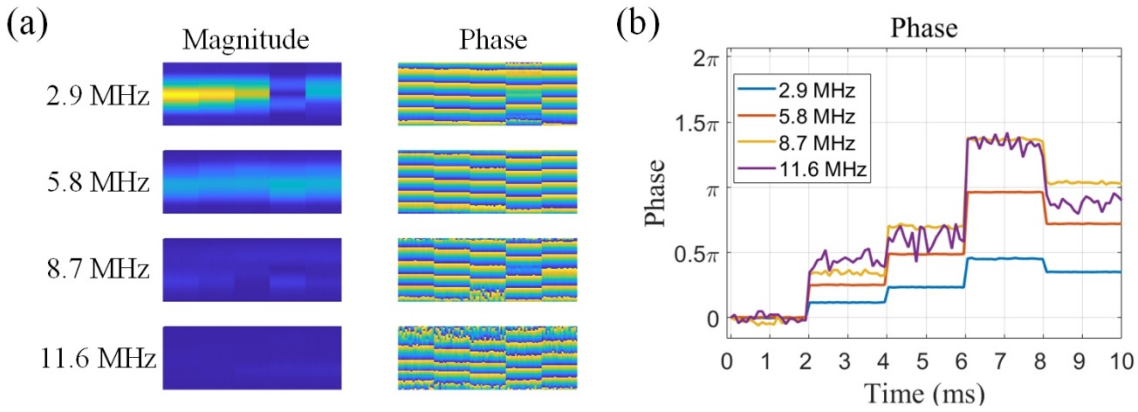

Fig. 5.3.4. (a) The extracted magnitude and phase information from the frequency spectrogram. (b) The measured phase curves from the beat frequencies [86].

In this section, the SHG of the APV beams with theoretical and experimental results were studied. The theoretical analysis of the APV carrying linear OAM mapping curve is given and the coupled wave theory for SHG is discussed. With the APV, a linear one-to-one mapping curve for the SHG OAM is created which is an enhanced improvement to the asymmetric BG beams. Due to the use of the HOBBIT systems, each OAM is frequency tagged, which allows us to verify the multiple OAM interaction theory. The experimental results fit well with the theoretical prediction which proves that the APV has advantages in generating fractional OAM and doing multiple OAM interaction in nonlinear processes. In our experiment, the APV solves the three problems that must be considered in OAM-involved nonlinear interaction. The power density and the mode overlapping issues are fixed by using the RF signals and the OAM-independent beam size. A relatively large beam diameter is used to eliminate the spiraling k vector problem, and in an OAM range from -

10 to +10, the phase-matching condition can be considered approximately the same. However, with smaller beam sizes and larger OAM, the phase-matching condition is still an important factor in OAM-involved nonlinear processes.

5.4 Deep UV OAM beams generation with high charges

In the former section, the advantages of using the APV to generate new light frequencies and new fractional OAM charges has been introduced. The asymmetric complex amplitude structure enables the elimination of the natural phase discontinuities in the beam profile, which help maintain the beam along propagation and help retail the fractional charge. Both the fundamental beams and the SHG beams carry fractional OAM with a linear one-to-one correspondence mapping curve. The results show promising manipulation of OAM in nonlinear interactions. In this section, the possibility of generating APV beams carrying high OAM charges in SHG and the factors that impact the nonlinear interaction will be explored and discussed.

The nonlinear optics theory is important to quantum technology. The photon pairs generated from the SPDC process are usually used as entangled states [89]. Compared to other ways of generating entangled states, the quantum optics method works at room temperature and can be easily controlled by using nonlinear crystals. High dimensionality is another requirement for quantum applications, and the spatial modes provide the option to involve the nonlinear processes and the OAM modes together. According to the results in [19], the SPDC generated photon pairs with a Gaussian beam pump will be a superposition of infinite OAM spectrum, which is a natural property of quantum entanglement. However, with the Gaussian pump, the generated superposition of the spatial

modes in the photon pairs has a Gaussian-shape distribution which is centered at OAM 0. This distribution is called the spiral bandwidth. For specific applications like quantum teleportation [90], it is essential to have a balanced spiral bandwidth which means the coefficients for each component in the superposition should be equalized. As a result, post-selection methods like the so-called Procrustean method used in [19] are used to manipulate the spatial mode spectrum generated by the SPDC. However, the post-selection methods may cause security issues and post-selection free methods have been developed to overcome this effect [91-94]. The usual method to balance the spiral bandwidth is to use a pump of superposition of OAM modes with radial controls. It is then essential to generate deep UV OAM beams whose wavelength is the common band used in quantum optics. However, it is hard to use regular methods to generate such beams. For example, most SLMs are not suitable for UV beams whose wavelength is shorter than 400 nm, and shorter wavelengths make it hard to solve the resolution issue using lithography methods. Another option is to use nonlinear interaction to generate the desired superposed OAM modes in the UV band and use them as the input to the SPDC. Since controlling the radial and OAM modes together will be a requirement, the 2D HOBBIT system is perfect for generating such modes. In this section, the SHG to generate high-order OAM and radial APV beams with all different combinations will be introduced.

Considering that the SHG process of the spatial APV is being studied, Eq. (5.12) can be updated as follows,

$$\vec{U}_{SHG} = \hat{y}\exp\left(-\frac{2\left(r-r_n\right)^2}{w_r^2}-\frac{2\theta^2}{w_\theta{}^2}\right)\exp(i2\pi 2 f_c t)$$
$$\times \sum_{p,q\in n}\exp\left[i\left(2\pi(f_p+f_q)t+\varphi_p+\varphi_q\right)\right]\exp\left(-i(l_p+l_q)\theta\right)\exp\left(-i(k_p+k_q)z\right).$$

(5.15)

The radial modes of the spatial APV can be considered as orthogonal to each other, and the multiple OAM interaction has been discussed in section 3. The relative simulation results of single OAM, multiple OAM, and multiple radial modes using Eq. (5.15) are shown in Fig. 5.4.1. The first row shows the fundamental APV beams carrying 3 different integer charges, 2 superposed OAM charges, and multiple OAM and radial modes. The single OAM charges show the beam size invariance at the same radial mode. The interference pattern of multiple OAM and radial modes can be seen. The second row shows the simulation results of the SHG APV with Eq. (5.15). We can observe that the beam sizes of the fundamental and SHG APV are the same, except for the higher asymmetry of the SHG APV since the nonlinear interaction is power intensity relevant. The SHG APV is propagated to the far-field to observe the OAM charge related effect. From the single OAM charges results, we can see the SHG far-field is the Bessel beam whose beam size is OAM-dependent. The results for multiple modes are very interesting since the interaction between multiple OAM will generate more modes causing the interference pattern in the far-field to be very complex. If we take a fundamental beam carrying ±3 for example, then the generated SHG APV should carry 3 OAM charges: +6, -6, and 0. The APV far-field shows the interference pattern of these 3 Bessel modes. Similar results can be observed from the other two results with multiple OAM and radial modes.

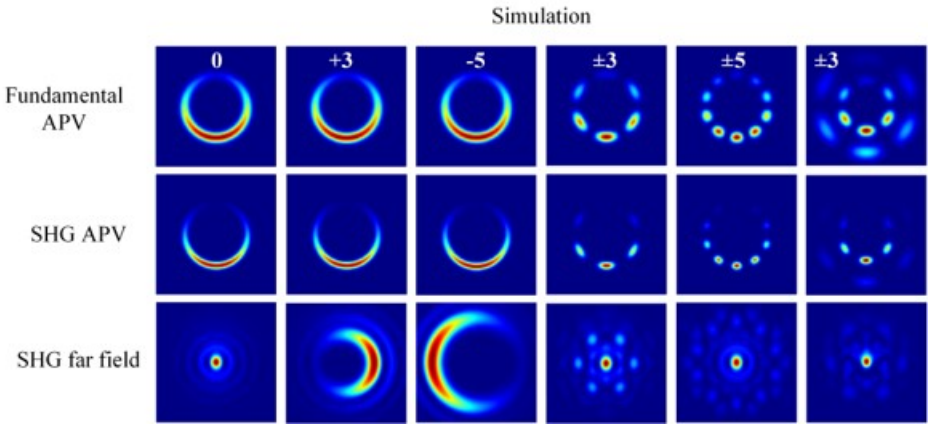

Fig. 5.4.1. Simulation results of the spatial APV in SHG [95].

There are three main factors impacting the nonlinear interaction with OAM beams, power density, mode overlapping, and phase-matching condition. As discussed earlier, the RF signal driving the HOBBIT system can be used to control the power density, and the mode overlapping issue can be fixed by exploiting the APV with OAM-independent beam size. The phase-matching condition is affected by the k vector mismatch between different OAM modes. And the skew angle is both related to OAM and beam size and can be expressed by $\theta = \frac{\ell}{kr}$, where r here denotes the radius of the beam. Since the 2D HOBBIT system can generate different radial APV, it will be convenient to study how the beam size will affect the SHG results. The experimental results are shown in Fig. 5.4.2. The parameters of the 2D HOBBIT can be found in chapter 3. The nonlinear crystal used in this experiment is a 0.3 mm Type-I BBO (Eksma optics BBO-644H). The spatial APV is imaged to the center of the crystal using a reducing telescope. Two different beam diameters, 250 μm and 125 μm, are chosen and can be seen in the results. For the fundamental APV at 250 μm, we can see the beam sizes for different OAM are very

constant. But for the fundamental APV at 125 μm, a rotation for higher OAM can be observed. This is due to the basic nature of the log-polar coordinate transformation which is perfect for plane waves but will cause distortion on the APV distributions due to the larger linear phase gradients during the wrapping procedure. The far-fields after propagation of the fundamental APV are shown in the second row. The SHG APV beams are shown in the third row and similar intensity patterns can be observed for both beam diameters. The BBO crystal is aligned based on the phase-matching condition for OAM 0. The SHG APV appears worse at higher OAM charges which is due to the k vector mismatch. If the results using different beam diameters are compared, we can conclude that the intensity pattern is better for large beam sizes. The propagation of the SHG APV is shown in the last row.

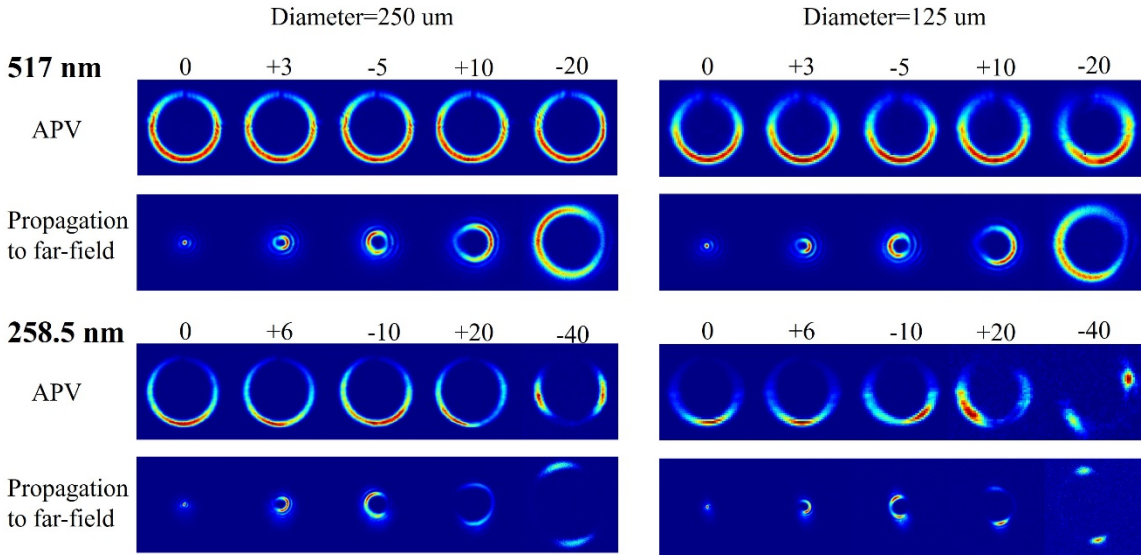

Fig. 5.4.2. The SHG results with APV with different beam sizes.

With the generated deep UV OAM beams shown in Fig. 5.4.2, the generation of high OAM needs to be confirmed. It is hard to detect the OAM charges directly at 258.5

nm, but the OAM interference pattern can be used to verify the charges. The results are shown in Fig. 5.4.3. The 517 nm APV beams carrying ± 20 are generated, and after the SHG process, 3 OAM modes of 0, +40, and -40 will be included in the field. The ± 40 will show 80 petals which proves the generation of the charge. We can observe a bright Bessel spot in the SHG APV beams which corresponds to OAM 0. However, the power intensity of the higher OAM charge is so low that nearly no intensity can be seen. By using the image processing technique, the central spot can be filtered out to enhance the contrast of the residual field and we can see the interference pattern. Due to the imperfectness of the phase-matching condition for higher OAM, the beam diameter of the pattern and the distance between two petals need to be measured to estimate the petal numbers. The experimentally measured results are shown in the figure. With a beam diameter of 1202.94 μm and a petal distance of 47.97 μm, the number of petals is $1202.94 \times \pi / 47.97 + 1 = 79.78$, which is very close to the theoretical number of petals for ± 40. This small variance is due to measurement error. We can say the generation of deep UV carrying high OAM is verified by doing such an experiment.

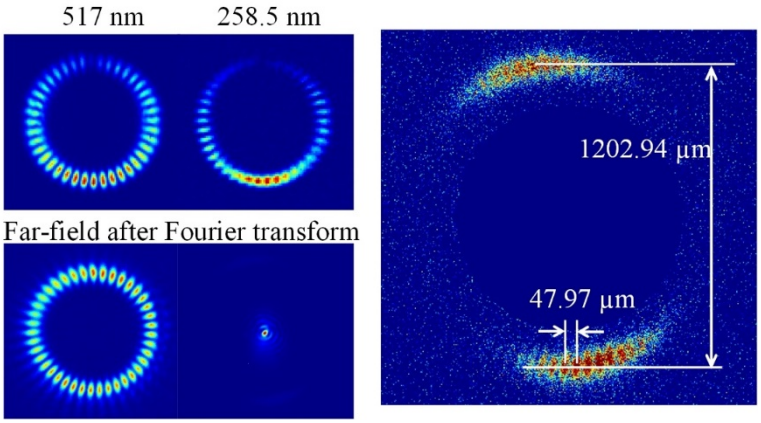

Fig. 5.4.3. Verification of the SHG APV carrying OAM 40.

Next, we want to show the SHG results involving multiple OAM and multiple radial modes since both dimensions can be used to manipulate the OAM spiral bandwidth in SPDC. The results are shown in Fig. 5.4.4. The first two rows show the fundamental APV beams and the relative far-field distributions through propagation. The typical interference patterns can be seen, and for the far-field of multiple radial modes, we can observe multiple ring patterns as well. The fundamental APV beams are sent to the BBO crystal and the SHG APV beams are shown in the third row. Considering all of the interactions, the OAM charges are labeled above the figure. The far-field of the SHG APV can be seen in the fourth row which shows similar interference patterns as the simulation results shown in Fig. 5.4.1.

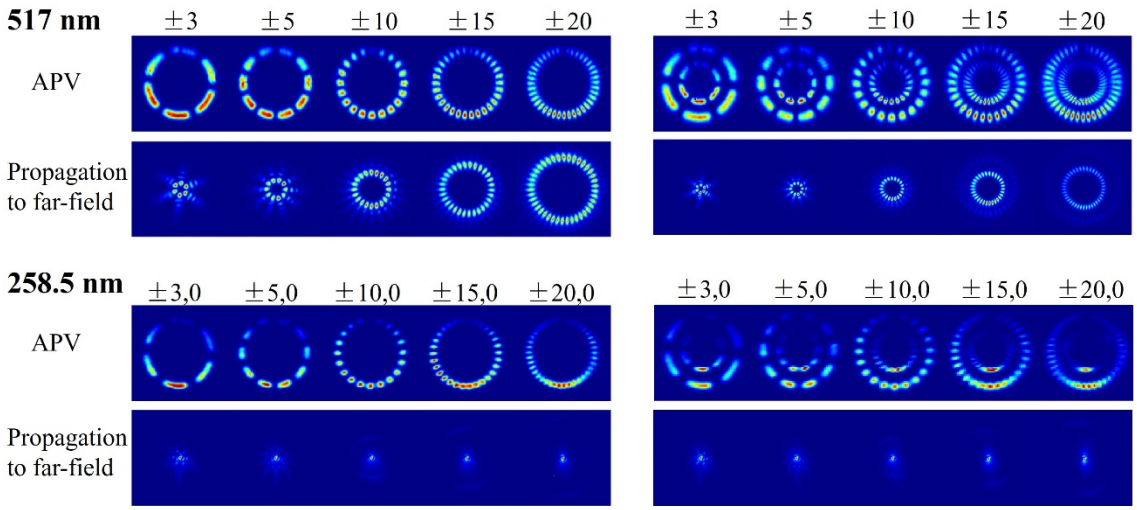

Fig. 5.4.4. SHG APV results with multiple OAM and radial modes.

In this section, the results generated using spatial APV generated by the 2D HOBBIT system with high OAM and multiple radial modes are demonstrated. Our results confirmed the APV SHG theory illustrated earlier and generate deep UV OAM beams

carrying OAM as high as 40. For high OAM SHG, the phase-matching condition related to the k vector mismatch cannot be ignored and some parts on the beam profiles have lower power intensity. This can be further improved by using different types of phase-matching crystals such as quasi-phase-matching. The multiple OAM and radial modes nonlinear interaction results are also shown. Our results show promising applications in quantum technology, providing a method to generate deep UV OAM beams and manipulate the OAM spiral bandwidth, which is essential in some quantum applications.

5.5 Conclusion

In summary, the SHG of APV beams is demonstrated in this chapter. The APV beams, which have OAM-independent beam sizes, are promising tools to explore how OAM charges, the only parameter, can impact the converted modes in the SHG field. The theoretical analysis based on the electromagnetic theory on the global OAM carried by the APV is first demonstrated. Usually, the phase structure is the most important feature for OAM beams, however, both amplitude and phase will affect the global OAM in the field. This analysis shows the reason why our beams generated by the HOBBIT can carry OAM with a linear one-to-one correspondence mapping curve. The SHG theory based on coupled-wave equations was then illustrated. Due to the asymmetric structure of the light field, the phase discontinuities are eliminated from the complex amplitude and the OAM charge is exactly doubled in the SHG beams. Based on the theory, the 1 μm HOBBIT system and a PPLN crystal are utilized to do the SHG process. The reverse HOBBIT system is used to measure the OAM in the generated fields. An input beam carrying fractional OAM from -1 to +1 with a step of 0.1 is studied. The OAM mapping curve for the SHG

fields also shows a very good linear one-to-one correspondence depicting a linear curve from -2 to +2 with a step of 0.2, compared to the results in the former chapter with asymmetric BG beams. This is due to the simpler amplitude and phase structure of the APV. A relatively large beam size of 300 μm is used in this experiment so that the phase-matching condition for a range of OAM from -10 to +10 can be considered the same. Due to the natural property of the HOBBIT beams carrying a tagged Doppler frequency, the reverse HOBBIT can extract the beat frequency information from multiple OAM beams and verify the multiple mode interaction theory using APV. An input beam carrying 3 OAM charges of 0, +0.5, and -0.5 respectively, is sent to the crystal and, by varying the initial phase of -0.5, constructive and destructive interference can be seen in the generated field. The 5 OAM of -1, -0.5, 0, +0.5, and +1 are included in the SHG field, considering all the interactions. OAM components will have a beat frequency and the final phase information for each beat frequency can be theoretically calculated. By using the reverse HOBBIT system, the OAM, frequency, and phase spectrograms are collected experimentally. The results fit well with the theoretical predictions and verify the multiple OAM interaction theory with APV.

The nonlinear interaction theory with APV was then used to generate deep UV OAM beams. The UV beams and spatial modes are widely used in quantum technology. For a Gaussian pump, the generated field through an SPDC process will carry a superposition state which can be thought of as a high dimensional entanglement state. However, this state includes an OAM spectrum whose spiral bandwidth has unbalanced coefficients. To equalize the coefficients, post-selection filtering methods are usually used.

However, the post-selection compromises the quality of the quantum states. Some references have shown that by tailoring the input states carrying multiple OAM and radial modes, the spiral bandwidth of the SPDC generated field can be balanced, which indicates the generation of deep UV beams carrying OAM and radial information. Considering this, the 2D HOBBIT is a perfect choice to generate spatial APV which can be thought of as carrying both OAM and radial information. The 2D HOBBIT and a type-I BBO crystal are used to explore the impacting factors of the SHG process. Single OAM, multiple OAM, and radial modes are sent to the BBO. As mentioned in former chapters, power density, phase-matching condition, and mode overlapping are the most important factors for OAM-involved nonlinear interactions. Using HOBBIT generated APV beams, the power density, and mode overlapping problems can be solved since the power density can be controlled by the RF signal and the APV has an OAM-independent beam size. The phase-matching condition is due to the k vector mismatch whose angle is related to both the OAM charge and the beam size. Based on this, APV beams with 2 different beam diameters, 250 μm and 125 μm, are used to generate deep UV OAM beams. The results show similarities between the 2 diameters but with a better beam quality for the larger beam. Also, for higher OAM charges, the intensity distributions show lower density in regional areas which is due to the phase-matching around the ring being nonuniform. This can be further improved by using a quasi-phase-matching crystal. To verify the generation of high OAM charges in the UV band, the superposition of ± 20 works as the pump and the petal numbers in the generated field indicates a generation of charge 40. Then the multiple OAM and radial

modes conversion in the SHG is experimentally executed and the results match the theory and the simulation results.

Our work on the nonlinear interaction with APV beams shows the possibility to isolate the OAM as the only factor being varied in the conversion. With the results using the asymmetric BG beams, our work explores the basic nature of what affects the OAM-involved nonlinear processes and shows how to manipulate the interaction. Our theory can be used to generate new light frequencies carrying tailored OAM which will be useful in applications such as optical communications and quantum technology. It is the first work showing how fractional OAM can be controlled and how it behaves in nonlinear interactions. The linear one-to-one correspondence in both fundamental and SHG fields shows the potential to enhance the light spectrum efficiency and increase the channel capacity.

CHAPTER SIX

CONCLUSION AND FUTURE WORK

6.1 Conclusion

In this work, driven by the promising applications of structured light in fields like optical communications, remote sensing, and quantum technology, the generation, manipulation, and detection of APV beams carrying both integer and fractional OAM charges are studied. Methods based on the HOBBIT concept are developed. The nonlinear interaction of APV beams is studied for understanding and manipulating the beam arbitrarily.

First, the CW HOBBIT system and reverse HOBBIT systems were introduced. By using AOD and log-polar optics in the systems, the beam can be generated and measured rapidly up to MHz level. Driven by carefully designed RF signals, the HOBBIT system can generate time-varying APV beams carrying integer, fractional, and combined OAM. The benefit of an APV is the property of OAM independence which enables the matter interaction only caused by OAM. One feature using the AOD is the Doppler frequency shift between different modes. The reverse HOBBIT system uses the AOD and log-polar optics in reverse order, compared to the HOBBIT system. Driven by a linear RF chirp, the results using the reverse HOBBIT to detect the generated modes by the HOBBIT show the real-time cross-correlation of the input beam and the detection scheme. By using the FFT method, the beat frequency information can be extracted from the measured results and the frequency and phase spectrograms can be used to build the Poincaré sphere which is widely

used for information coding and decoding. In addition, the HOBBIT and reverse HOBBIT were used to track the OAM change of a rotating fog density in real-time to give the spatial information of a complex medium.

Then, the 2D pulsed HOBBIT system was demonstrated. By introducing a second AOD into the system, the beam size and OAM can be controlled simultaneously. The generated modes can be considered as a spatial APV basis which can be used for remote sensing tasks. The use of a pulsed source overcomes the Doppler frequency shift problem in a CW HOBBIT and the experimental results show the interference patterns of multiple OAM. By calculating the fidelity using the intensity correlation of the experimental and the simulated results, the generated spatial APV beams show great beam quality. The orthogonality of the generated APV OAM is proved by decomposing the beam into an integer OAM basis and a mode purity more than 97% can be generated through the 2D HOBBIT. The current 2D HOBBIT system enables a fastest mode switching rate of 406.25 kHz. This mode switching speed can be further improved by using a smaller beam size or using AOD with higher acoustic velocity. The spatial APV basis was used to create different types of pulse trains to measure binary amplitude pattern and the rotating fog density. The binary amplitude pattern was recovered ideally by sending OAM interference modes, and the recovered letter size is with high accuracy. For the rotating fog density sensing, the spatial property of the beams enables to measure the radial OAM correlation information, and the further modulation of the RF signals makes the real-time azimuthal localized information can be retrieved from the detection scheme with a single-pixel detector. The theory and experiment of using the 2D HOBBIT and the reverse HOBBIT to

characterize the partial coherence of an APV beam are demonstrated. Our results show the ability to measure the CSD function and to recover the phase of the light field rapidly.

Next, the nonlinear study of the asymmetric Bessel-Gaussian beams was illustrated. The asymmetric BG beams and the APV beams are a Fourier transform pair which are both the generated types of beam models of the HOBBIT system. Different from the APV beams whose beam size is OAM-independent. The asymmetric BG beams have a larger beam size by carrying larger OAM. The study of the SHG of the asymmetric BG beams through a PPLN crystal was given. Three main factors, the power density, the phase matching condition, and the mode overlapping were illustrated to explain the complexity of OAM-involved nonlinear process. The linear one-to-one correspondence of the fractional OAM charge was given for the fundamental asymmetric BG beams which is due to the inherent asymmetry property of the beam model. The SHG beams also show a very good one-to-one correspondence of the fractional charges. The experimental results of integer and fractional OAM were demonstrated. The OAM mapping curve is not purely linear which is due to the asymmetric BG beams having a superposed OAM spectrum. The different situations of multiple asymmetric BG beams in nonlinear interaction were discussed. The propagation of the asymmetric BG beams in the nonlinear crystal will impact the power ratios in the generated beam which allows us to manipulate the interaction by controlling the parameters. The nonlinear transversion efficiency was also given.

The nonlinear conversion of the APV beams was discussed in the following chapter. The electromagnetic theory on APV beams carrying fractional OAM with a linear one-to-one correspondence was demonstrated first. The coupled wave equation was used to study

the SHG of APV beams. The multiple OAM nonlinear interaction theory was derived. The OAM mapping curve of the SHG beams was measured using the reverse HOBBIT and a linear one-to-one correspondence was measured. The multiple OAM interaction theory was verified by sending 3 OAM modes, -0.5, 0, and +0.5 through the nonlinear crystal and measuring the beat Doppler frequency using the reverse HOBBIT system. Using the FFT analysis, the amplitude and phase information of each OAM mode can be extracted and used to verify the interaction. Utilizing the APV nonlinear interaction theory, the spatial APV beams generated by the 2D pulsed HOBBIT (517 nm) were used as pump through a BBO crystal to generate 258.5 nm OAM beams in the UV band. The simulation and experimental results were given and fitted well with each other. Two different beam sizes of APV were studied to show how the skew angle affects the OAM-related conversion. The verification of generation of OAM charge 40 was given by measuring the interference petals when sending ± 20 to the BBO. The experimental results of multiple radial and OAM modes were also given.

6.2 Future work

In the future, more work on the generation and detection of structured light will be carried on. On one hand, the asymmetry of the APV and the asymmetric BG beams shows a very important advantage to create fractional OAM beams which have a linear one-to-one correspondence. On the other hand, although controlling the asymmetry makes the generated beam with a high mode purity, the APV is not a true basis because of the spiral bandwidth of the asymmetric structure. However, this can be improved by either tailoring the RF signal driving the AOD or new designs of optical coordinate transformation.

Building an orthogonal basis will be beneficial to applications requiring high dimensionality. Besides, the embedded Doppler frequency shifts to different OAM modes might have the potential to track any small disturbance caused by the complex media which can be used in remote sensing tasks.

On the detection side, the reverse HOBBIT shows a great performance for measuring OAM spectrum of a CW laser source in real-time. It will be important to develop a pulsed reverse HOBBIT to measure a single pulse's OAM. The appropriate timing is required to locate the pulse's position in time for precise control of the system. The demonstrated reverse HOBBIT in Chapter 2 can be used for detecting APV beams with a specific radial size. However, it is not suitable for the measurement of the radial size and the azimuthal position of the spatial APV generated by the 2D HOBBIT. New considerations of how to measure these parameters are essential to decoding the information carried by these modes. One important feature of the HOBBIT system is multi-mode manipulation since the use of AOD. It is convenient to sum different RF signals carrying different frequencies together to generate multiple OAM modes together. It makes the reverse HOBBIT easy to work as an interferometer. As a result, the spatial correlation information of a single field can be extracted using the reverse HOBBIT which is suitable to measure the spatial coherence of the beam. Partially coherence beam works better as the information carrier for optical communication studies. Our approach might be useful to study the behavior of the partially coherent beams and for the generation of these special beam models.

The nonlinear study of OAM beams is important with both beams having OAM-dependent and OAM-independent beam sizes. The multiple OAM interaction is intriguing and offers a way to generate and manipulate new types of structured light. Manipulation of these beams with higher degrees of freedom is essential for applications involving information encoding and decoding. The multi-mode interaction might also be a new way to excite the generation of new type of structured light such as the Ince-Gaussian modes. Another important area related to OAM-involved nonlinear interaction is the quantum information technology. In Chapter 5, the UV OAM beams are generated through the SHG process and they are the perfect source as the pump of quantum entanglement generation. The embedded high dimensionality of OAM-carrying beams also makes it possible to create highly entangled photons. The current schemes to generate entangled photons are less efficient and need post-selection filters. However, the nonlinear study in this dissertation provides a potential way to generate and manipulate the OAM spiral bandwidth.

The mentioned work in this dissertation offers a way to generate and manipulate fractional OAM, which is important to extend the degrees of freedom to encode and decode information. The generated fractional OAM has a linear one-to-one correspondence of the fractional OAM charges in both fundamental and nonlinear converted fields. Both the schemes to generate and detect these modes are based on the so-called HOBBIT concept which enables the real-time manipulation of structured modes in MHz level. The rapid switching feature is significant in studies like remote sensing which is shown as examples to measure the complex media in this dissertation. The nonlinear study of the APV modes realizes the process of fractional OAM conversion and is important for a better

understanding of the OAM-related nonlinear processes. The study of APV beams is essentially important and has potential for research areas requiring high-dimensional data processing.

6.3 Major contributions

Following is a summarized list of the major contributions realized as a result of the Dissertation research:

- This research was the first to demonstrate the APV beams carry fractional OAM with a linear one-to-one correspondence. This is the prerequisite for using the fractional OAM to do sensing.
- This research was the first to demonstrate a real-time sensing method by measuring continuous OAM spectrum. The reverse HOBBIT can reveal a speed of MHz.
- This research was the first to develop the spatial APV basis for imaging and sensing. The 2D HOBBIT system was developed to generate the spatial APV.
- This research was the first to study how spatial structure of the beam will impact the nonlinear processes. The APV and the asymmetric BG beams showed a one-to-one correspondence of fractional OAM charges after nonlinear conversion.

REFERENCES

1. A. Forbes, M. Oliveira, and M. R. Dennis, “Structured light,” Nat. Photonics **15**, 253–262 (2021).
2. L. Allen, M. Beijersbergen, R. Spreeuw, and J. P. Woerdman, “Orbital angular momentum of light and the transformation of Laguerre-Gaussian laser modes,” Phys. Rev. A **45**(11), 8185-8189 (1992).
3. J. Wang, J.-Y. Yang, I. M. Fazal, N. Ahmed, Y. Yan, H. Huang, Y. Ren, Y. Yue, S. Dolinar, M. Tur and A. E. Willner, “Terabit free-space data transmission employing orbital angular momentum multiplexing,” Nat. Photonics **6**, 488-496 (2012).
4. J. Du, R. Zhang, Z. Zhao, G. Xie, L. Li, H. Song, K. Pang, C. Liu, H. Song, A. Almaiman, B. Lynn, M. Tur, A. E. Willner, “Single-pixel identification of 2-dimensional objects by using complex Laguerre–Gaussian spectrum containing both azimuthal and radial modal indices,” Opt. Commun. **481**, 126557 (2021).
5. M. V. Berry, “Optical vortices evolving from helicoidal integer and fractional phase steps,” J. Opt. A: Pure Appl. Opt. **6**(2), 259–268 (2004).
6. J. B. Götte, S. Franke-Arnold, R. Zambrini, and S. M. Barnett, “Quantum Formulation of Fractional Orbital Angular Momentum,” J. Mod. Opt. **54**, 1723 (2007).
7. A. T. O’Neil, I. MacVicar, L. Allen, and M. J. Padgett, “Intrinsic and Extrinsic Nature of the Orbital Angular Momentum of a Light Beam,” Phys. Rev. Lett. **88**(5), 053601 (2002).
8. V. Kotlyar, A. Kovalev, A. Porfirev, and E. Kozlova, “Orbital angular momentum of a laser beam behind an off-axis spiral phase plate,” Opt. Lett. **44**(15), 3673-3676 (2019).
9. V. V. Kotlyar, A. A. Kovalev, R. V. Skidanov, and V. A. Soifer, “Asymmetric Bessel–Gauss beams,” J. Opt. Soc. Am. A **31**(9), 1977-1983 (2014).

10. J. B. Götte, K. O'Holleran, D. Preece, F. Flossmann, S. Franke-Arnold, S. M. Barnett, and M. J. Padgett, "Light beams with fractional orbital angular momentum and their vortex structure," Opt. Express **16**(2), 993-1006 (2008).
11. W. Li, K. S. Morgan, Y. Li, J. Keith Miller, G. White, R. J. Watkins, and E. G. Johnson, "Rapidly tunable orbital angular momentum (OAM) system for higher order Bessel beams integrated in time (HOBBIT)," Opt. Express **27**(4), 3920-3934 (2019).
12. R. J. Watkins, K. Dai, G. White, W. Li, J. K. Miller, K. S. Morgan, and E. G. Johnson, "Experimental probing of turbulence using a continuous spectrum of asymmetric OAM beams," Opt. Express **28**(2), 924-935 (2020).
13. K. Dholakia, N. B. Simpson, and M. J. Padgett, "Second-harmonic generation and the orbital angular momentum of light," Phys. Rev. A **54**(5), 3742-3745 (1996).
14. J. Courtial, K. Dholakia, L. Allen, and M. J. Padgett, "Second-harmonic generation and the conservation of orbital angular momentum with high-order Laguerre-Gaussian modes," Phys. Rev. A **56**(5), 4193-4196 (1997).
15. Z. Zhou, D. Ding, Y. Jiang, Y. Li, S. Shi, X. Wang, and B. Shi, "Orbital angular momentum light frequency conversion and interference with quasi-phase matching crystals," Opt. Express **22**(17), 20298-20310 (2014).
16. G. Walker, A. S. Arnold, and S. Franke-Arnold, "Trans-Spectral Orbital Angular Momentum Transfer via Four-Wave Mixing in Rb Vapor," Phys. Rev. Lett. **108**(24), 243601 (2012).
17. R. Ni, Y. F. Niu, L. Du, X. P. Hu, Y. Zhang, and S. N. Zhu, "Topological charge transfer in frequency doubling of fractional orbital angular momentum state," Appl. Phys. Lett. **109**(15), 151103 (2016).
18. S. U. Alam, A. S. Rao, A. Ghosh, P. Vaity, and G. K. Samanta, "Nonlinear frequency doubling characteristics of asymmetric vortices of tunable, broad orbital angular momentum spectrum," Appl. Phys. Lett. **112**(17), 171102 (2018).

19. A. C. Dada, J. Leach, G. S. Buller, M. J. Padgett, and E. Andersson, "Experimental high-dimensional two-photon entanglement and violations of generalized bell inequalities," Nat. Phys. **7**, 677–680 (2011).
20. J. Baghdady, K. Miller, K. Morgan, M. Byrd, S. Osler, R. Ragusa, W. Li, B. M. Cochenour, and E. G. Johnson, "Multi-gigabit/s underwater optical communication link using orbital angular momentum multiplexing," Opt. Express **24**(9), 9794-9805 (2016).
21. K. Dai, C. Gao, L. Zhong, Q. Na, and Q. Wang, "Measuring OAM states of light beams with gradually-changing-period gratings," Opt. Lett. **40**(4), 562-565 (2015).
22. V. Denisenko, V. Shvedov, A. S. Desyatnikov, D. N. Neshev, W. Krolikowski, A. Volyar, M. Soskin, and Y. S. Kivshar, "Determination of topological charges of polychromatic optical vortices," Opt. Express **17**(26), 23374-23379 (2009).
23. S. N. Alperin, R. D. Niederriter, J. T. Gopinath, and M. E. Siemens, "Quantitative measurement of the orbital angular momentum of light with a single, stationary lens," Opt. Lett. **41**(21), 5019-5022 (2016).
24. V. V. Kotlyar, A. A. Kovalev, and A. P. Porfirev, "Calculation of fractional orbital angular momentum of superpositions of optical vortices by intensity moments," Opt. Express **27**(8), 11236–11251 (2019).
25. J. Leach, M. J. Padgett, S. M. Barnett, S. Franke-Arnold, and J. Courtial, "Measuring the Orbital Angular Momentum of a Single Photon," Phys. Rev. Lett. **88**(25), 257901 (2002).
26. N. K. Fontaine, R. Ryf, H. Chen, D. T. Neilson, K. Kim, and J. Carpenter, "Laguerre-Gaussian mode sorter," Nat. Commun. **10**(1), 1865 (2019).
27. S. Wei, S. K. Earl, J. Lin, S. S. Kou, and X. Yuan, "Active sorting of orbital angular momentum states of light with a cascaded tunable resonator," Light: Sci. Appl. **9**(1), 10 (2020).
28. X. Gu, M. Krenn, M. Erhard, and A. Zeilinger, "Gouy Phase Radial Mode Sorter for Light: Concepts and Experiments," Phys. Rev. Lett. **120**(10), 103601 (2018).

29. M. P. J. Lavery, F. C. Speirits, S. M. Barnett, M. J. Padgett, “Detection of a spinning object using light's orbital angular momentum,” Science **341**(6145), 537-540 (2013).
30. H. Zhou, D. Fu, J. Dong, P. Zhang, D. Chen, X. Cai, F. Li, and X. Zhang, “Orbital angular momentum complex spectrum analyzer for vortex light based on the rotational Doppler effect,” Light Sci. Appl. **6**(4), e16251 (2017).
31. G. C. G. Berkhout, M. P. J. Lavery, J. Courtial, M. W. Beijersbergen, and M. J. Padgett, “Efficient Sorting of Orbital Angular Momentum States of Light,” Phys. Rev. Lett. **105**(15), 153601 (2010).
32. M. Mirhosseini, M. Malik, Z. Shi, and R. W. Boyd, “Efficient separation of the orbital angular momentum eigenstates of light,” Nat. Commun. **4**(1), 2781 (2013).
33. C. Wan, J. Chen, and Q. Zhan, “Tailoring optical orbital angular momentum spectrum with spiral complex field modulation,” Opt. Express **25**(13), 15108–15117 (2017).
34. B. Braverman, A. Skerjanc, N. Sullivan, and R. W. Boyd, “Fast generation and detection of spatial modes of light using an acousto-optic modulator,” Opt. Express **28**(20), 29112–29121 (2020).
35. Alexander Q. Anderson, Elizabeth F. Strong, Brendan M. Heffernan, Mark E. Siemens, Gregory B. Rieker, and Juliet T. Gopinath, “Detection technique effect on rotational Doppler measurements,” Opt. Lett. **45**(9), 2636-2639 (2020).
36. Zhimeng Li, Tong Liu, Yuan Ren, Song Qiu, Chen Wang, and Hua Wang, “Direction-sensitive detection of a spinning object using dual-frequency vortex light,” Opt. Express **29**(5), 7453-7463 (2021).
37. Alexander Q. Anderson, Elizabeth F. Strong, Brendan M. Heffernan, Mark E. Siemens, Gregory B. Rieker, and Juliet T. Gopinath, “Observation of the rotational Doppler shift with spatially incoherent light,” Opt. Express **29**(3), 4058-4066 (2021).
38. A. Belmonte, C. Rosales-Guzmán, and J. P. Torres, “Measurement of flow vorticity with helical beams of light,” Optica **2**(11), 1002-1005 (2015).

39. J. Leach, B. Jack, J. Romero, D. Ireland, S. Franke-Arnold, S. Barnett, M. Padgett, "Quantum imaging and orbital angular momentum," Proc. SPIE 7613, Complex Light and Optical Forces IV, 76130L (2010).

40. Y. Li, Z. Zhou, D. Ding, and B. Shi, "Sum frequency generation with two orbital angular momentum carrying laser beams," J. Opt. Soc. Am. B **32**(3), 407–411 (2015).

41. K. Miyamoto, K. Sano, T. Miyakawa, H. Niinomi, K. Toyoda, A. Vallés, and T. Omatsu, "Generation of high-quality terahertz OAM mode based on soft-aperture difference frequency generation," Opt. Express **27**(22), 31840–31849 (2019).

42. F. Kong, C. Zhang, F. Bouchard, Z. Li, G. G. Brown, D. H. Ko, T. J. Hammond, L. Arissian, R. W. Boyd, E. Karimi, and P. B. Corkum, "Controlling the orbital angular momentum of high harmonic vortices," Nat. Commun. **8**, 14970 (2017).

43. G. Gariepy, J. Leach, K. T. Kim, T. J. Hammond, E. Frumker, R.W. Boyd, and P. B. Corkum, "Creating High-Harmonic Beams with Controlled Orbital Angular Momentum," Phys. Rev. Lett. **113**(15), 153901 (2014).

44. L. Beltran, G. Frascella, A. M. Perez, R. Fickler, P. R. Sharapova, M. Manceau, O. V. Tikhonova, R. W. Boyd, G. Leuchs, and M. V. Chekhova, "Orbital angular momentum modes of high-gain parametric down-conversion," J. Opt. **19**(4), 044005 (2017).

45. A. Chopinaud, M. Jacquey, B. V. de Lesegno, and L. Pruvost, "High helicity vortex conversion in a rubidium vapor," Phys. Rev. A **97**(6), 063806 (2018).

46. A. M. Akulshin, I. Novikova, E. E. Mikhailov, S. A. Suslov, and R. J. McLean, "Arithmetic with optical topological charges in stepwise-excited Rb vapor," Opt. Lett. **41**(6), 1146–1149 (2016).

47. R. F. Offer, D. Stulga, E. Riis, S. Franke-Arnold, and A. S. Arnold, "Spiral bandwidth of four-wave mixing in Rb vapour," Commun. Phys. **1**(1), 84 (2018).

48. R. Mamuti, S. Goto, K. Miyamoto, and T. Omatsu, "Generation of coupled orbital angular momentum modes from an optical vortex parametric laser source," Opt. Express **27**(25), 37025–37033 (2019).

49. P. Stanislovaitis, A. Matijosius, M. Ivanov, and V. Smilgevicius, "Topological charge transformation of beams with embedded fractional phase step in the process of second harmonic generation," J. Opt. **19**(10), 105603 (2017).
50. M. W. Beijerbergen, R. P. C. Coerwinkel, M. Kristensen, and J. P. Woerdman, "Helical-wavefront laser beam produced with a spiral phaseplate," Opt. Commun. **112**(5-6), 321–327 (1994).
51. N. R. Heckenberg, R. McDuff, C. P. Smith, and A. G. White, "Generation of optical phase singularities by computer-generated holograms," Opt. Lett. **17**(3), 221–223 (1992).
52. Y. Wen, I. Chremmos, Y. Chen, J. Zhu, Y. Zhang, and S. Yu, "Spiral transformation for high-resolution and efficient sorting of vortex modes," Phys. Rev. Lett. **120**(19), 193904 (2018).
53. G. Ruffato, M. Massari, and F. Romanato, "Multiplication and division of the orbital angular momentum of light with diffractive transformation optics," Light: Sci. Appl. **8**(1), 113 (2019).
54. O. Bryngdahl, "Geometrical transformations in optics," J. Opt. Soc. Am. **64**(8), 1092–1099 (1974).
55. M. A. Dugan, J. X. Tull, and W. S. Warren, "High-resolution acousto-optic shaping of unamplified and amplified femtosecond laser pulses," J. Opt. Soc. Am. B **14**(9), 2348–2358 (1997).
56. T. Häfner, J. Strauß, C. Roider, J. Heberle, and M. Schmidt, "Tailored laser beam shaping for efficient and accurate microstructuring," Appl. Phys. A **124**(2), 111 (2018).
57. A. Zunino, S. Surdo, and M. Duocastella, "Dynamic Multifocus Laser Writing with Acousto-Optofluidics," Adv. Mater. Technol. **4**, 1900623 (2019).
58. K. Dai, J. K. Miller, and E. G. Johnson, "Real-time OAM cross-correlator based on a single-pixel detector HOBBIT system," Opt. Express **28**(26), 39277-39287 (2020).

59. S. Franke-Arnold, S. M. Barnett, E. Yao, J. Leach, J. Courtial, and M. Padgett, "Uncertainty principle for angular position and angular momentum," New J. Phys. **6**, 103 (2004).

60. J. C. Gutiérrez-Vega and M. A. Bandres, "Helmholtz–Gauss waves," J. Opt. Soc. Am. A **22**(2), 289–298 (2005).

61. K. Morgan, Y. Li,W. Li, J. K. Miller, R. J.Watkins, and E. G. Johnson, "Multilevel quadrature amplitude multiplexing using coherently coupled orbital angular momentum modes," Opt. Express **26**(9), 12180–12190 (2018).

62. B. Jack, A. M. Yao, J. Leach, J. Romero, S. Franke-Arnold, D. G. Ireland, S. M. Barnett, and M. J. Padgett, "Entanglement of arbitrary superpositions of modes within two-dimensional orbital angular momentum state spaces," Phys. Rev. A **81**(4), 043844 (2010).

63. M. Kutila, P. Pyykönen, H. Holzhüter, M. Colomb, and P. Duthon, "Automotive LiDAR performance verification in fog and rain," in 2018 21st International Conference on Intelligent Transportation Systems (ITSC), 1695–1701 (2018).

64. L. Rego, K. M. Dorney, N. J. Brooks, Q. L. Nguyen, C. Liao, J. San Román, D. E. Couch, A. Liu, E. Pisanty, M. Lewenstein, L. Plaja, H. C. Kapteyn, M. M. Murnane, and C. Hernández-García, "Generation of extreme-ultraviolet beams with time-varying orbital angular momentum," Science **364**(6447), eaaw9486 (2019).

65. A. Chong, C. Wan, J. Chen, and Q. Zhan, "Generation of spatiotemporal optical vortices with controllable transverse orbital angular momentum," Nat. Photonics **14**(6), 350-354 (2020).

66. S. W. Hancock, S. Zahedpour, A. Goffin, and H. M. Milchberg, "Free-space propagation of spatiotemporal optical vortices," Optica **6**(12), 1547-1553 (2019).

67. G. Gui, N. J. Brooks, H. C. Kapteyn, M. M. Murnane, and C. Liao, "Second-harmonic generation and the conservation of spatiotemporal orbital angular momentum of light," Nat. Photonics **15**, 608-613 (2021).

68. Z. Zhao, H. Song, R. Zhang, K. Pang, C. Liu, H. Song, A. Almaiman, K. Manukyan, H. Zhou, B. Lynn, R. W. Boyd, M. Tur, and A. E. Willner, "Dynamic

spatiotemporal beams that combine two independent and controllable orbital-angular-momenta using multiple optical-frequency-comb lines," Nat. Commun. **11**, 4099 (2020).

69. F. Bouchard, N. H. Valencia, F. Brandt, R. Fickler, M. Huber, and M. Malik, "Measuring azimuthal and radial modes of photons," Opt. Express **26**(24), 31925-31941 (2018).
70. Y. Zhou, M. Mirhosseini, D. Fu, J. Zhao, S. Rafsanjani, H. Mohammad, A. E. Willner, and R. W. Boyd, "Sorting photons by radial quantum number," Phys. Rev. Lett. **119**, 263602 (2017).
71. K. Dai, J. K. Miller, J. Free, M. Lemon, F. Dalgleish, and E. G. Johnson, "Remote sensing using a spatially and temporally controlled asymmetric perfect vortex basis generated with a 2D HOBBIT," Opt. Express **30**(19), 34765-34775 (2022).
72. G. Gbur, "Partially coherent beam propagation in atmospheric turbulence [Invited]," J. Opt. Soc. Am. A **31**(9), 2038-2045 (2014).
73. A. Dhalla, J. V. Migacz, and J. A. Izatt, "Crosstalk rejection in parallel optical coherence tomography using spatially incoherent illumination with partially coherent sources," Opt. Lett. **35**(13), 2305-2307 (2010).
74. B. Redding, M. A. Choma, H. Cao, "Speckle-free laser imaging using random laser illumination," Nat. Photonics **6**, 355–359 (2012).
75. Y. Chen, S. A. Ponomarenko, and Y. Cai, "Self-steering partially coherent beams," Sci. Rep. **7**, 39957 (2017).
76. J. K. Wood, K. A. Sharma, S. Cho, T. G. Brown, and M. A. Alonso, "Using shadows to measure spatial coherence," Opt. Lett. **39**(16), 4927-4930 (2014).
77. M. Koivurova, H. Partanen, J. Turunen, and A. T. Friberg, "Grating interferometer for light-efficient spatial coherence measurement of arbitrary sources," Appl. Opt. **56**(18), 5216-5227 (2017).
78. A. Bhattacharjee, S. Aarav, and A. K. Jha, "Two-shot measurement of spatial coherence," Appl. Phys. Lett. **113**, 051102 (2018).

79. R. Martínez-Herrero, M. Santarsiero, G. Piquero, and J. González de Sande, "A New Type of Shape-Invariant Beams with Structured Coherence: Laguerre-Christoffel-Darboux Beams," Photonics **8**(4), 134 (2021).
80. F. A. Bovino, M. Braccini, M. Giardina, and C. Sibilia, "Orbital angular momentum in noncollinear second-harmonic generation by off-axis vortex beams," J. Opt. Soc. Am. B **28**(11), 2806–2811 (2011).
81. S.-M. Li, L.-J. Kong, Z.-C. Ren, Y. Li, C. Tu, and H.-T. Wang, "Managing orbital angular momentum in second-harmonic generation," Phys. Rev. A **88**(3), 035801 (2013).
82. K. Dai, W. Li, K. S. Morgan, Y. Li, J. K. Miller, R. J. Watkins, and E. G. Johnson, "Second-harmonic generation of asymmetric Bessel-Gaussian beams carrying orbital angular momentum," Opt. Express **28**(2), 2536-2546 (2020).
83. R. N. Lanning, Z. Xiao, M. Zhang, I. Novikova, E. E. Mikhailov, and J. P. Dowling, "Gaussian-beam-propagation theory for nonlinear optics involving an analytical treatment of orbital-angular-momentum transfer," Phys. Rev. A **96**(1), 013830 (2017).
84. K. Dai, W. Li, K. S. Morgan, J. K. Miller, R. J. Watkins, and E. G. Johnson, "Second-harmonic Generation of Asymmetric Bessel-Gaussian Beams Carrying Multiple OAM Charge Numbers," in Conference on Lasers and Electro-Optics, OSA Technical Digest (Optica Publishing Group, 2020), paper JTh2E.9.
85. L. Allen and M. Padgett, The Orbital Angular Momentum of Light: An Introduction (Wiley-VCH Verlag GmbH & Co. KGaA, 2011).
86. K. Dai, J. K. Miller, W. Li, R. J. Watkins, and E. G. Johnson, "Fractional orbital angular momentum conversion in second-harmonic generation with an asymmetric perfect vortex beam," Opt. Lett. **46**(14), 3332-3335 (2021).
87. R. W. Boyd, Nonlinear Optics (Academic Press, New York, 2008).
88. M. Erhard, M. Krenn, and A. Zeilinger, "Advances in high-dimensional quantum entanglement," Nat. Rev. Phys. **2**, 365 (2020).

89. C. Bennett, H. Bernstein, S. Popescu, and B. Schumacher, “Concentrating partial entanglement by local operations,” Phys. Rev. A **53**(4), 2046-2052 (1996).
90. C. H. Bennett, G. Brassard, C. Crépeau, R. Jozsa, A. Peres, and W. K. Wootters, “Teleporting an unknown quantum state via dual classical and Einstein-Podolsky-Rosen channels,” Phys. Rev. Lett. **70**(13), 1895-1899 (1993).
91. S. Karan, Radhika Prasad, and Anand K. Jha. “Postselection-free controlled generation of high-dimensional OAM entangled state,” arXiv preprint arXiv:2203.14799 (2022).
92. J. P. Torres, A. Alexandrescu, and L. Torner, “Quantum spiral bandwidth of entangled two-photon states,” Phys. Rev. A **68**, 050301 (2003).
93. E. V. Kovlakov, S. S. Straupe, and S. P. Kulik, “Quantum state engineering with twisted photons via adaptive shaping of the pump beam,” Phys. Rev. A **98**, 060301 (2018).
94. A. Yao, “Spectral decomposition of entangled photons with an arbitrary pump,” New J. Phys. **13**, 053048 (2011).
95. K. Dai, J. Free, J. K. Miller, R. J. Watkins and E. G. Johnson, "Ultraviolet Orbital Angular Momentum Generation Through a Second-Harmonic Process," 2022 Conference on Lasers and Electro-Optics (CLEO), 2022, pp. 1-2.